5-2016

Kinematic behavior of sheared sand with emphasis on particle to particle interaction using computed tomography

Maha Fawaz Jarrar
University of Tennessee - Knoxville, mjarrar@vols.utk.edu

To the Graduate Council:

I am submitting herewith a thesis written by Maha Fawaz Jarrar entitled "Kinematic behavior of sheared sand with emphasis on particle to particle interaction using computed tomography." I have examined the final electronic copy of this thesis for form and content and recommend that it be accepted in partial fulfillment of the requirements for the degree of Master of Science, with a major in Civil Engineering.

Khalid A. Alshibli, Major Professor

We have read this thesis and recommend its acceptance:

Angelica M. Palomino, Dayakar Penumadu

Accepted for the Council:
Dixie L. Thompson

Vice Provost and Dean of the Graduate School

(Original signatures are on file with official student records.)

Kinematic behavior of sheared sand with emphasis on particle to particle interaction using computed tomography

A Thesis Presented for the
Master of Science
Degree
The University of Tennessee, Knoxville

Maha Fawaz Jarrar
May 2016

This Thesis is dedicated
To my family and friends
And
To Amer

ACKNOWLEDGEMENTS

I would first like to thank my thesis advisor Dr. Khalid Alshibli of the Department of Civil and Environmental Engineering at the University of Tennessee, Knoxville. The door to Prof. Alshibli was always open whenever I ran into a trouble spot or had a question about my research or writing. I would also like to thank my research team at UTK especially Andrew Druckrey. Without his training and input, the work on this Thesis will be incomplete.

This material is partially funded by the US National Science Foundation (NSF) under Grant No. CMMI-1266230 and Office of Naval Research (ONR) grant No. N00014-11-1-0691. Any opinions, findings, and conclusions or recommendations expressed in this material are those of the authors and do not necessarily reflect the views of the NSF or ONR. The SMT images presented in this paper were collected using the X-Ray Operations and Research Beamline Station 13-BMD at Argonne Photon Source (APS), a U.S. Department of Energy (DOE) Office of Science User Facility operated for the DOE Office of Science by Argonne National Laboratory under Contract No. DE-AC02-06CH11357. We acknowledge the support of GeoSoilEnviroCARS (Sector 13), which is supported by the National Science Foundation - Earth Sciences (EAR-1128799), and the Department of Energy, Geosciences (DE-FG02-94ER14466). We thank Dr. Mark Rivers of APS for help in performing the SMT scans.

ABSTRACT

Granular materials are a three-phase mixture of solid, liquid, and gas that exhibit complex engineering properties. They have a heterogeneous composition in nature and consist of many discrete particles with complex interactions. Granular materials are commonly used in many civil engineering construction projects, therefore, a better understanding of behavior of granular materials may result in safe and economical design. This thesis is a compilation of two related topics. A 3D systematic experimental study that investigates the influence of particle morphology, confining pressure, and specimen density on the failure mode of sheared sand is presented. Three uniform sand specimens with different morphologies as well as spherical glass beads were tested under axisymmetric triaxial loading. The deformation of the tested specimens was monitored using in-situ 3D Synchrotron Microtomography (SMT), and maps of incremental particle translation and rotation were developed. The results of the analysis shows that the angularity of particles is the major player in the failure mode of the sheared sand under high confining pressure, where specimens fails either via a single well-defined shear band or via a bulging mode. Dense specimens tested under low confining pressure, as well as loose specimen exhibited a preference to fail via bulging in the middle of the specimens. The second part of the Thesis presents an experimental validation of the finite strain formulations that were developed by Zhang and Regueiro (2015) using 3D images of sheared F35 Ottawa sand specimens. The spatial maps of Eulerian octahedral shear strain were used to identify intensive shearing zones within the specimens, and compared well with maps of incremental particle translation and rotation for the same specimens. The local Eulerian volumetric strain was compared to the global measurements, which also can be considered

as an averaging of all local Eulerian volumetric strains. Void ratio evolution curves generally compared well with the volumetric strains at both the local and global level.

TABLE OF CONTENTS

LIST OF TABLES

LIST OF FIGURES

INTRODUCTION

The constitutive behavior of sheared sand is highly influenced by particle morphology, gradation, mineralogy, specimen density, loading condition, stress path, and boundary conditions. The failure of a soil mass in the field is commonly manifested in the development of a shear intensive failure surface known as a shear band. Researchers performed lab experiments on soil specimen such as the conventional triaxial compression (CTC) and plane strain loading to determine deformation properties of soils (e.g., Lee 1970; Marachi et al. 1981). The failure modes of the plane strain soil specimen are well documented in the literature (e.g., Alshibli and Sture 2000; Finno et al. 1997; Han and Drescher 1993). Whereas, the reported failure modes of CTC experiments were based on observations of the surface deformation. Such observations may be misleading in describing the failure modes of CTC experiments as many specimens have more complex internal failure mode than what the surface shows.

In the last two decades, few researchers have utilized Computed Tomography (CT) to investigate the failure mode of sand specimens loaded under triaxial compression (e.g., Desrues et al. (1996) and Alshibli et al. (2003)). Hall et al. (2010) developed a discrete approach called V-DIC to determine particle rotations and were able to emphasize their influence on strain localization within CT scans of triaxial sand specimens. However, this approach proved to be computationally expensive. To reduce the computational power needed to analyze individual particle kinematics, Ando et al. (2012) developed an alternative tracking technique (ID-Track) which uses single particle property (i.e., particle volume) to identify particles and track them as well as calculate individual particle rotations

and translations. Recently, Desrues and Ando (2015) used ID-Track to compare the translation and rotation fields within the fully developed shear band in angular Hostun and the rounded Caicos ooid sands, as well as Ottawa 50/70 sand. They found that angular Hostun sand exhibited a higher resistance to rotations due to particle interlocking, which caused the shear band to constitute a layer of outer particles with close to zero rotations that surround particles with higher rotations within the middle of the shear band. This was not observed in the rounded Caicos ooid particles where the shear band was narrower with concentrated high rotations. The Ottawa 50/70 sand specimen represents middle particle morphology between the two extremes, which supported the conclusion that there is an inverse relationship between the intensity of the rotations and grain angularity.

Although the Grenoble research group (Ando et al. 2012; Desrues and Ando 2015) has made an excellent contribution to the literature in this field and provided interesting insights about the effects of sand grain morphology on particle kinematic behavior within a shear band, there are still unanswered questions about a quantitative link between particle morphology and strain localization. It is also important to note that the top end platen of Ando et al. (2012) specimens rotated slightly as the loading progressed, which may caused specimen failure via a shear band and consequently a different material response than that of a conventional triaxial test. In addition, there is no published literature on using 3D imaging techniques to investigate the failure mode of sand triaxial specimens as a function of confining stress and initial density. In the first part of this Thesis, in-situ SMT scans were acquired for three different sands with morphology varying from very angular to rounded particles as well as a specimen composed of spherical glass beads. Particle

rotations and translations are calculated, and the failure modes of the specimens tested under both high and low confining pressures are discussed in relation to their morphologies and their initial densities.

Many researchers utilized a broad number of experimental and theoretical studies that focus on deriving the constitutive equations to define the relationship between stresses and strains in granular materials. The measurement of the stress tensor, known as the Cauchy stress tensor, has been well established in the literature (e.g., Cundall and Strack 1979; Christoffersen et al. 1981; Rothenburg and Selvadurai, 1981; Bagi 1996; Bardet and Vardoulakis 2001). On the other hand, there is no conclusive work on the formulation and interpretation of the strain tensor, especially at the large deformation level and in 3D. Recently, Zhang and Regueiro (2015) proposed an equivalent continuum method to measure finite strains in 3D at the local level in granular material subjected to large deformations.

The second part of this Thesis, is an experimental validation of the codes developed by Zhang and Regueiro (2015) to calculate the local finite strains within granular specimens. A sub-sample was taken from the specimens that were analyzed in the first part, and further analysis was conducted in preparation to calculate the local finite strains. Since the codes used in this study apply the equivalent continuum approach, a continuous domain (i.e. Representative elementary volume (REV)) that replaces the granular assembly is required. REV size identification was conducted using two methods. The first method utilized Avizo 8.0 software while the other used the code of Zhang and Regueiro (2015) to calculate Eulerian volumetric strain ($\bar{E}_v$) and octahedral shear strain ($\bar{\gamma}_{oct}$) for cubical sub-

volumes. Finally, the strains were calculated for the specimens at multiple compression stages and were compared to global measurements, the evolution of the void ratio, and particle kinematics.

CHAPTER I
INFLUENCE OF PARTICLE MORPHOLOGY ON 3D KINEMATIC BEHAVIOR AND STRAIN LOCALIZATION OF SHEARED SAND

A version of this chapter is currently under review for publishing by Khalid A. Alshibli, Maha F. Jarrar, Andrew M. Druckrey, and Riyadh I. Al-Raoush:

Khalid A. Alshibli, Maha F. Jarrar, Andrew M. Druckrey, Riyadh I. Al-Raoush. (2016) "Influence of Particle Morphology on 3D Kinematic Behavior and Strain Localization of Sheared Sand." *J. Geotech. Geoenviron. Eng*. under review

This paper has been submitted to the ASCE journal of Geotechnical and Geonenvironmental Engineering and is currently under review. In this work, I have completed the image processing of all the specimen in the study. I also completed the image analysis by applying C++ codes that were developed by Riyadh I. Al-Raoush. I also generated the figures related to particle tracking, and maps of particle displacements and rotations, by applying and updating (for the purpose of this work) Matlab codes which were written by Andrew M. Druckrey. Khalid A. Alshibli and Maha F. Jarrar co-wrote the paper, Khalid A. Alshibli finalized and submitted the paper. The experimental work and SMT imaging was done by the combined effort of Andrew M. Druckrey, Khalid A. Alshibli, and myself.

Abstract

The constitutive behavior of sheared sand is highly influenced by particle morphology, gradation, mineralogy, specimen density, loading condition, stress path, and boundary conditions. The literature lacks a 3D systematic experimental study that investigates the influence of particle morphology, confining pressure, and specimen density on the failure mode of sheared sand. In this paper, surface texture, roundness, and sphericity of three uniform sands and glass beads with similar grain size were quantified using 3D images of particles. In situ non-destructive 3D Synchrotron Micro-Computed Tomography (SMT) was used to monitor the deformation of loose and dense dry sand specimens that were tested under axisymmetric triaxial loading condition at 15 kPa and 400 kPa confining pressures. Particles were identified and tracked in 3D as shearing progressed within the specimens, and maps of incremental particle translation and rotation were developed and used to uncover the relationship between particle morphology, specimen density, and

confining pressure on the deformation and failure mode of sheared sand. The paper discusses the relationship between the failure mode and particle morphology, specimen density, and confining pressure.

Introduction

The constitutive behavior of soils is highly influenced by the arrangement of particles, particle groups, and associated pore space. These geometric properties comprise the so-called *material structure or fabric* (Mitchell, 1993). The failure of a soil mass in the field is commonly manifested in the development of a shear intensive failure surface known as a shear band. The geometry of the shear band is affected by soil properties, boundary conditions, and loading mode (i.e., plane strain, triaxial, simple shear, etc.). Researchers usually test laboratory soil specimens using conventional triaxial compression (CTC) or plane strain loading conditions to determine strength and deformation properties of soils (e.g., Lee 1970; Marachi et al. 1981). It is well-documented in the literature that plane strain specimens fail via a single or multiple shear bands depending on boundary conditions (e.g., Alshibli and Sture 2000; Finno et al. 1997; Han and Drescher 1993) whereas CTC specimens fail via bulging or diffuse bifurcation based on observations of the specimen surface deformation (e.g., Desrues and Hammad 1989; Desrues et al. 1985; Peric et al. 1992; Peters et al. 1988). However, judging the failure mode of specimens from observing their surface deformation may result in a misleading description of their failure mode as many specimens have more complex internal failure modes than what the surface shows.

In the last two decades, few researchers have utilized Computed Tomography (CT) to investigate the failure mode of sand specimens loaded under triaxial compression.

Desrues et al. (1996) and Alshibli et al. (2003) used in situ CT to monitor the failure mode and calculate the change of void ratio in sand specimens and found that bulging is just an external manifestation of a rather complex internal failure patterns. Batiste et al. (2004) used CT to track the onset, propagation, and measure the thickness and orientation of shear bands of specimens composed of F-75 Ottawa sand that were tested at relatively low confining pressures (0.05 to 1.3 kPa). The scans were collected at the end of experiments on similar specimens, which did not offer the opportunity to track particle kinematic behavior within the same specimen. Matsushima et al. (2006, 2007) used in situ Synchrotron Micro Computed tomography (SMT) to identify and track individual particles in 2D axial sections of a sand specimen. However, 2D analysis has a limitation as it ignores out of plane particle kinematic behavior.

To study the deformation and failure mechanisms at the 3D level, continuum approaches such as digital image correlation (DIC) and digital volume correlation (DVC) have been used to determine strain fields of laboratory sand specimens assuming continuum framework for the analysis (e.g., Rechenmacher 2006; Sjödahl et al. 2012). Although these techniques have high levels of accuracy, they ignore the granular nature of sand and the discrete kinematics at the particle scale. Hall et al. (2010) developed a discrete approach called V-DIC which uses volumetric subsets that represent the actual shape and position of each individual particle to determine particle rotations within triaxial sand specimens. Viggiani et al. (2013) combined both the continuum and the discrete V-DIC methods to analyze two dry sand specimens of angular Hostun and round Caicos ooid sands sheared under triaxial compression. Based on the continuum method, they found that strain

localization initiates during the hardening regime before the peak stress stage, and the shear band begins to diffuse as the load progresses beyond the peak state. The discrete V-DIC approach also provided experimental evidence that strain localization initiates during the hardening regime before the peak and emphasized the influence of particle rotations on strain localization.

The discrete V-DIC method depends on the grayscale image to recognize individual particles, which proved to be computationally expensive. To reduce the computational power needed to analyze individual particle kinematics, Ando et al. (2012) developed an alternative tracking technique (ID-Track) and applied it on the same sand specimens reported by Viggiani et al. (2013). ID track used a single particle property (i.e., particle volume) to identify particles and track them. The particle voxel volume was used in the tracking procedure, and the translation of the particles was calculated by finding the difference in the position of the center of mass between two consecutive binarized images. Rotations, on the other hand, lacked precision, and were calculated using two orientation vectors that defined the minimum and maximum eigenvectors of the moment of inertia tensor. The reason for the lower accuracy of the rotation calculations reported by Ando et al. (2012) resides in the image processing technique where the addition of extra voxels to one side of a particle will shift the orientation of the eigenvector resulting in errors in rotation values. In this paper, we improved this analysis technique by incorporating multiple particle properties such as volume, surface area, and dimension in the particle tracking approach and by introducing a new method to quantify particle rotations.

Recently, Desrues and Ando (2015) compared the translation and rotation fields within the fully developed shear band in angular Hostun and the rounded Caicos ooid sands, as well as Ottawa 50/70 sand. They found that angular Hostun sand exhibited a higher resistance to rotations due to particle interlocking, which caused the shear band to constitute a layer of outer particles with close to zero rotations that surround particles with higher rotations within the middle of the shear band. This was not observed in the rounded Caicos ooid particles where the shear band was narrower with concentrated high rotations. The Ottawa 50/70 sand specimen represents middle particle morphology between the two extremes, which supported the conclusion that there is an inverse relationship between the intensity of the rotations and grain angularity.

Although the Grenoble research group (Ando et al. 2012; Desrues and Ando 2015) has made an excellent contribution to the literature in this field and provided interesting insights about the effects of sand grain morphology on particle kinematic behavior within a shear band, there are still unanswered questions about a quantitative link between particle morphology and strain localization. It is also important to note that the top end platen of Ando et al. (2012) specimens rotated slightly as the loading progressed, which may caused specimen failure via a shear band, and consequently, a different material response than that of a conventional triaxial test. In addition, there is no published literature on using 3D imaging techniques to investigate the failure mode of sand triaxial specimens as a function of confining stress and initial density. In this paper, in-situ SMT scans were acquired for three different sands with morphology varying from very angular to rounded particles as well as a specimen composed of spherical glass beads. Particle rotations and translations

are calculated, and the failure modes of the specimens tested under both high and low confining pressures are discussed in relation to their morphologies and their initial densities.

Experiments

Three silica sands known as F-35 Ottawa sand (labeled F35), #1 dry glass sand (labeled DG), and GS#40 Columbia grout sands (labeled GS40) were acquired (Figure 1), and only size fraction between US sieves #40 (0.429 mm) and #50 (0.297 mm) were used in this study (Table 1)"All tables and figures are located in the appendix". They represent silica sands with different morphology ranging from rounded to angular particle classes. Glass beads (labeled as GB) with grain sizes similar to the study sands were also included in the investigation to provide baseline measurements for roundness, sphericity, and smooth surface texture. Surface texture is used to describe the surface of particles (e.g., polished, greasy, frosted, etc.) that are too small to affect the overall shape. Roundness refers to those aspects of particle surface (sharpness of corners and edges) that are on a larger scale than those classed as surface texture, but that are smaller than the overall dimensions of the particle. Sphericity is used to describe the overall form of the particle irrespective of the sharpness of edges and corners. It is a measure of the degree of conformity of particle shape to that of a sphere. Alshibli et al. (2015) proposed a root mean square texture (Rq) as an index to measure surface texture of sand particles using optical interferometry technique. Roundness (I_R) and sphericity (I_{sph}) indices were calculated from 3D images of particles.

Table 2 lists morphology indices of the sands and glass beads. The ranking listed in Table 2 considered full statistical distribution of parameters (not shown in this paper) that include mean, SD, and other statistical parameters.

A miniature triaxial test cell [similar to the one used in Hasan and Alshibli (2012)], lightweight and small to facilitate its being mounted on a rotating stage, was used to acquire in-situ 3D SMT images. Specimens were cylindrical in shape with an aspect ratio of ~2. A computer-controlled stepper motor was used to load the specimen at a constant displacement rate of 0.2 mm/minute. Axial load was recorded using a load cell located inside the test cell. To prepare a specimen, a latex membrane was first secured to the bottom end platen using a rubber o-ring, then an aluminum mold was placed and tightened around the membrane. To align the membrane inside the mold wall, vacuum was applied to the mold-membrane interface. After the mold was filled with sand, the membrane was stretched over the top end platen and secured using another o-ring. The vacuum line was switched to the specimen pore space, the mold was removed, and the other components of the triaxial cell were assembled. The test cell was then bolted to the stage of the SMT scanner and the vacuum was gradually reduced while the air pressure was increased to apply the confining pressure (σ_3) until reaching the desired σ_3 value (σ_3 = 15 kPa or σ_3 = 400 kPa).

The experiments were performed on dry specimens under drained condition. Two dense specimens of each of the sands and glass beads were prepared at a relative density (Dr) of ~85%–100%, one specimen of F35 sand was prepared in a loose state with a relative density of 49%, and another specimen of DG sand was prepared at a relative density of

64%, which can be considered as loose (Table 3). The loose specimens were prepared using a funnel with a long stem and the sand was slowly poured through the funnel at a small drop height while the funnel was slowly raised as the mold filled. Preparing loose specimens proved to be very difficult due to the narrow grain-size range, small size of the specimen, and the placement of the top platen that can cause the specimen to densify. To prepare the dense specimens, the sand was filled in five layers with each layer gently tamped with a rod before the next successive layer was filled. One specimen of each of the dense and loose states was tested at σ_3 = 15 kPa, which is considered a very low confining pressure; the rest of the dense specimens were tested under a relatively high confining pressure (σ_3 = 400 kPa).

SMT Scans

Since the 1990s, x-ray computed tomography (CT) has emerged as a powerful non-destructive 3D scanning technique to study geomaterials. In principle, CT consists of measuring the attenuation of an x-ray beam for a number of different paths through the tested object and mathematically extracting the density of each point in a plane of the object. This 2D density map constitutes a CT slice, which gives very accurate information within the plane. By creating several slices, a true 3D volumetric image of the object can be built up. It is a powerful nondestructive scanning technique for visualizing the internal structure of objects. CT has been extensively used to characterize engineering properties of soils and rocks (e.g., Otani and Obara 2004; Desrues et al. 2006; and Alshibli and Reed 2010). For example, CT was used to study spatial distribution of void ratio in granular materials (Alshibli et al. 2000a) and to investigate the deformation patterns of sand

specimens (Desrues et al. 1996; Alshibli et al. 2000b). Alshibli and Alramahi (2006) captured a 3D interaction of 6 mm beads during triaxial compression using an industrial CT system.

The resolution of most industrial CT detectors is in the range of 20 to 40 microns, which makes it difficult to capture particle-to-particle interaction of sand specimens with an average grain size of 160 microns for a typical triaxial specimen. A significant enhancement to the conventional x-ray tomography systems is the use of synchrotron radiation. Synchrotron radiation sources generate higher intensity beams (10^6 times greater) than conventional x-ray beams). It has several advantages over industrial x-ray sources, including high intensity of photon flux (number of photons per second), high degree of collimation (source divergence leads to image blur), and the ability to tune the photon energy over a wide range using an appropriate monochromator for obtaining specific-element measurements (Kinney and Nichols 1992). Synchrotron micro-computed tomography (SMT) produces images with higher resolution than that produced by industrial CT systems.

The SMT scans reported in this paper were acquired at beamline 13D of the Advanced Photon Source (APS), Argonne National Laboratory (ANL), Illinois, USA. The specimens were scanned using a monochromatic energy of 33 keV, and the image spatial resolution for the specimen scans varied from 8.16 micron/voxel to 11.14 micron/voxel depending on the camera used at the time of scanning (Table 3). An initial scan was acquired before a specimen was loaded and then compressed to a prescribed compression displacement (e.g., 0.2 mm); here compression was paused to acquire the scan.

Compression proceeded to the next value (e.g., 0.4 mm) where another scan was acquired, and so on, until 8 to 10 scans per specimen were acquired (Table 3)

Stress-Strain behavior

Figure 2 through Figure 4 show the nominal axial strain (ε_1) versus the principle stress ratio (PSR= σ_1/σ_3) and ε_1 versus volumetric strain (ε_v) for the dense specimens tested at σ_3 = 400 kPa, dense specimens tested at σ_3 = 15 kPa, and loose specimens tested at σ_3 = 15 kPa, respectively. ε_v was calculated from SMT images. Under relatively high confining pressure (σ_3 = 400 kPa), all specimens exhibited a gradual increase in PSR to a peak state followed by a small degree of softening. The DG sand (DG-D-400kPa) exhibited the highest peak PSR value of 4.1 at $\varepsilon_1 = 7.1\%$, followed by a small degree of softening (Figure 2). It has dilative behavior up to $\varepsilon_1 = 12.2\%$ followed by minimal change in ε_v. The F35-D-400kPa sand specimen reached a peak PSR of 4.0 at $\varepsilon_1 = 5.6\%$, followed by a relatively higher degree of softening. The GS40-D-400kPa specimen closely followed F35-D-400kPa where it reached the peak PSR of 3.8 at $\varepsilon_1 = 6.0\%$ followed by a small degree of softening. The glass beads specimen reached a peak PSR of 2.8 at $\varepsilon_1 = 3.7\%$ followed by a very small degree of softening. The F35, GS40, and GB specimens show a similar initial dilative behavior followed by a critical state behavior at different strain levels. As particle morphology changes from smooth round to rough angular beads/sand, the PSR increases, and it takes more axial strain to reach the peak PSR due to relatively high interlocking between angular rough particles than rounded smooth particles.

Dense specimens tested under low confining pressure (σ_3 = 15 kPa) did not exhibit a peak stress state but rather an initial increase in PSR followed by a smaller rate of increase

as compression progressed (Figure 2); a typical behavior of a dense specimen tested at low confining pressure. All specimens show a dilative behavior throughout the test at similar rates. The influence of σ_3 is evident from Figure 2 & Figure 3 where a higher PSR and higher volumetric strain are recorded for dense specimens when they are tested under low confining pressure than when they are subjected to a high confining pressure. Figure 4 displays the behavior of the loose DG and F35 specimens under low confining pressure (σ_3 = 15 kPa), which is marked by a gradual increase in PSR and ε_v as compression progresses without reaching the critical state due to uniform grain size of particles and relatively low confining pressure. It will take a very high strain for the specimen to reach a critical state.

Image Processing, Particle Identification, and Tracking

Processing of the SMT images was performed using Avizo Fire 8.0 software, which uses the Visilog algorithm for image processing and quantification. For each loading stage, four overlapping scan heights at a constant step size were acquired to image the whole volume of the specimen at a high resolution. The raw grayscale SMT scans were loaded into the software according to their step size and were stitched together using the merging module, forming a scan volume of the entire specimen (Figure 5a). Noise from the grayscale images was removed using an anisotropic diffusion filter, which generates a diffusion coefficient in the form of an edge seeking function that preserves the edges between the particles and the voids while removing the noise elsewhere (Figure 5b).

The images were then segmented using a consistent threshold value to separate the solid particles from the surrounding air, resulting in a binarized image with values of one

for the solid particles and values of zero for the surrounding air. The high resolution of the SMT images allowed for a constant global threshold value to be used for all scans throughout the loading stages, which resulted in accurate binary images and minimized errors in particle morphology calculations, thus increasing accuracy in tracking particles and in quantification of particle kinematics. After applying the threshold value, some particle voxels may be mistakenly assigned a value of zero resulting in a hole of void within the segmented particle, while void voxels would be mistakenly given a value of one forming an island. Avizo Fire 8.0 provides a "fill holes" algorithm that finds the mislabeled voxels within particles and assigns them a value of one while another "opening" algorithm is used to remove the islands within the air voids of the image. Furthermore, particles in the resultant binarized image remain in contact with neighboring particles; therefore, it is impossible to identify them individually (Figure 5c). Visilog has a watershed algorithm that separates particles from each other by removing the small area of contact between them. It also removes voxels that represent the contact points between particles and the loading platens. Another algorithm called "border kill" was applied to delete the voxels touching the borders of the image and the voxels that represent the loading platens (Figure 5d). Each particle was then individually labeled so that each could be identified and discretely quantified (Figure 5e). The particle labels were then expanded and masked with the binary image to regain the contact points that had been removed during separation, thus providing a labeled image with particles in contact.

Further analysis to find different physical properties of the labeled particles in the 3D images was conducted using a modified version of the code that was originally developed

by Al-Raoush (2007) and modified by the authors (see Druckrey et al. 2015). The particle centroid coordinates were calculated based on the particle's center of mass. Each particle's volume was calculated by summing the voxel volumes that constitute the particle. Likewise, particle surface area was calculated by summing the areas of the exterior faces of boundary voxels belonging to the particle. The concept of principal component analysis (PCA) was used on the particle voxels to find the three orthogonal directions that represent the shortest (d_S), intermediate (d_I), and longest (d_L) lengths of the particle that passes through the center of the mass. The three lengths were computed statistically by using singular value decomposition and the distances between the extreme points along those directions represent the three particle lengths. Druckrey et al. (2015) provides detailed explanation of the code features.

Although Avizo labels particles, it does not necessarily give the same label to a specific particle throughout different scans. Therefore, the Druckrey and Alshibli (2014) algorithm was used to track particles between two consecutive scans. The particle tracking process begins with isolating a sub-volume around each particle's centroid in the first image and uses the sub-volume in the second image to look for a matching particle. Individual particle properties (particle volume, surface area, and the three orthogonal lengths) within a 3–4% margin of error were used in the tracking procedure. If the algorithm did not find a matching particle, it was eliminated from the analysis. If more than one matching particles are found, the particle with the closest morphological properties is selected.

Particle Kinematic Behavior

Particle kinematic behavior is described using translation gradients and degree of particle rotation in 3D. Particle translation gradients were calculated as the difference in the particle centroid in the x, y, and z directions between two consecutive scans. Rotations were also calculated by measuring the change in angle of rotation of the longest particle length with respect to the direction of the major principal stress (z-axis or loading direction). Previous work of Alshibli and Alramahi (2006) and Hasan and Alshibli (2012) have demonstrated that it is enough to use the angle with respect to the loading direction (major principal stress) as a measure of particle rotation since the angle with respect to the direction of minor principal stress exhibits a normal statistical distribution due to axisymmetric behavior of triaxial specimens in that plane.

Dense specimens tested under high confining pressure ($\sigma_3 = 400$ kPa)

Figure 6 through Figure 15 show the translations and rotations for experiments on dense specimens sheared under σ_3 = 400 kPa. Both the F35-D-400kPa and the GS40-D-400kPa specimens exhibited failure through a well-defined single shear band. Referring to Figure 6, the translation maps of F35-D-400kPa show evidence of an onset of a localized shear zone prior to the peak PSR state at $\varepsilon_1 = 4.9\%$ (Figure 6d), which is also evident from Figure 7 where particle rotations initiate as early as $\varepsilon_1 = 3.4\%$ (Figure 7c). Both translations and rotations become more localized as the PSR reached the peak state (Figure 6e and Figure 7e), and a fully developed single shear band can be seen at the last translation increment at $\varepsilon_1 = 11.7\%$. The development of a single shear band caused a relatively higher post-peak PSR softening for F35-D-400kPa when compared to other sands (Figure

2). Figure 8 displays the translation gradients of GS40-D-400kPa specimen, which provides an evidence of shear band onset at $\varepsilon_1 = 3.3\%$ (Figure 8c) collaborated with few and dispersed particle rotations (Figure 9c). Localization of rotations became clearer at the peak PSR ($\varepsilon_1 = 6.66\%$) that later developed into a well-defined single shear band at the post-peak regime.

The shear bands that developed in the GS40-D-400kPa and F35-D-400kPa specimens are associated with higher resistances to particle rotations due to a high confining pressure and interlocking that forces the shear band to include a larger number of particles with low rotations surrounding particles with higher rotations at the center of shear band (Figure 9h). A careful look at particle morphology in Table 2 shows that F35 sand has the highest roughness, highest non-sphericity, and second lowest roundness excluding the GB. The GS40 sand is more spherical, more angular, and has less roughness than F35 sand. The measured shear band thickness of F35-D-400kPa is 3.36 mm ($9.5d_{50}$, where d_{50} is mean particle size) compared to 4.06 mm ($11.32d_{50}$) for the GS40-D-400kPa specimen. It appears that particle roundness is the main contributor to particle interlocking and specimen tendency to develop a shear band. The translation maps also show a transition zone from highly displaced particles to the low particle translation zone of a narrow inclined line that follows the shear band direction in F35-D-400kPa in Figure 6g, whereas the transition zone is wider in the GS40-D-400kPa specimen (Figure 8h). The thicknesses of the transition zone in particle translation of F35-D-400kPa and GS40-D-400kPa were lower than that of the rotations and were equal to 1.09 mm ($3d_{50}$) and 1.48 mm ($4.1d_{50}$), respectively. It can

also be noted that the thickness of the transition zone increases at the bottom part of the shear band as the sand tries to shear in that direction for both specimens.

Figure 10 shows particle translation in the yz plane for the dense glass beads specimen (GB-D-400 kPa) sheared under σ_3 = 400 kPa. The specimen began to show a preferred shearing direction as a precursor for a potential shear band at the peak PSR, $\varepsilon_1 = 3.63\%$ (Figure 10c). As shearing progressed, the translation map in the yz plane indicates that there is a failure through a shear band. However, Figure 11 shows the translation in the xz plane (orthogonal to yz plane) of the same specimen, where another competing shear band develops at the upper left side of the specimen at the same strain (Figure 11c) and continues to develop until the end of the experiment (Figure 11g). Figure 12, and Figure 13 show particle rotations for GB-D-400kPa in the yz and xz planes, respectively, where particle rotation did not show a concentration of high rotation gradients along the shear bands because uniform spherical particles with a uniform smooth surface texture, roundness, and sphericity resulted in a much higher particle rotation angle (as high as 40^o compared to 20^o for the other sand specimen). The GB-D-400kPa specimen failed through multiple shear bands rather than one well-defined shear band. The relatively high confining pressure is conducive for forcing shearing along a well-defined single shear band for a dense specimen; however, smooth spherical GB particl.es make it easy for particles to rotate relative to each other, and there is insufficient interlocking between particles to mobilize shear along a single shear band.

The #1 Dry Glass sand specimen (DG-D-400kPa) initially showed a preferred shearing direction at $\varepsilon_1 = 3.57\%$ and $\varepsilon_1 = 5.09\%$ (Figure 14c & d) and a nucleation of

particle rotations initiated at an inclined direction in the specimen at the same axial strains (Figure 15c & d). The deformation mode later changed as the specimen reached its peak PSR at $\varepsilon_1 = 7.13\%$ (Figure 14e) where a cone-shaped high particle translation field developed throughout the top half of the specimen forcing a bulge in the middle portion of the specimen with multiple shear surfaces and high translation fields that are cut off at the bottom of the specimen with an arched transition zone bordering the particles with close to zero translation (Figure 14h). Figure 15e shows that rotations concentrated within the middle half of the specimen. Again, one would expect an angular dense specimen tested under high confining pressure to fail through a single shear band. However, DG sand has the highest angularity of roundness classification (Table 2), which appears to be the main morphology factor affecting strain localization for dense specimens tested under high confining pressure. As the specimen tries to fail along a single shear band, high interlocking develops, causing a high resistance to shearing that forces the development of multiple small shear bands and a zone of high dilation in the middle part of the specimen. It is interesting to note that DG-D-400kPa exhibited the smallest degree of softening when compared to the other specimens in Figure 2 since it continued to resist shearing with a high degree of interlocking between particles whereas a single shear band causes a drop in PSR for F35-D-400kPa and GS40-D-400kPa.

Dense specimens tested under low confining pressure ($\sigma_3 = 15$ kPa)

Figure 16 through Figure 22 show the results for the dense specimens tested under low confining pressures (σ_3 = 15 kPa) where all specimens exhibited failures through a moderate to a significant bulging. The translations for all specimens follow the same trend

where specimens exhibit a cone-shaped high translation zone bounded by particles displacing downwards at smaller translation rates; this behavior is illustrated in Figure 16e for the glass beads (GB-D-15kPa), Figure 17e for GS40-D-15kPa, Figure 19e for F35-D-15kPa, and Figure 21e for DG-D-15kPa. The reason behind the smaller downwards translation of the bordering particles is due to their outward lateral translation; those particles are followed by particles with close to zero translation.

At $\sim\varepsilon_1 = 17.5\%$, all specimens display a transition from a high translation cone-shaped region to an arched transition zone that separates the particles with high translation on the top of transition zone from the particles with very low translation below it. It can be seen from Figure 21g that very angular DG-D-15kPa has a well-defined symmetrical arch transition zone whereas such zone symmetry is lost for angular GS40-D-15kPa (Figure 17h) and rounder F35-D-15kPa (Figure 19h). The left side of the transition zone of GS40-D-15kPa (Figure 17h) showed an increase in thickness as the translation began to show a preference for a more inclined translation gradient. A similar translation mode was also observed in the last translation increment of F35-D-15kPa (Figure 19i). This behavior was not captured in the glass beads because the last scan was acquired before 17.5% axial strain was reached due to scan beam time limitation.

Spatial distributions of particle rotations are also highly influenced by roundness index. The very angular dry glass sand specimen (DG-D-15kPa) exhibited a concentration of particle rotations in the middle part of the specimen as early as $\varepsilon_1 = 1.9\%$ (Figure 22a) caused by a high degree of interlocking, followed by angular GS40-D-15kPa where particle rotations showed localized rotations at $\sim\varepsilon_1 = 3.5\%$ (Figure 18c) where particle rotations

are few in number, highly dispersed, and have very low angles of rotation. Particle rotations for the rounder F35-D-15kPa began at the same strain increment as the GS40-D-15kPa, but the rotations were more localized and were higher in number and value (Figure 20c). As loading continued, the rotations became more localized and increased in number and value in all sands, but rotations were highest for F35-D-15kPa Figure 20h & i) in comparison to DG-D-15kPa (Figure 22g) and GS40-D-15kPa (Figure 18h).

Loose specimens tested under low confining pressure ($\sigma_3 = 15$ kPa)

The particle kinematics of the loose DG and F35 specimens are depicted in Figure 23 through Figure 26. Both DG-L-15kPa and F35-L-15kPa failed via bulging mode with considerable particle translation and rotation. The DG-L-15kPa specimen shows unusually high initial particle translation at the top half of the specimen (Figure 23a) most likely caused by loose packing and low confining pressure that resulted in a denser state and consequently nearly uniformly distributed translation (Figure 23b) that eventually evolved into a conical top pushing down, causing particles to deform in the lateral direction in the middle of the specimen. Particles rotation (Figure 24b) spread over a larger portion of the specimen when compared to DG-D-15kPa due to more void space for particles to rotate as they translate. F35-L-15kPa exhibits less volume dilation (marked by less void space) than F35-D-15kPa (Figure 25 compared to Figure 19 and Figure 4 compared to Figure 3). Also, particle rotations within F35-L-15kPa have smaller values and develop at larger axial strains than particles within F35-D-15kPa indicating that more void space in loose specimens is conducive to less rotation (less interlocking) for relatively rounded particles.

Conclusions

The paper investigated the influence of particle surface texture, roundness, sphericity, confining pressure, and specimen density on the deformation and failure mode of dry uniform sand specimens tested under drained triaxial condition. The following conclusions are drawn from the paper:

1. Particle roundness is the major factor that influences the development of a single well-defined shear band or a bulging failure mode for dense specimens tested under high confining pressure (σ_3 = 400 kPa). Bulging mode is just an external manifestation of intense shearing involving a large number of particles. Sphericity and surface texture are not the deciding parameters for dense specimens tested under high confining pressure.
2. The smooth surface texture of round, spherical glass beads causes high degrees of particle rotation—up to 40^o— which do not concentrate around shearing bands with no preferred distribution of particles with high rotation. The lack of interlocking between particles causes high rotations, and the development of multiple shear bands for the dense GB specimen tested under σ_3 = 400 kPa.
3. Dense specimens tested under low confining pressure (σ_3 = 15 kPa) fail via bulging, which is an external manifestation of a complex internal shear pattern. The low confining pressure allows a higher degree of freedom for the specimen to expand laterally and develop multiple shearing planes. Particle rotation is influenced by particle roundness index; rotation decreases as angularity increases.

4. The failure mode of loose specimens tested under low confining pressure (σ_3 = 15 kPa) is similar to that of dense specimens under low confining pressure except for the availability of more void space for particles to translate and less particle rotation due to less contact between particles in loose packing.

References

Al-Raoush, R. (2007). "Microstructure characterization of granular materials." *Physica A: Statistical Mechanics and its Applications*, 377(2), 545-558.

Alshibli, K., and Sture, S. (2000). "Shear Band Formation in Plane Strain Experiments of Sand." *Journal of Geotechnical and Gezoenvironmental Engineering*, 126(6), 495-503.

Alshibli, K. A., and Al-Hamdan, M. Z. (2000). "Assessment of internal fabric of particulate materials." *Dev Arid Reg Res Ser*, 1, 115-122.

Alshibli, K. A., and Alramahi, B. A. (2006). "Microscopic evaluation of strain distribution in granular materials during shear." *Journal of Geotechnical and Geoenvironmental Engineering*, 132(1), 80-91.

Alshibli, K. A., Batiste, S. N., and Sture, S. (2003). "Strain localization in sand: Plane strain versus triaxial compression." *Journal of Geotechnical and Geoenvironmental Engineering*, 129(6), 483-494.

Alshibli, K. A., Druckrey, A. M., Al-Raoush, R. I., Weiskittel, T., and Lavrik, N. V. (2015). "Quantifying Morphology of Sands Using 3D Imaging." *J Mater Civil Eng*, 27(10).

Alshibli, K. A., and Reed, A. H. (2010). *Advances in Computed Tomography for Geomaterials: GeoX 2010*, Wiley.

Alshibli, K. A., Sture, S., Costes, N. C., Frank, M. L., Lankton, M. R., Batiste, S. N., and Swanson, R. A. (2000). "Assessment of localized deformations in sand using X-ray computed tomography." *Geotech Test J*, 23(3), 274-299.

Andò, E., Hall, S., Viggiani, G., Desrues, J., and Bésuelle, P. (2012). "Grain-scale experimental investigation of localised deformation in sand: a discrete particle tracking approach." *Acta Geotech.*, 7(1), 1-13.

Batiste, S. N., Alshibli, K. A., Sture, S., and Lankton, M. (2004). "Shear band characterization of triaxial sand specimens using computed tomography." *Geotech Test J*, 27(6), 568-579.

Desrues, J., and Ando, E. (2015). "Strain localisation in granular media." *Cr Phys*, 16(1), 26-36.

Desrues, J., Chambon, R., Mokni, M., and Mazerolle, F. (1996). "Void ratio evolution inside shear bands in triaxial sand specimens studied by computed tomography." *Géotechnique*, 46(3), 529-546.

Desrues, J., and Hammad, W. (1989). "Shear Banding Dependency on Mean Stress Level in Sand." *Numerical Methods for Localization and Bifurcation of Granular Bodies*, Institute of Soil Mechanics and Rock Mechanics, Technical University of Karlsruhe

Desrues, J., Lanier, J., and Stutz, P. (1985). "Localization of the deformation in tests on sand sample." *Engineering Fracture Mechanics*, 21(4), 909-921.

Desrues, J., Viggiani, G., and Bésuelle, P. (2006). *Advances in X-ray Tomography for Geomaterials*, Wiley-ISTE, Great Britain.

Druckrey, A., and Alshibli, K. (2014). "3D Behavior of Sand Particles Using X-Ray Synchrotron Micro-Tomography." *Geo-Congress 2014 Technical Papers*, American Society of Civil Engineers, 2814-2821.

Druckrey, A. M., Alshibli, K., and Al-Raoush, R. (2015). "3D Characterization pf Sand Particle-to-Particle Contact and Morphology." *Computers and Geotechnics*. under review.

Finno, R. J., Harris, W. W., Mooney, M. A., and Viggiani, G. (1997). "Shear bands in plane strain compression of loose sand." *Géotechnique*, 47(1), 149-165.

Hall, S. A., Bornert, M., Desrues, J., Pannier, Y., Lenoir, N., Viggiani, G., and Besuelle, P. (2010). "Discrete and continuum analysis of localised deformation in sand using X-ray mu CT and volumetric digital image correlation." *Géotechnique*, 60(5), 315-322.

Han, C., and Drescher, A. (1993). "Shear Bands in Biaxial Tests on Dry Coarse Sand " *Soils and Foundations*, 33(1), p. 118-132.

Hasan, A., and Alshibli, K. (2012). "Three dimensional fabric evolution of sheared sand." *Granular Matter*, 14(4), 469-482.

Kinney, J. H., and Nichols, M. C. (1992). "X-Ray Tomographic Microscopy (XTM) Using Synchrotron Radiation." *Annual Review of Materials Science*, 22(1), 121-152.

Lee, K. L. (1970). "Comparison of Plane Strain and Triaxial Tests on Sand." *Journal of the Soil Mechanics and Foundations division, ASCE*, 96(3), 901-923.

Marachi, N., Duncan, J., Chan, C., and Seed, H. (1981). "Plane-Strain Testing of Sand." *Laboratory Shear Strength of Soils , ASTM STP 740*, R. N. Yong and F. C. Townsend, eds., American Society for Testing and Materials, 294-302.

Matsushima, T., Katagiri, J., Uesugi, K., and Nakano, T. (2006). "Micro X-ray CT at SPring-8 for Granular Mechanics." *Geotechnical Symposium* Roma.

Matsushima, T., Katagiri, J., Uesugi, K., and Nakano, T. "Micro X-ray CT at SPring-8 for Granular Mechanics." *Proc., Soil stress-strain behavior: measurement, modeling and analysis*, Springer, 225-234.

Otani, J., and Obara, Y. (2004). *X-Ray CT for Geomaterials: Soils, Concrete, Rocks.*, Swets & Zeitlinger B.V., Lisse, The Netherlands.

Peric, D., Runesson, K., and Sture, S. (1992). "Evaluation of Plastic Bifurcation for Plane Strain versus Axisymmetry." *Journal of Engineering Mechanics*, 118(3), 512-524.

Peters, J., F., Lade, P., V., and Bro, A. (1988). "Shear Band Formation in Triaxial and Plane Strain Tests." *Advanced Triaxial Testing of Soil and Rock, ASTM STP 977*, R. T. Donaghe, R. C. Chaney, and M. L. Silver, eds., American Society for Testing and Materials, Philadelphia, 604-627.

Rechenmacher, A. L. (2006). "Grain-scale processes governing shear band initiation and evolution in sands." *Journal of the Mechanics and Physics of Solids*, 54(1), 22-45.

Sjodahl, M., Siviour, C. R., and Forsberg, F. (2012). "Digital volume correlation applied to compaction of granular materials." *Proc Iutam*, 4, 179-195.

Viggiani, G., Ando, E., Jaquet, C., and Talbot, H. (2013). "Identifying and following particle-to-particle contacts in real granular media: an experimental challenge." *Aip Conf Proc*, 1542, 60-65.

Appendix

Table 1. Properties of sands and glass beads

Material	G_s	d_{50} (mm)	e_{min}	e_{max}	Source	Supplier	Grain Size
F-35 Ottawa Sand (F35)	2.650	0.36	0.570	0.763	Ottawa, IL, USA	US Silica Company	Size fraction between US sieves #40 (0.42 mm) and #50 (0.297 mm)
#1 Dry Glass Sand (DG)	2.650	0.36	0.715	0.947	Berkeley Springs, WV, USA		
GS#40 Columbia Grout Sand (GS40)	2.650	0.36	0.693	0.946	Columbia, SC, USA		
Glass beads (GB)	2.550	0.36	0.686	0.800	Soda lime glass	Jaygo inc.	

Table 2. Mean values of morphology indices and their standard deviations (SD)

Material	I_{sph}			I_R			R_q (μm)		
	Mean	SD	Rank*	Mean	SD	Rank*	Mean	SD	Rank*
Glass beads (GB)	1.096	0.433	Spherical ↑ GB	0.965	0.043	Round ↑ GB	0.381	0.947	Smoother ↑ GB
F-35 Ottawa Sand (F35)	1.872	0.732	GS40	0.959	0.083	F35	2.084	1.693	GS40
#1 Dry Glass Sand (DG)	1.704	0.859	DG	0.937	0.106	GS40	1.990	1.135	DG
GS#40 Columbia Grout Sand (GS40)	1.674	0.799	F35 ↓ Non-spherical	0.924	0.099	DG ↓ Angular	1.923	1.986	F35 ↓ Rough

* Ranking is based on statistical distribution which incudes mean, SD and other statistical parameters now shown in this paper

Table 3. Properties of the tested specimens

Material	Exp.	Initial void ratio	σ_3 (kPa)	D_r (%)	Specimen height (mm)	Specimen diameter (mm)	Scan acquired at axial compression (mm)	Resolution, (μm/voxel)
F-35 Ottawa sand (F35)	F35-L-15kPa	0.668	15	49	19.64	10.23	0.0, 0.2, 0.4, 0.7, 1.0, 1.4, 1.8, 2.4, 3.1, 3.9	8.16
	F35-D-15kPa	0.603	15	83	20.16	10.77	0.0, 0.2, 0.4, 0.7, 1.0, 1.4, 1.8, 2.4, 3.5, 4.5	11.14
	F35-D-400kPa	0.586	400	91	20.35	10.41	0.0, 0.2, 0.4, 0.7, 1.0, 1.4, 1.8, 2.4	11.18
#1 Dry glass sand (DG)	DG-L-15kPa	0.799	15	64	19.58	10.15	0.0, 0.2, 0.4, 0.7, 1.0, 1.4, 1.8, 2.4, 3.1, 3.9	8.16
	DG-D-15kPa	0.754	15	83	20.11	10.63	0.0, 0.4, 0.7, 1.0, 1.4, 1.8, 2.4, 3.5	11.14
	DG-D-400kPa	0.727	400	95	19.63	10.60	0.0, 0.2, 0.4, 0.7, 1.0, 1.4, 1.8, 2.4, 3.5	11.18
GS#40 Columbia grout sand (GS40)	GS40-D-15kPa	0.721	15	89	19.97	10.41	0.0, 0.2, 0.4, 0.7, 1.0, 1.4, 1.8, 2.4, 3.5	11.14
	GS40-D-400kPa	0.720	400	89	21.03	10.26	0.0, 0.2, 0.4, 0.7, 1.0, 1.4, 1.8, 2.4, 3.1	8.16
Glass beads (GB)	GB-D-15kPa	0.690	15	96	19.7	10.83	0.0, 0.2, 0.4, 0.7, 1.0, 1.4, 1.8, 2.4	11.14
	GB-D-400kPa	0.687	400	99	19.30	10.60	0.0, 0.2, 0.4, 0.7, 1.0, 1.4, 1.8, 2.4	11.18

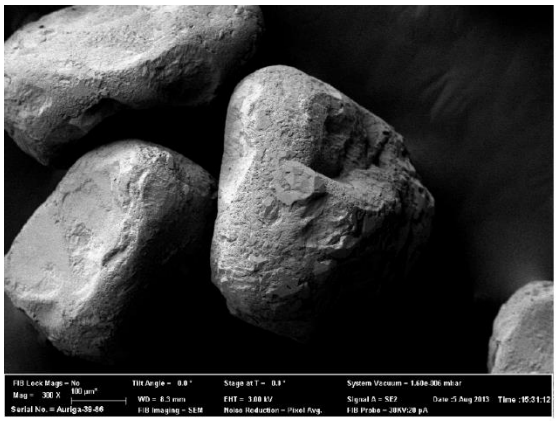

(a) F35 Ottawa Sand

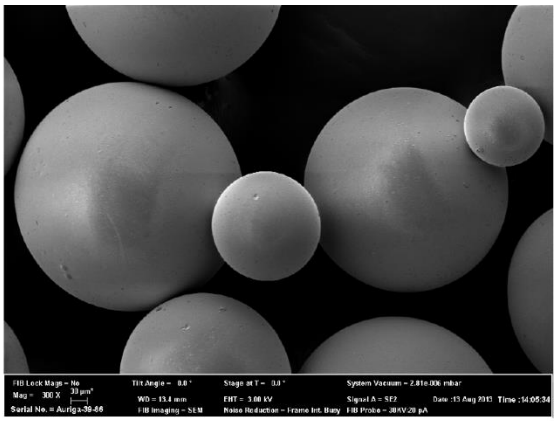

(b) Glass Beads

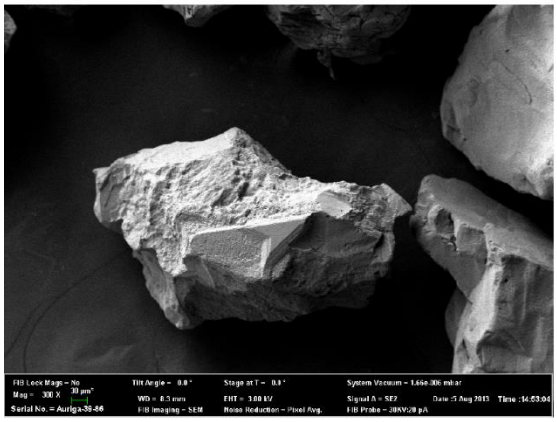

(c) Colombia Grout GS # 40 Sand

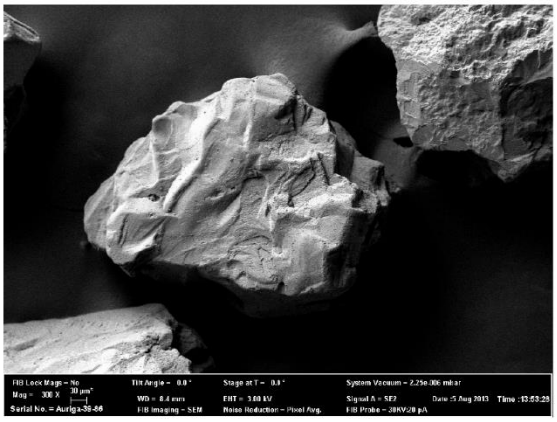

(d) #1 Dry Glass Sand

Figure 1: Scanning Electron Microscope (SEM) images of the sands and the glass beads.

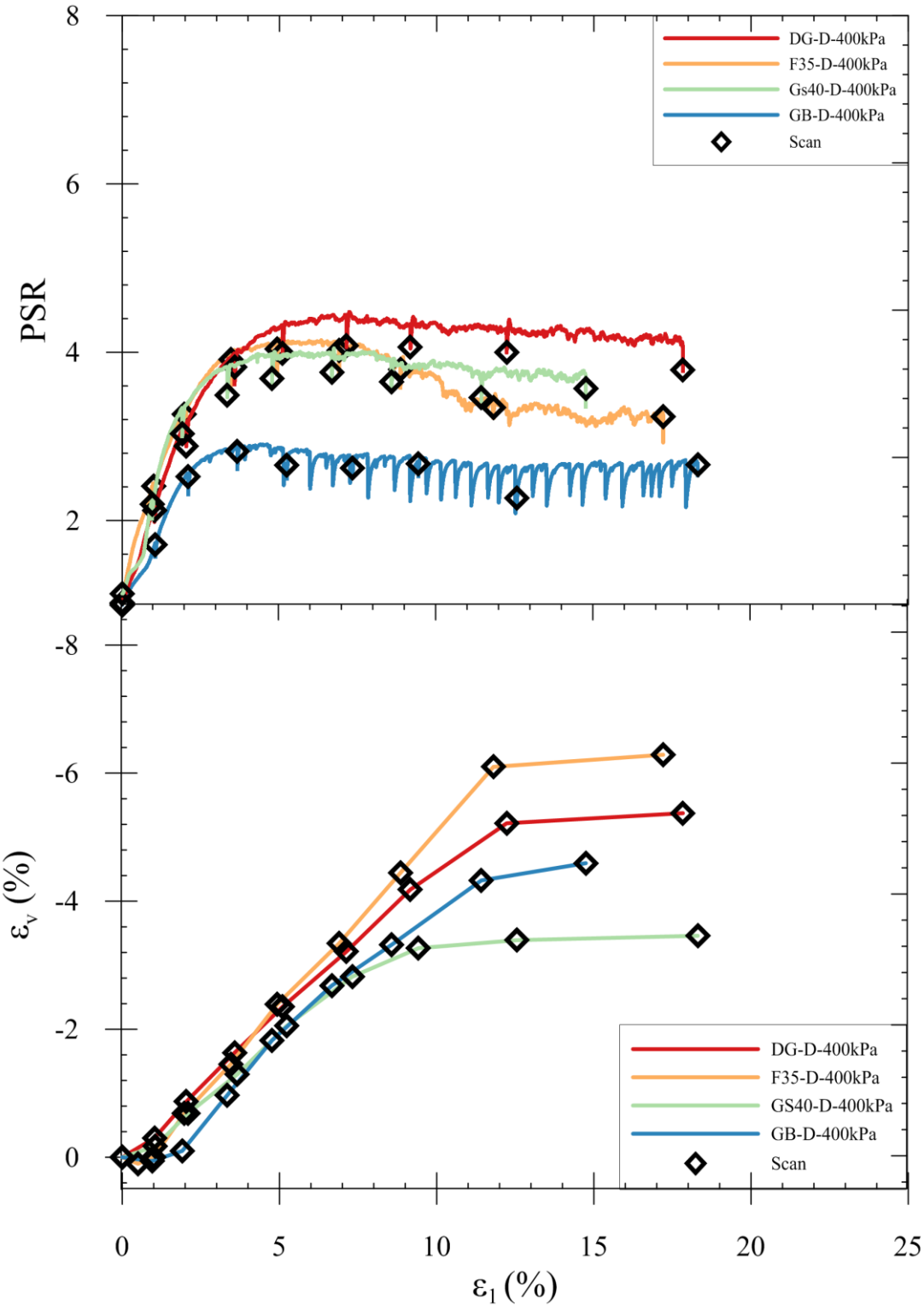

Figure 2. Nominal axial strain versus principal stress ratio (PSR) for dense specimens, σ_3 = 400 kPa

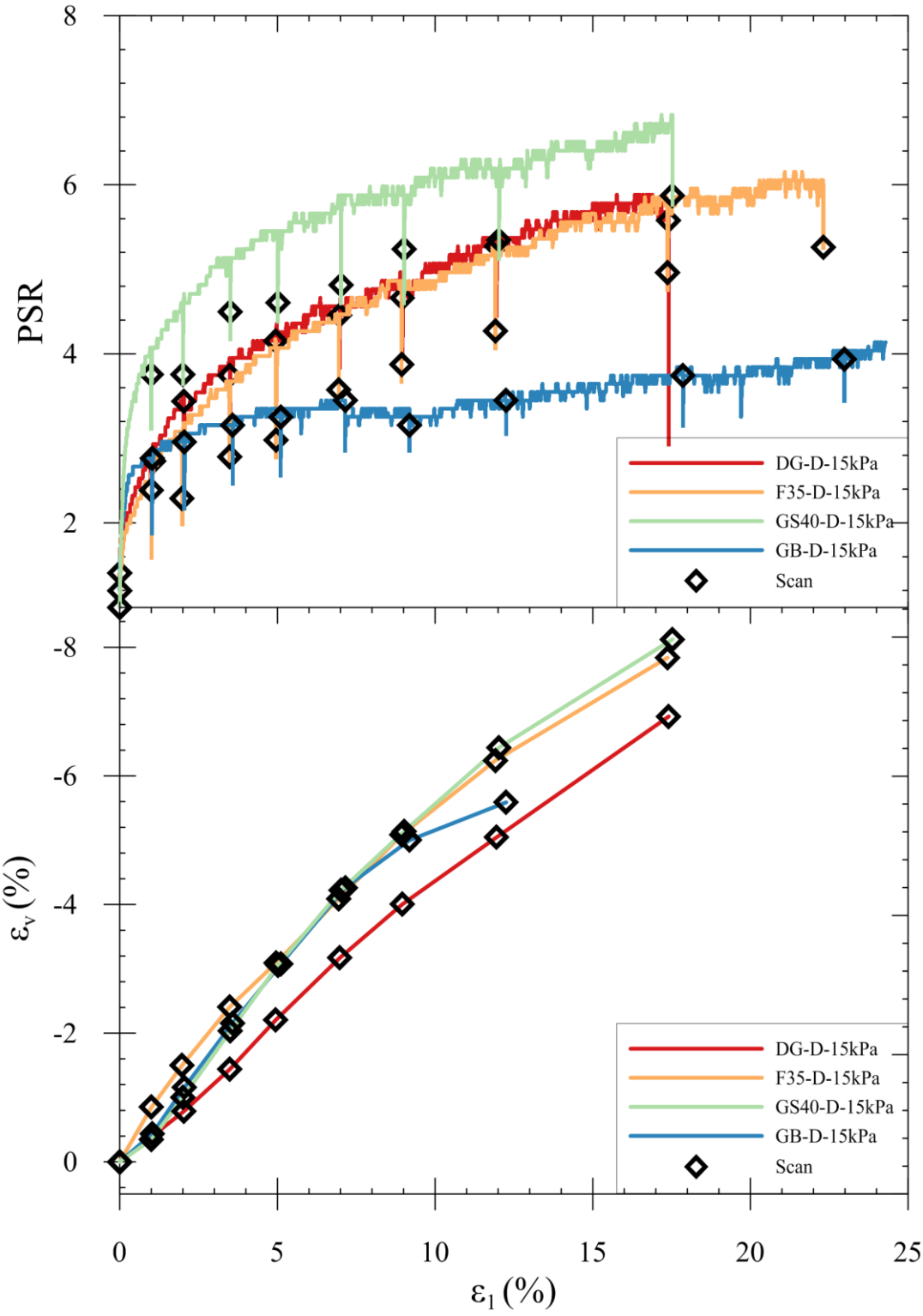

Figure 3. Nominal axial strain versus principal stress ratio (PSR) for dense specimens, σ_3 = 15 kPa

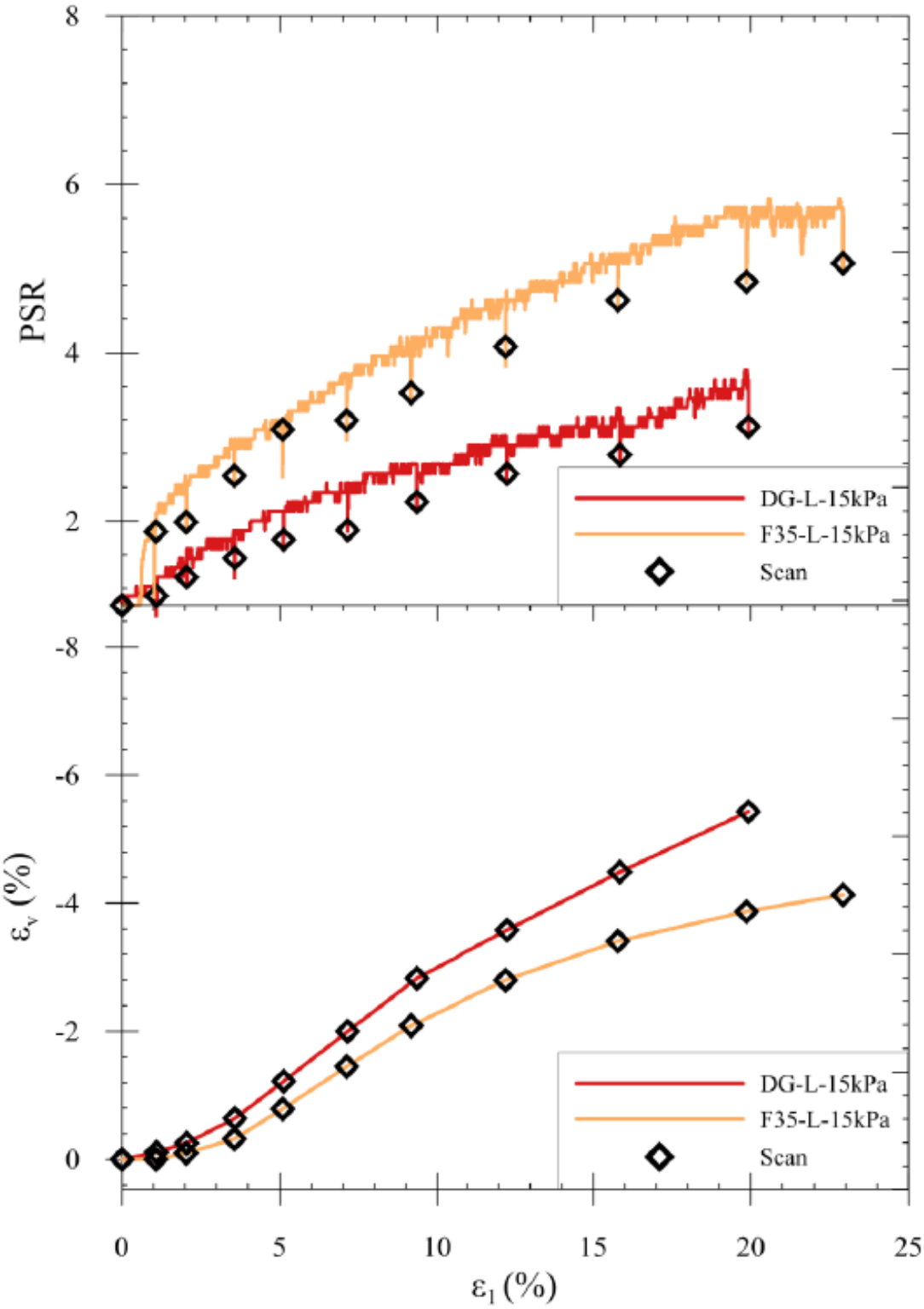

Figure 4. Nominal axial strain versus principal stress ratio (PSR) for loose specimens, σ_3 = 15 kPa

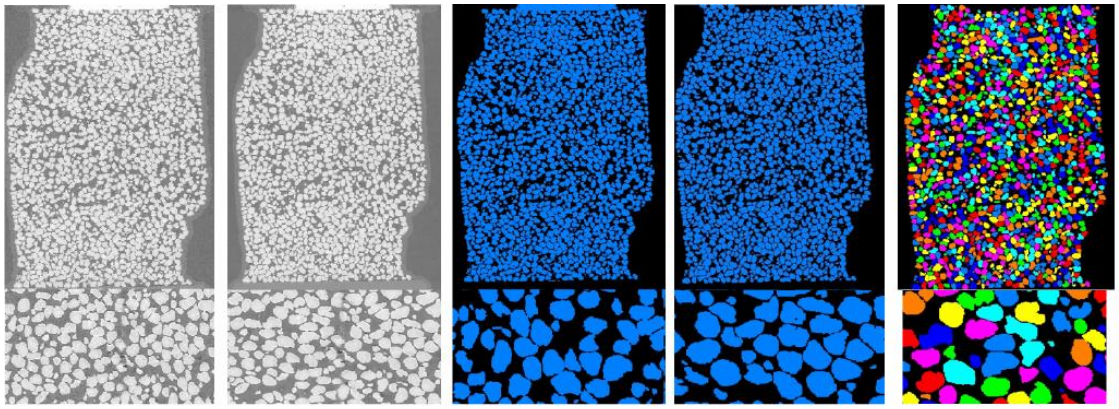

(a) SMT image (b) Filtered image (c) Segmented image (d) Separated particles (e) Labeled particles

Figure 5. Image analysis steps to produce labeled particles

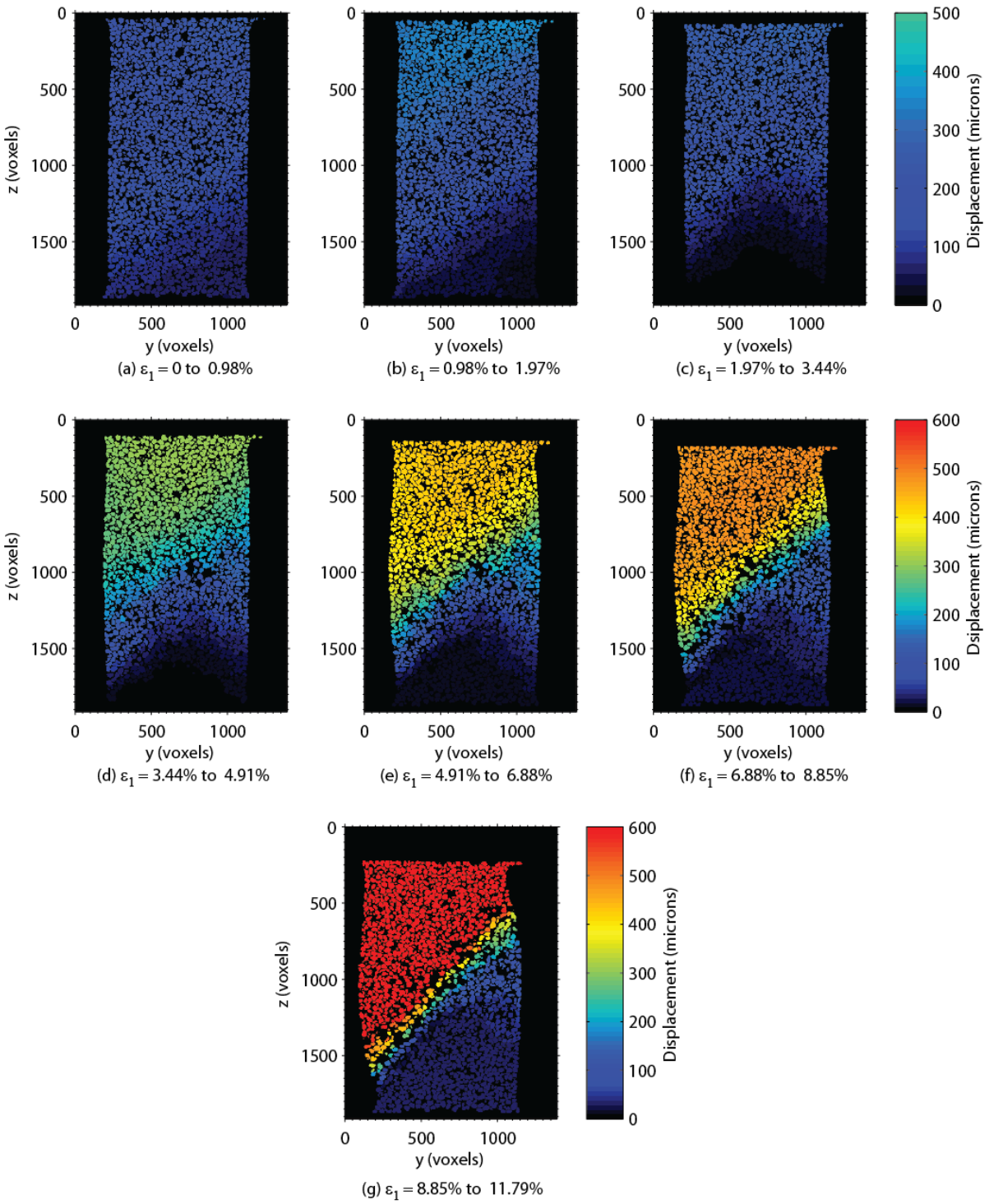

Figure 6. Particle translation for dense F35 sand specimen (F35-D-400kPa) tested under high confining pressure, σ_3 = 400 kPa

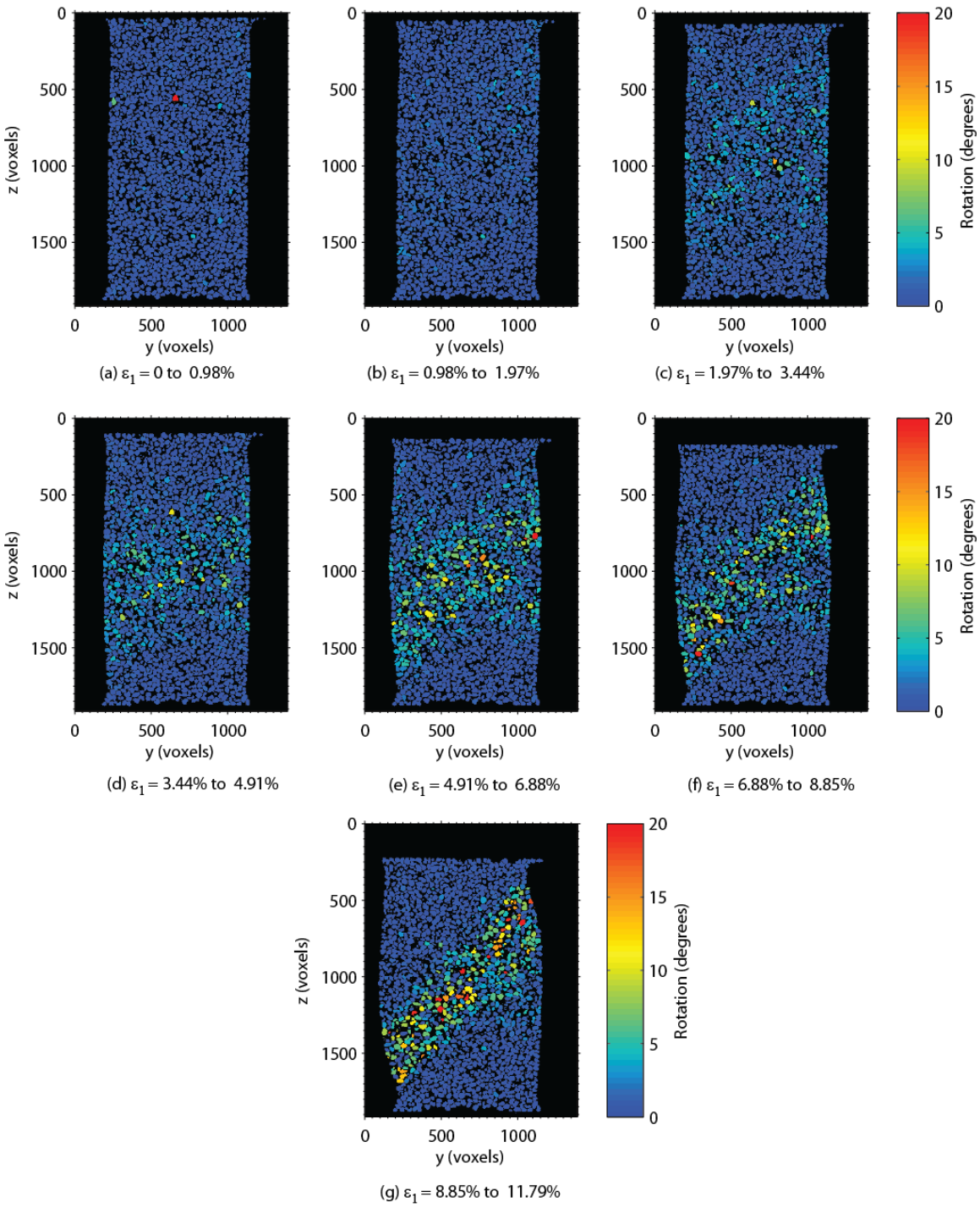

Figure 7. Rotation angle of particles for dense F35 sand specimen (F35-D-400kPa) tested under high confining pressure, σ_3 = 400 kPa

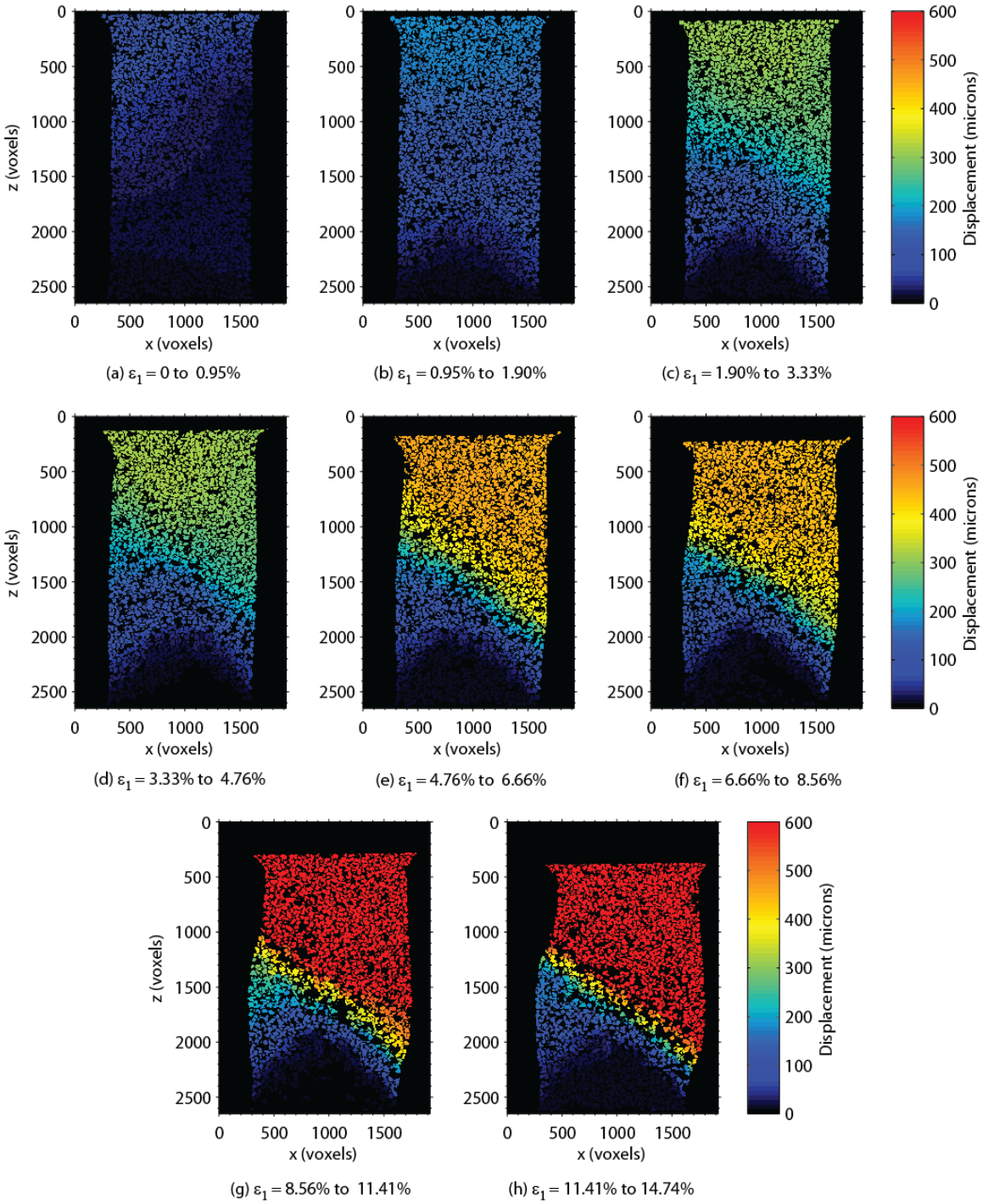

Figure 8. Particle translation for dense GS#40 Columbia Grout sand specimen (GS40-D-400kPa) tested under high confining pressure, σ_3 = 400 kPa

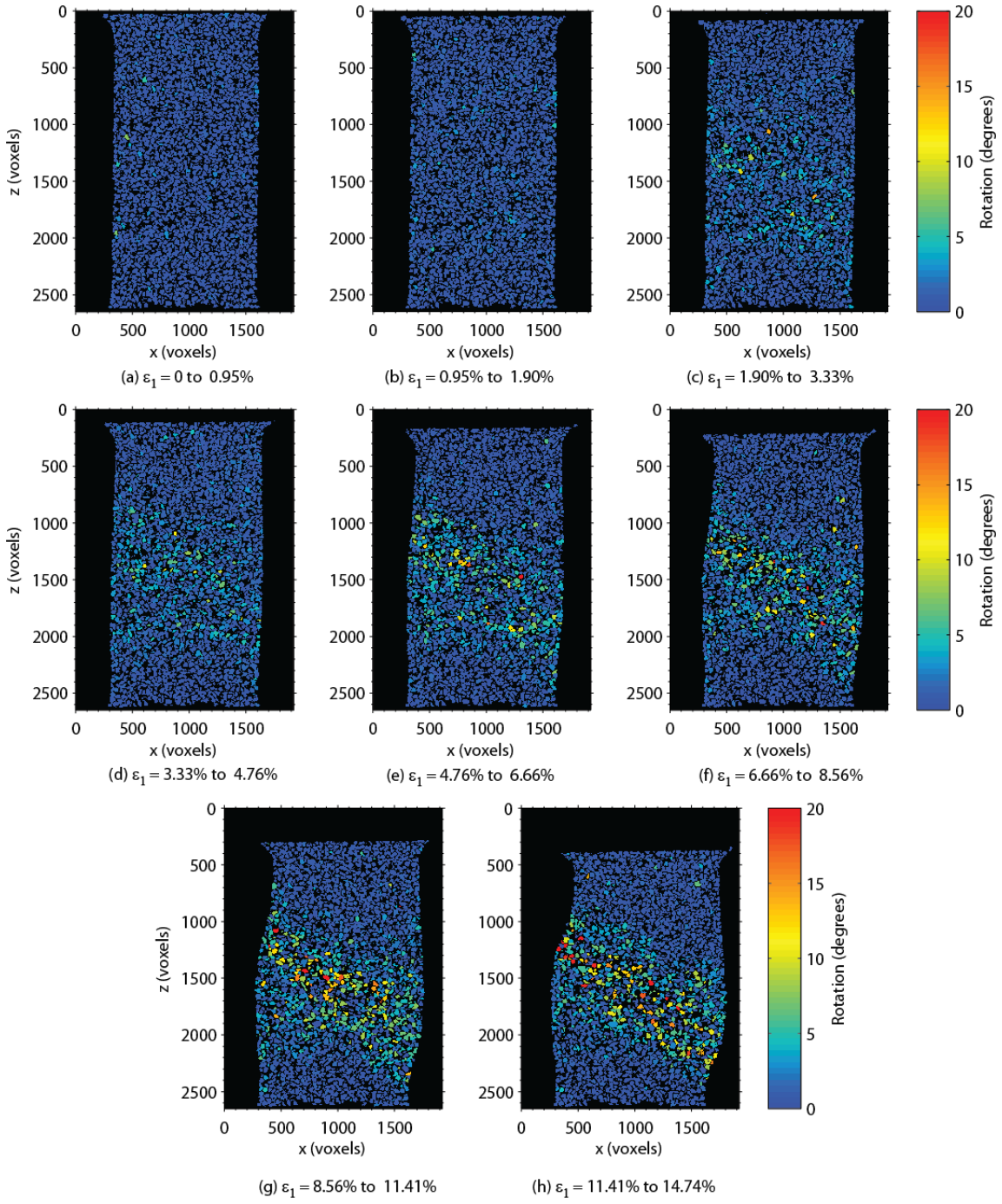

Figure 9: Rotation angle of particles for dense GS#40 Columbia Grout sand specimen (GS40-D-400kPa) tested under high confining pressure, σ_3= 400 kPa.

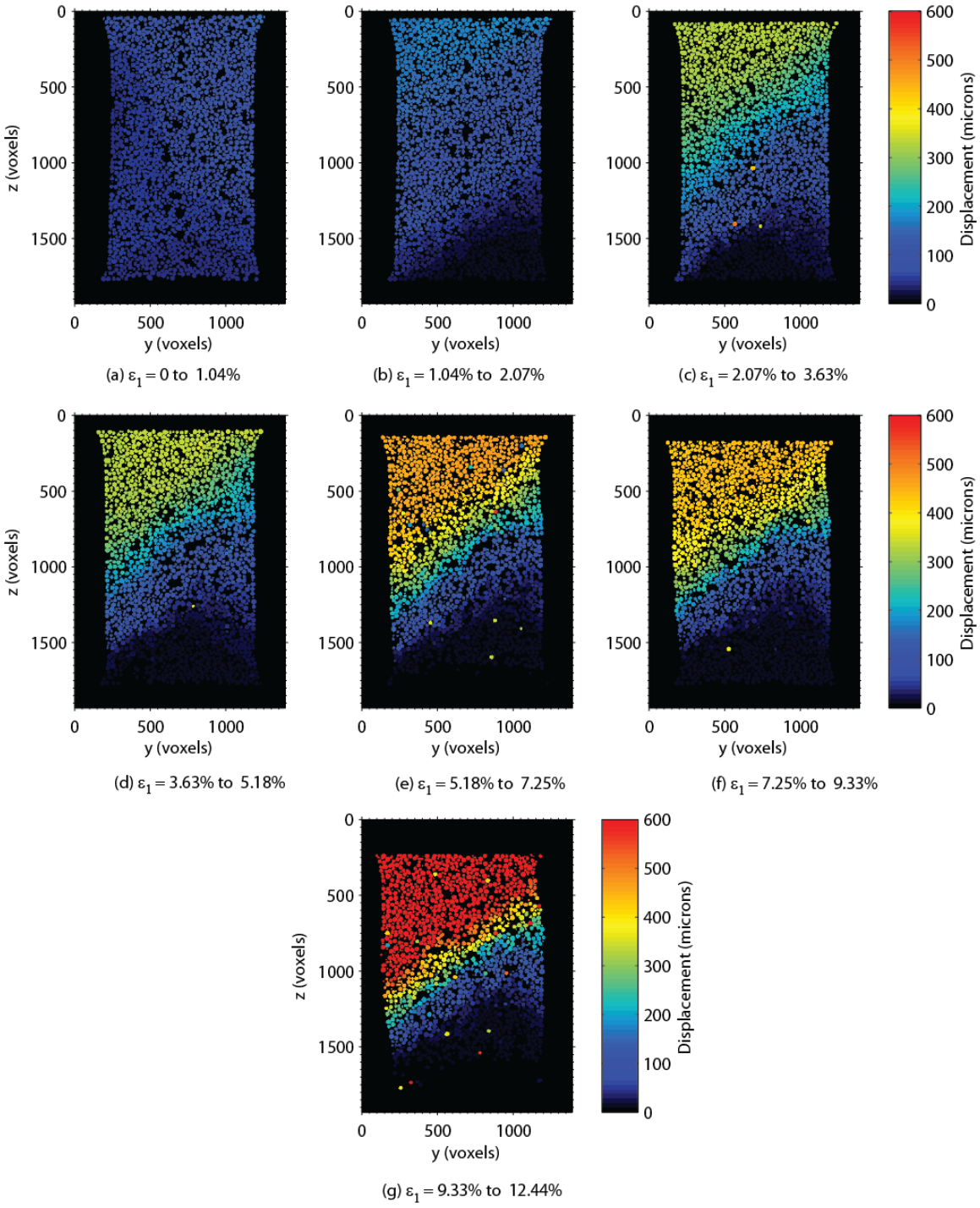

Figure 10. Particle translation for dense glass beads specimen (GB-D-400kPa) tested under high confining pressure, $\boldsymbol{\sigma_3}$ = 400 kPa, yz plane

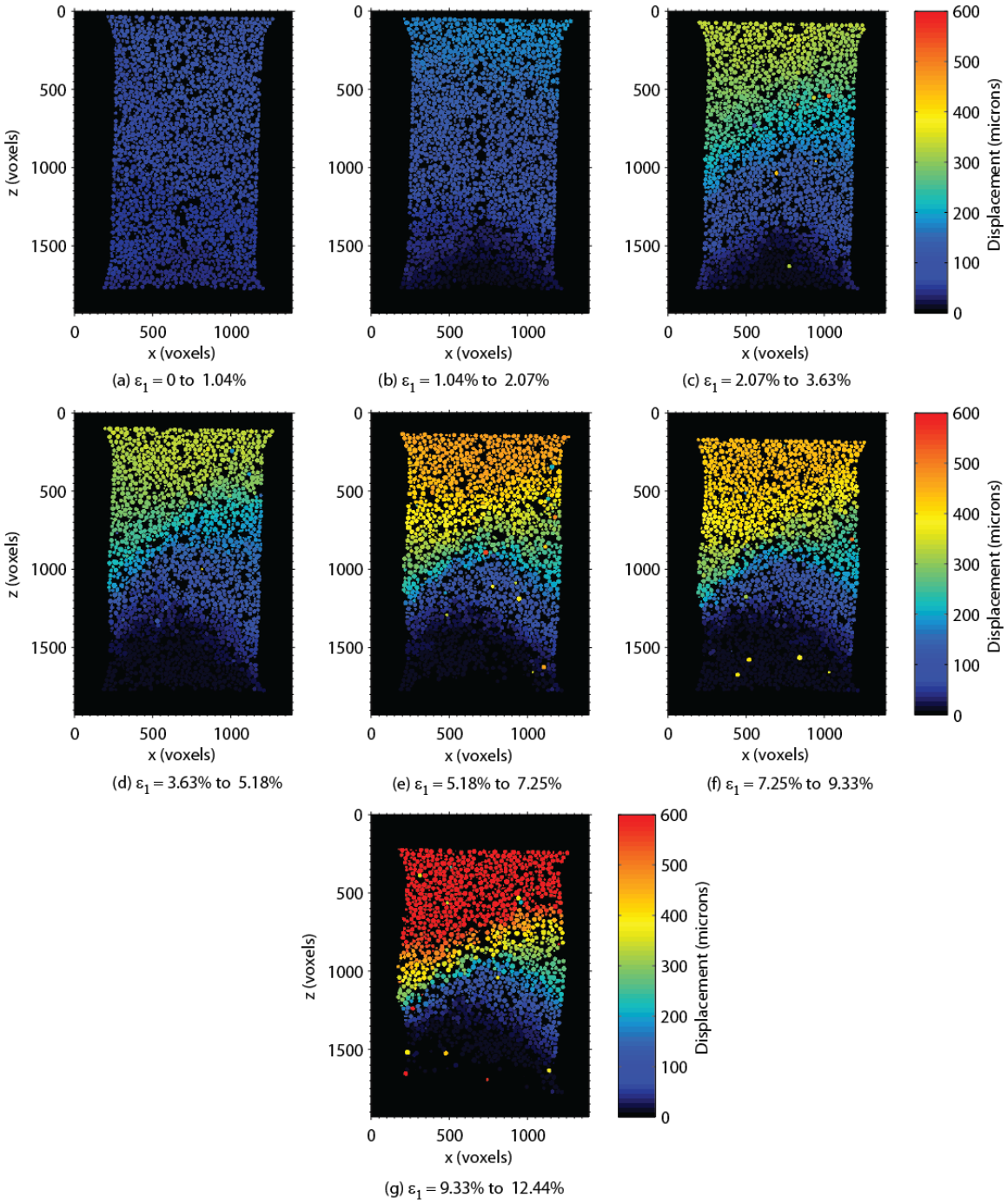

Figure 11. Particle translation for dense glass beads specimen (GB-D-400kPa) tested under high confining pressure, $\boldsymbol{\sigma_3}$ = 400 kPa, xz plane

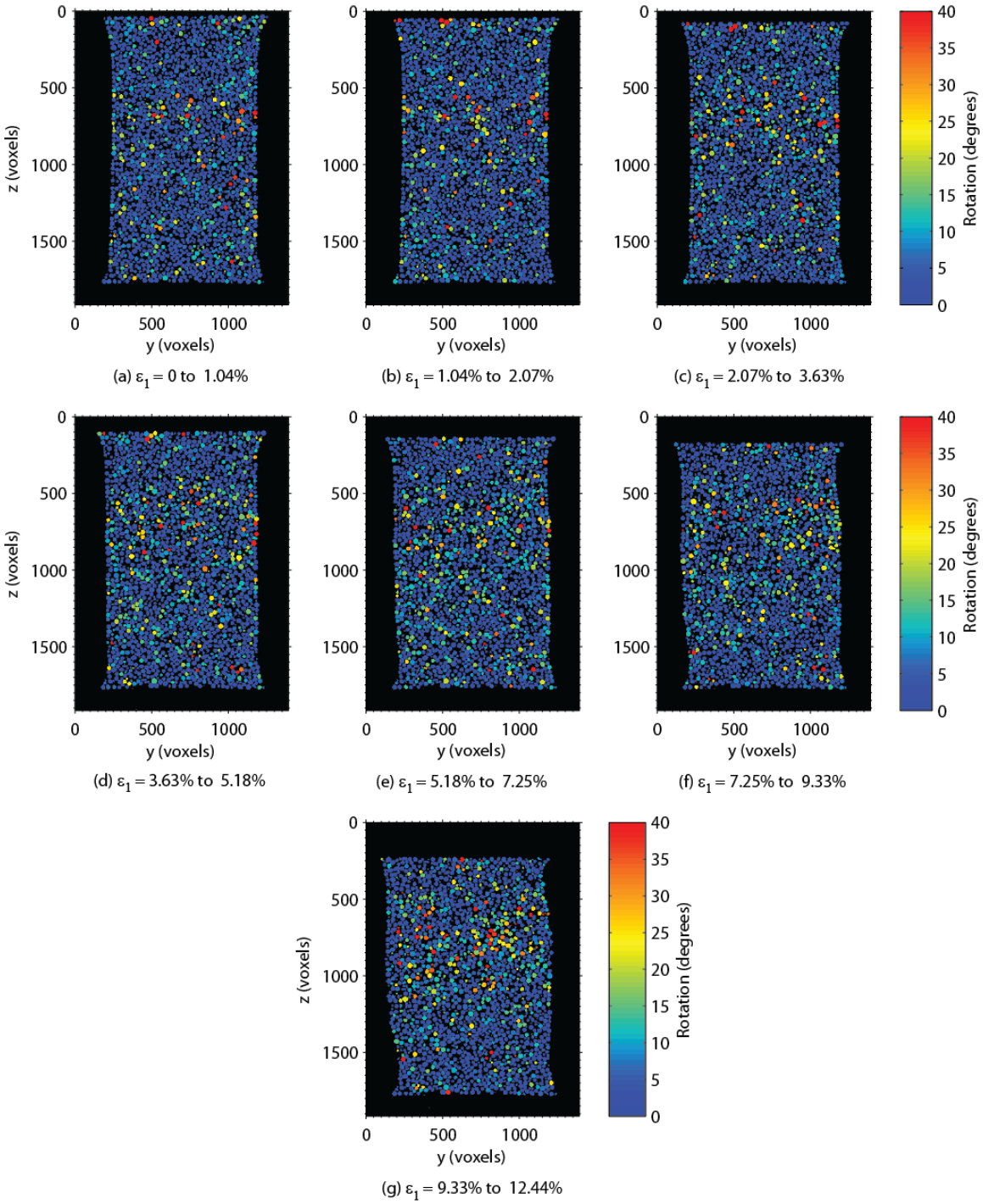

Figure 12. Rotation angle of particles for dense glass beads specimen (GB-D-400kPa) tested under high confining pressure, $\boldsymbol{\sigma_3}$ = 400 kPa, yz plane

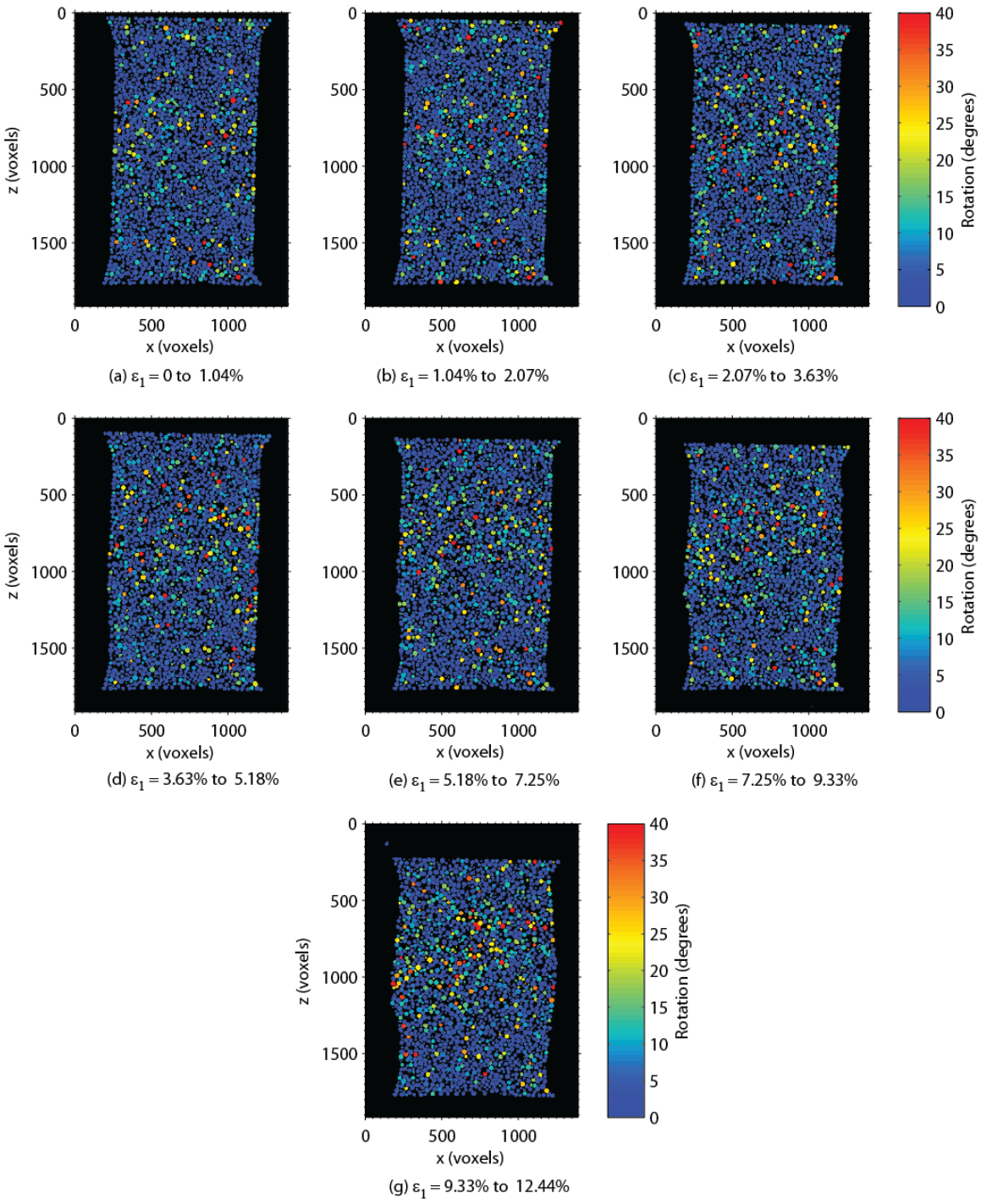

Figure 13. Rotation angle of particles for dense glass beads specimen (GB-D-400kPa) tested under high confining pressure, $\boldsymbol{\sigma_3}$ = 400 kPa, xz plane

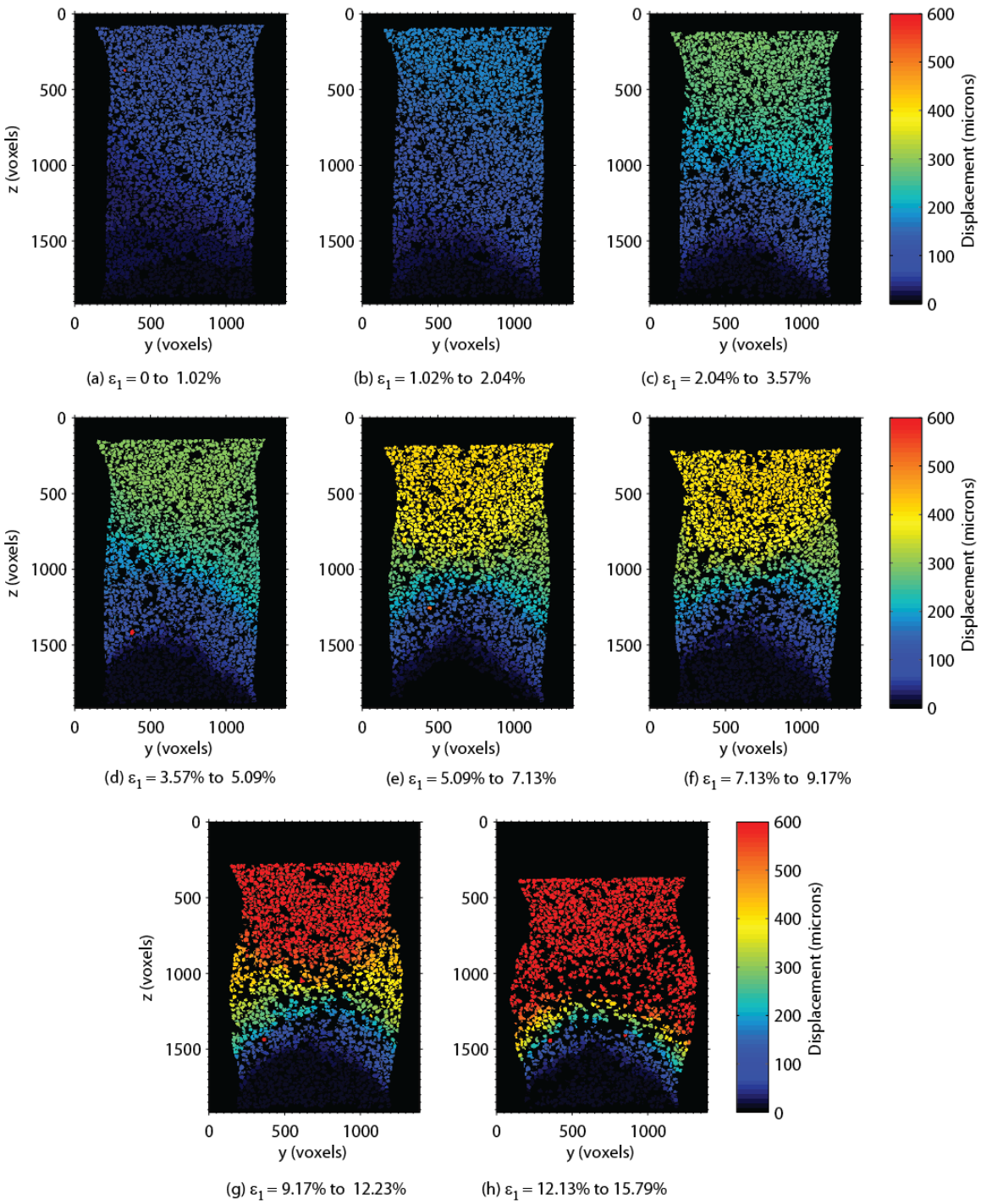

Figure 14. Particle translation for dense #1 dry glass sand specimen (DG-D-400kPa) tested under high confining pressure, $\boldsymbol{\sigma_3}$ = 400 kPa

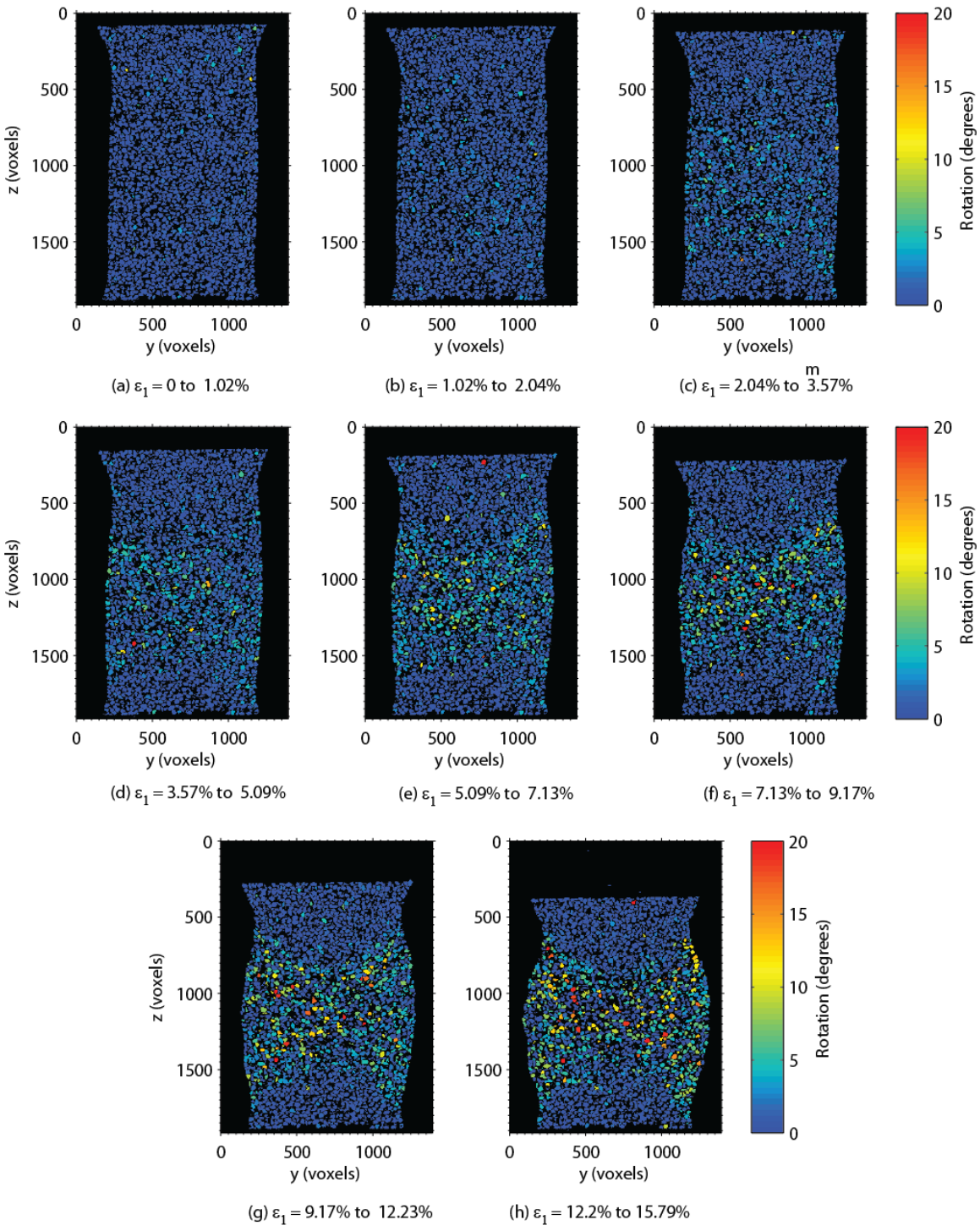

Figure 15. Rotation angle of particles for dense #1 dry glass sand specimen (DG-D-400kPa) tested under high confining pressure, $\boldsymbol{\sigma_3}$ = 400 kPa

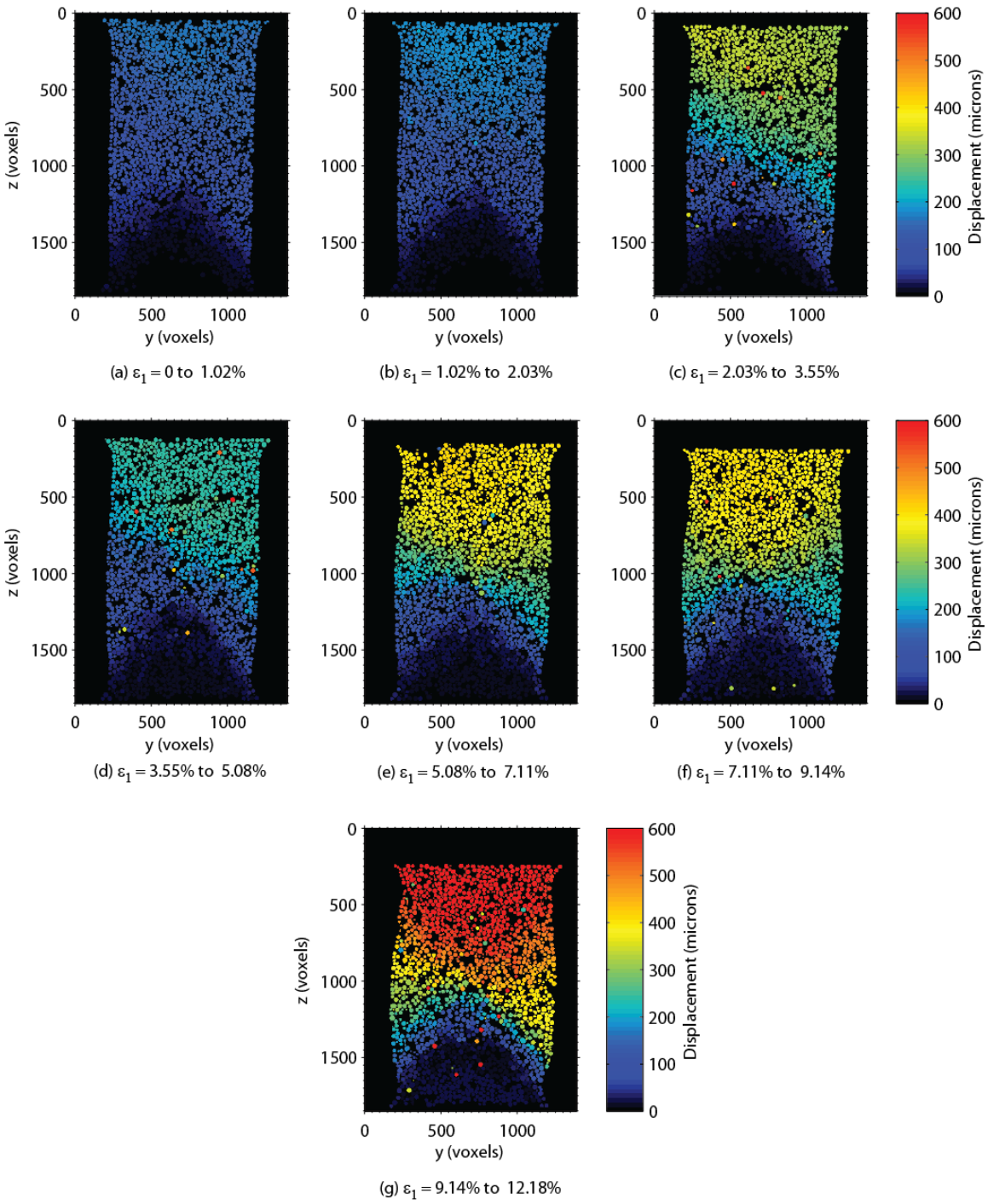

Figure 16. Particle translation for dense glass beads specimen (GB-D-15kPa) tested under low confining pressure, $\boldsymbol{\sigma_3}$ = 15 kPa

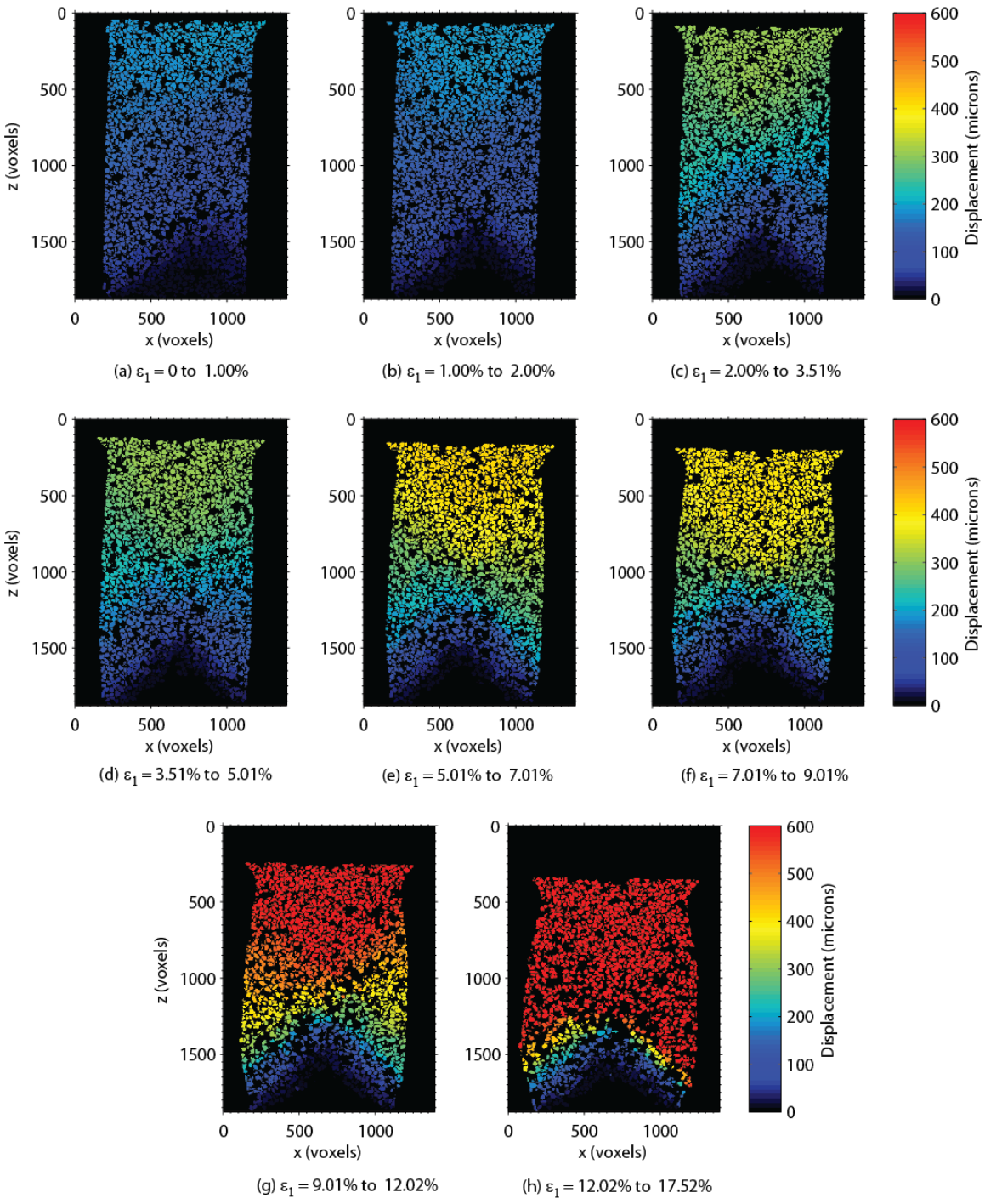

Figure 17. Particle translation for dense GS#40 Columbia Grout sand specimen (GS40-D-15kPa) tested under low confining pressure, $\boldsymbol{\sigma_3}$ = 15 kPa

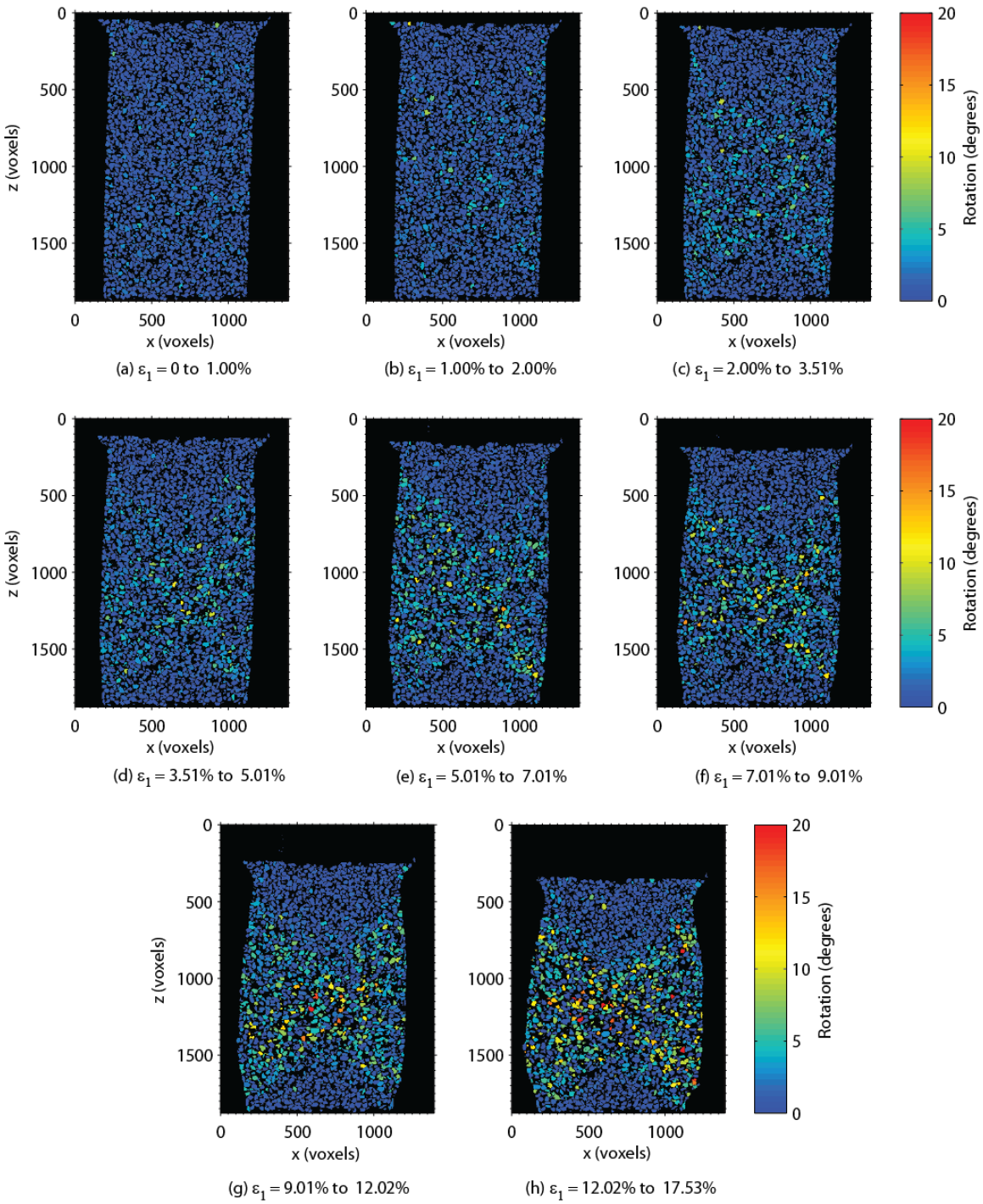

Figure 18. Rotation angle of particles for dense GS#40 Columbia Grout sand specimen (GS40-D-15kPa) tested under low confining pressure, $\boldsymbol{\sigma_3}$ = 15 kPa

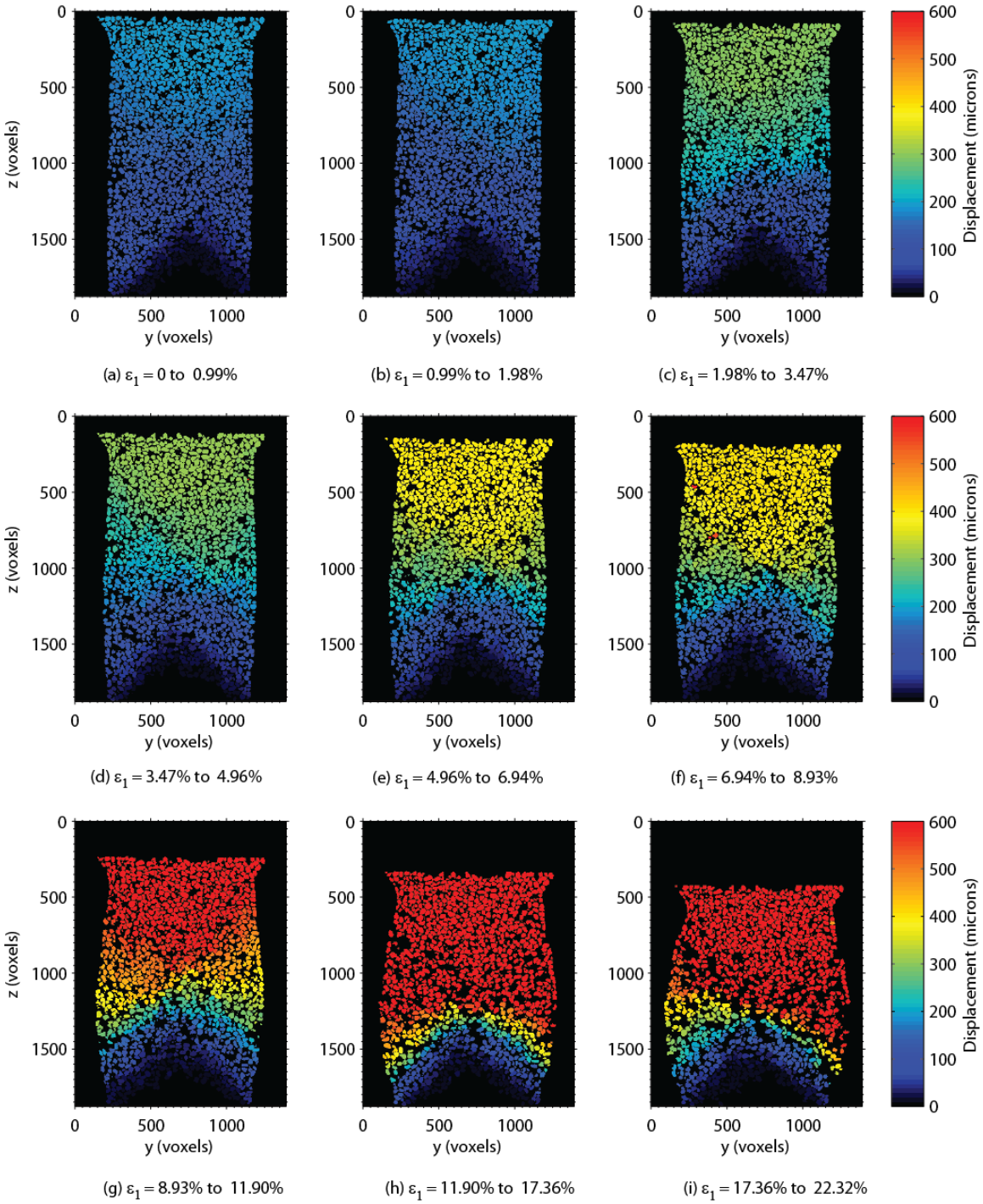

Figure 19. Particle translation for dense F35 sand specimen (F35-D-15kPa) tested under low confining pressure, $\boldsymbol{\sigma_3}$ = 15 kPa

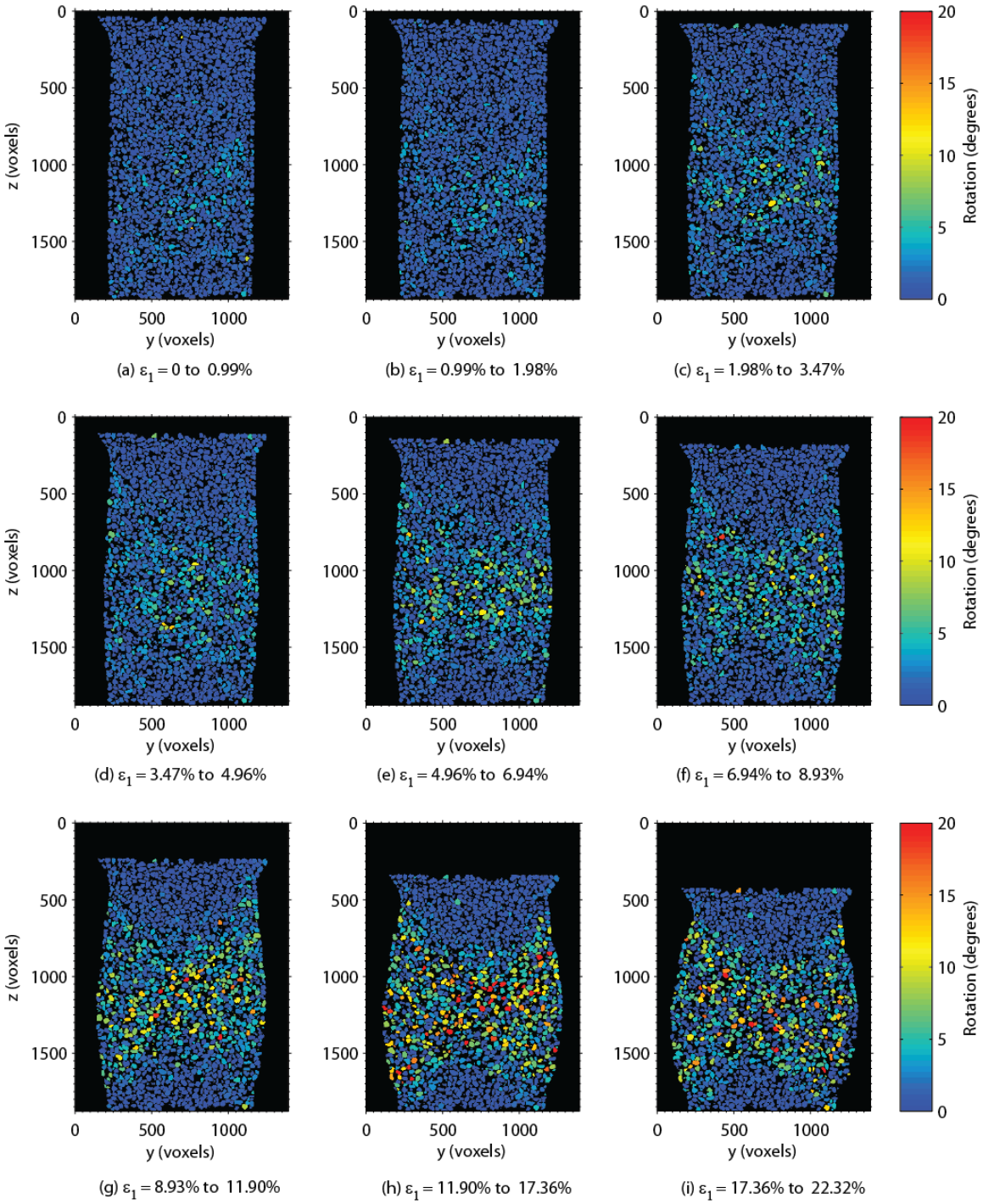

Figure 20. Rotation angle of particles for dense F35 sand specimen (F35-D-15kPa) tested under low confining pressure, $\boldsymbol{\sigma_3}$ = 15 kPa

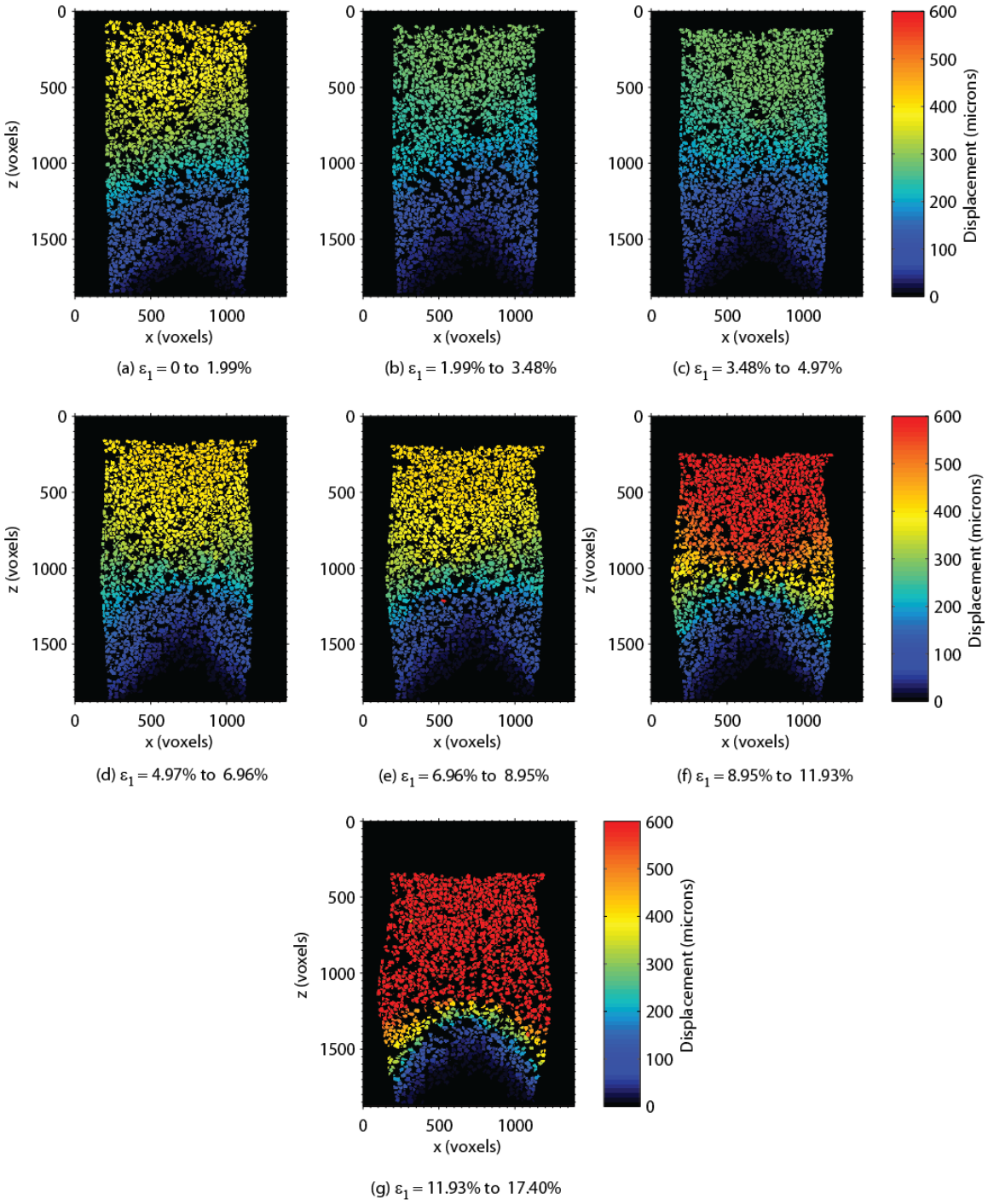

Figure 21. Particle translation for dense #1 dry glass sand specimen (DG-D-15kPa) tested under low confining pressure, $\boldsymbol{\sigma_3}$ = 15 kPa

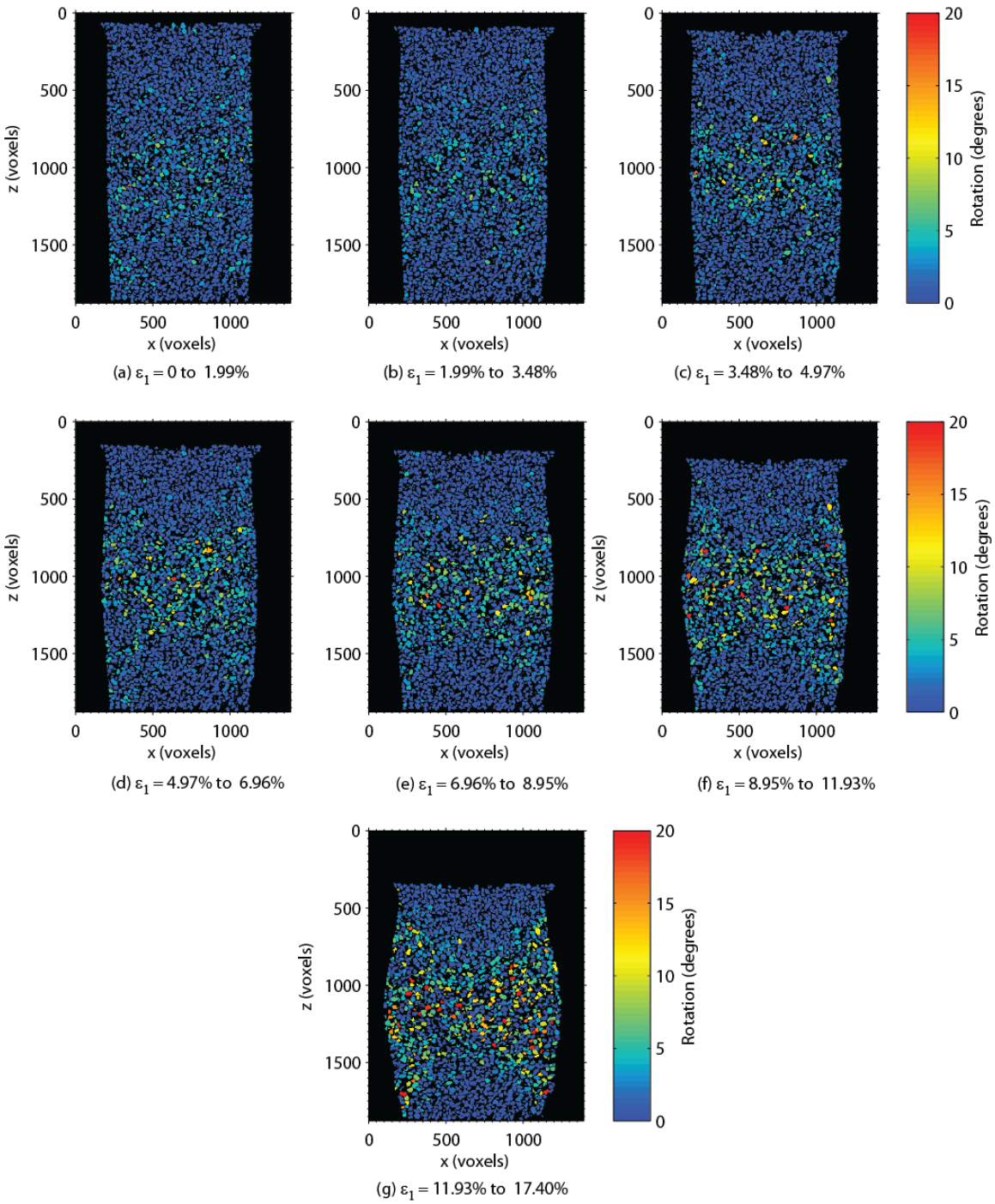

Figure 22. Rotation angle of particles for dense #1 dry glass sand specimen (DG-D-15kPa) tested under low confining pressure, $\boldsymbol{\sigma_3}$ = 15 kPa

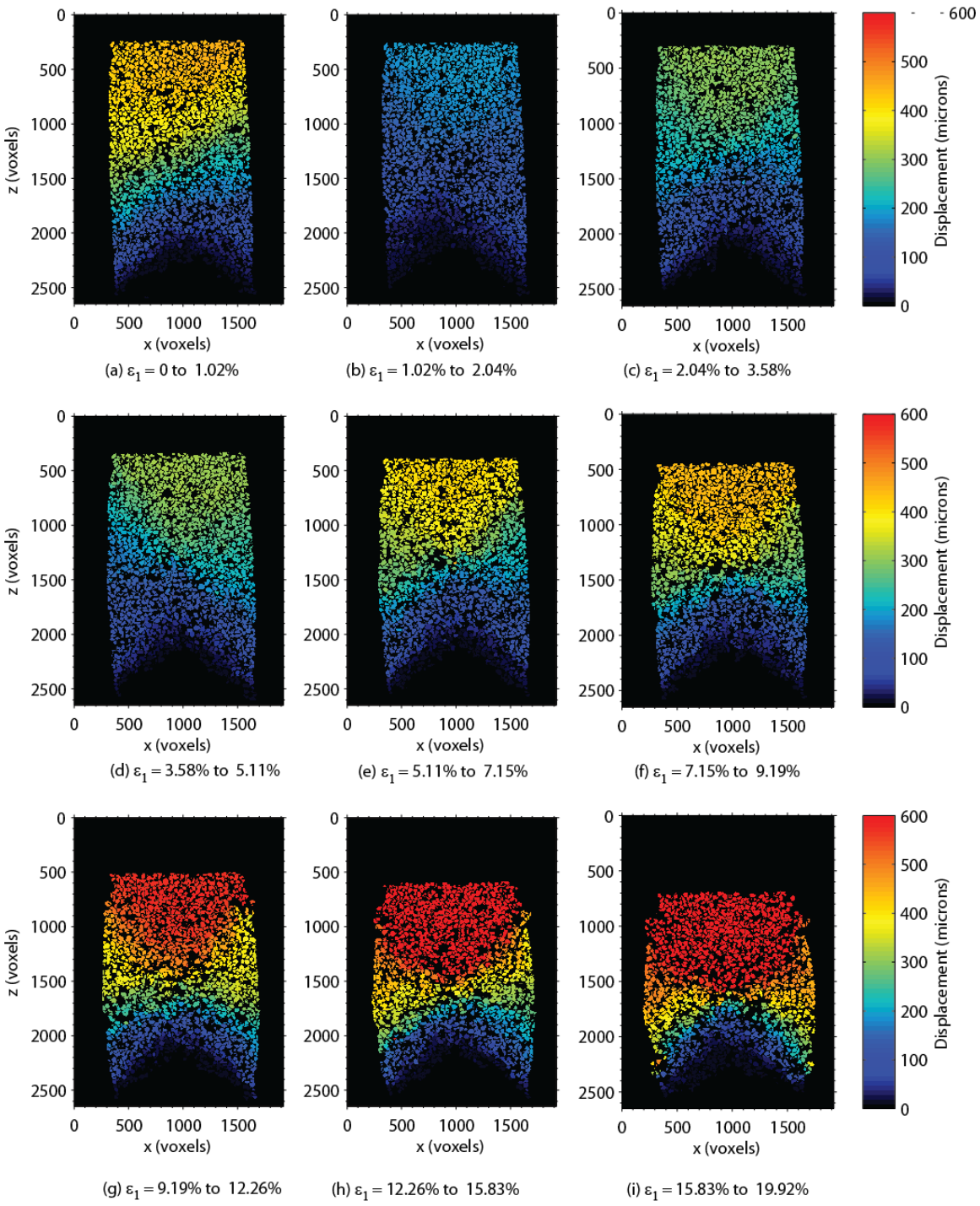

Figure 23. Particle translation for loose #1 dry glass sand specimen (DG-L-15kPa) tested under low confining pressure, $\boldsymbol{\sigma_3}$ = 15 kPa

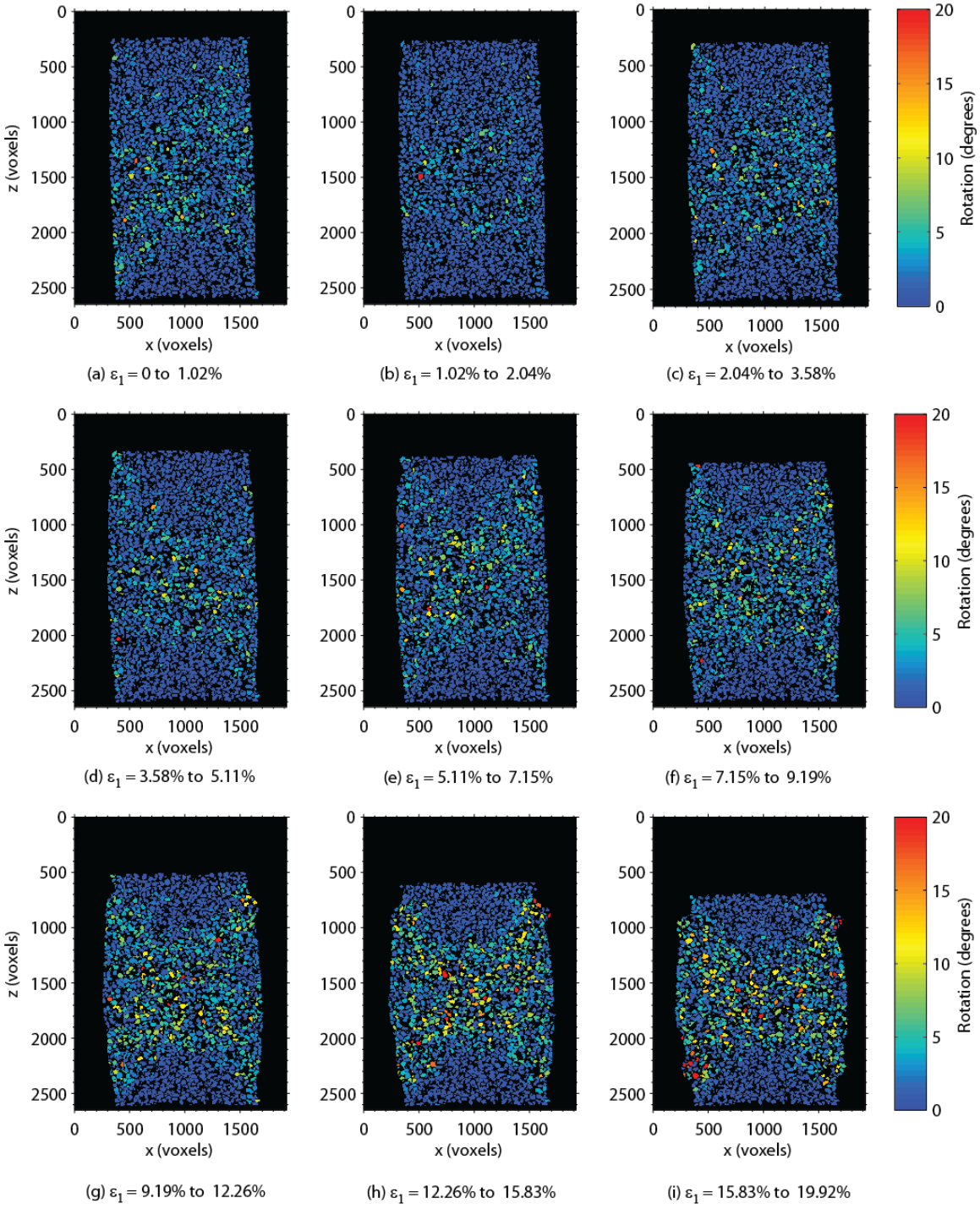

Figure 24. Rotation angle of particles for loose #1 dry glass sand specimen (DG-L-15kPa) tested under low confining pressure, $\boldsymbol{\sigma_3}$ = 15 kPa

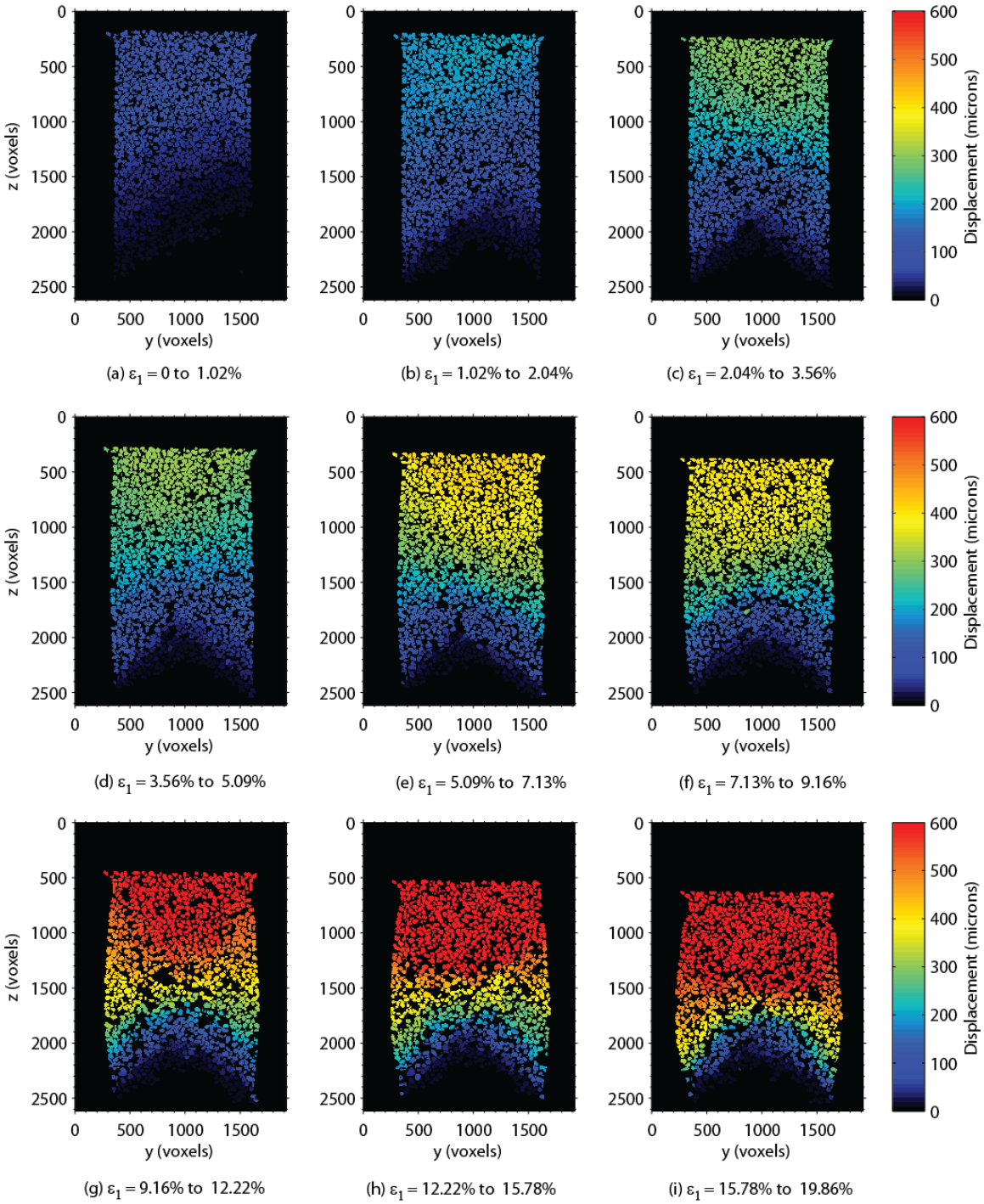

Figure 25. Particle translation for loose F35 sand specimen (F35-L-15kPa) tested under low confining pressure, $\boldsymbol{\sigma_3}$ = 15 kPa

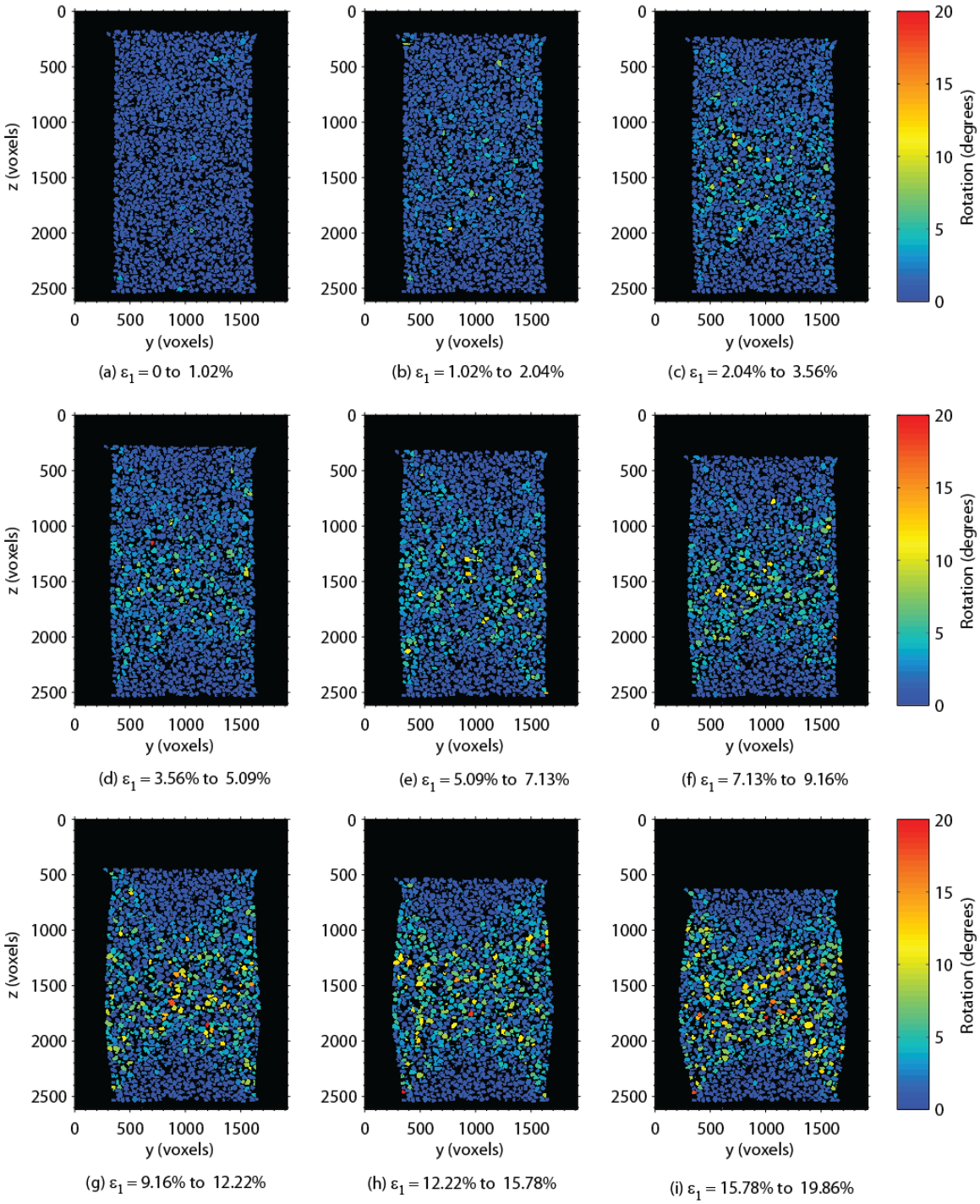

Figure 26. Rotation angle of particles for loose F35 sand specimen (F35-L-15kPa) tested under low confining pressure, $\boldsymbol{\sigma_3}$ = 15 kPa

CHAPTER II
GRANULAR STRAIN MEASUREMENTS FROM PARTICLE LEVEL 3D EXPERIMENTS

Abstract

Constitutive modeling of granular materials has been a subject of extensive research in recent years. While the measurement of the Cauchy stress tensor has been well-established in the literature, the formulation and interpretation of the strain tensor is still not well documented. According to Bagi (1996), researchers mostly adopt well-known continuum or discrete micro-structural approaches to calculate strains within granular materials. However, neither of the two approaches can fully capture the behavior of granular materials, but rather they are considered as complementary to each other where each has its own strength/limitations in solving granular mechanics problems. Zhang and Regueiro (2015) proposed an equivalent continuum approach to measure finite strains at the local level in granular material subjected to large deformations. They used 3D discrete element method data to validate the proposed strains measures. This paper presents an experimental validation of Zhang and Regueiro (2015) approach using 3D images of sheared Ottawa sand specimens. Eulerian finite strains were calculated for representative element volumes within the specimens. The spatial maps of Eulerian octahedral shear strain were able to identify zones of intensive shearing within the specimens, and compared well with maps of incremental particle translation and rotation for the same specimens. The local Eulerian volumetric strain was compared to the global measurements, which also can be considered as an averaging of all local Eulerian volumetric strains. Void ratio evolution curves generally compared well with the volumetric strains at both the local and global levels.

Key Words: finite strain measures, granular assemblies, experimental data, computed tomography

Introduction

Many researchers utilized a broad number of experimental and theoretical studies that focus on deriving the constitutive equations to define the relationship between stresses and strains in granular materials (Bathurst and Rothenburg, 1988; Chang and Ma, 1991; Cundall and Strack, 1979; Mühlhaus, 1986; Pasternak and Mühlhaus, 2002; Tordesillas et al., 2004). According to Bagi (1996), researchers follow two well-known methods to understand the behavior of granular material: the continuum mechanical approach and the microstructural approach. Despite the extensive research, neither of the two approaches can fully capture the true behavior of granular materials, rather they are complementary to each other where each has its own advantages/limitations in solving granular material problems (Oda and Iwashita, 1999).

The continuum mechanical method (Alsaleh et al., 2006; Bauer, 1996; Mühlhaus, 1986; Pasternak and Mühlhaus, 2002; Steinmann, 1995; Techman and Bauer, 1996) considers the granular assembly as a continuum domain where a small volume is used as its representative element and the applied stresses and strains are perceived as the most critical variables in determining the state of the material. The constitutive equations within the framework of the continuum mechanical approach satisfy equilibrium and material laws, and the model parameters are used to represent certain material properties that are usually determined from experiments. Therefore, such approach loses its validity once the conditions are changed in a way that is not similar to the calibration experiments. Bagi (1996) suggested that unless the constitutive equations in the continuum mechanical method are mathematically modified to include extra mechanical parameters or introduce

state variables other than the conventional stress and strain, it will remain as an empirical method and will only be used for practical engineering applications.

Alternatively, the microstructural method is a relatively new approach that relies on micro variables such as contact forces, grain displacements, and local geometrical characteristics to derive the macro-level state variables (Bagi, 1996). Since the microstructural approach utilizes the mentioned discrete characteristics of a granular material at the micro level as an input to determine the state and behavior of the material at the macro level, it renders itself as a more promising method to develop constitutive models that can accurately capture the mechanics of granular materials. Several methods have been proposed in the literature to model the discrete nature of granular material by applying the microstructural approach (Bathurst and Rothenburg, 1988; Chang and Ma, 1991; Cundall and Strack, 1979; Tordesillas et al., 2004). However, there remains a disagreement on the most fundamental questions regarding the formulation of the microstructural strain tensor and eventually the microstructural constitutive equations. Unlike strain tensors' derivations, stress calculations in granular materials; known as the Cauchy stress, has been well established in the literature (Bagi, 1996; Bardet and Vardoulakis, 2001; Christoffersen et al., 1981; Cundall and Strack, 1979; Rothenburg and Selvadurai, 1981).

One of the most challenging concepts that researchers face in the microstructural approach is the geometrical representation of granular assemblies. Chang et al. (1992) defined three length scales that describe different geometrical aspects of the granular assembly. Starting with the smallest scale, the inter-particle contact represents a small area

of contact between two particles, moving to a slightly larger scale; known as the micro element which is composed of one particle and its nearest neighboring particles, and ending with the largest geometrical unit known as the representative unit or the representative element volume (REV). After introducing the basic geometrical units of the granular assembly, there is a need to establish a geometrical system at a larger scale that will be used to model a relatively large mass of grains. Such system should represent the internal properties of the material as well as serve as a link between a discrete material and a continuum (Oda and Iwashita, 1999). Voronoi tessellation, the Dirichlet tessellation, the two dual cell systems of Bagi (1996), and the Delaunay tessellation are examples of well-known geometrical systems. Researchers have developed those tessellations as tools to mainly establish a definition for the micro mechanical strains at the micro element scale and then link it to the deformation at the representative element scale.

According to Bagi (1996), there are few formulations of strain tensors reported in the literature. Most of those measures lie within one of the two approaches: the equivalent continuum (Bagi, 1996; Kruyt and Rothenburg, 1996; Kuhn, 1999; Tordesillas et al., 2010) or the best fit strains (Cambou et al., 2000; Liao et al., 1997; Satake, 2004). The equivalent continuum approach replaces the granular assembly with a continuous domain where the translation of the characteristic points in the domain is equal to the translation of particles' centroids. The best fit strains find the translation gradient tensor based on the smallest deviation from the distinctive displacements of the system. In spite of these advances, most of the reported strain measures are either based on the small strain assumption (Bagi, 1996;

Liao et al., 1997) or are limited to 2D measurements (Cambou et al., 2000; Kruyt and Rothenburg, 1996; Kuhn, 1999; Satake, 2004; Tordesillas et al., 2010).

Zhang and Regueiro (2015) proposed seven finite strain measures in 3D that can be applied to granular materials when they are subjected to large deformations. They adopted the equivalent continuum approach by constructing a continuum domain using Delaunay Tessellation. Zhang and Regueiro (2015) based their calculations of granular strain measures on DEM simulations using the rate of deformation tensor (d) that was originally proposed by Fu and Dafalias (2012). Zhang and Regueiro (2015) furthered this method to include 3D measurements from DEM simulations. They also stated that their granular finite strain measures can be applied not only on DEM simulations but also on the post processing of experimental data of computed tomography (Andò et al., 2011; Druckrey and Alshibli, 2014). There are other methods that can be used to measure finite granular strains (Chupin et al., 2012; O'Sullivan et al., 2003), but they are beyond the scope of this paper since this paper adopts Zhang and Regueiro (2015) method. This paper focuses on calculating the finite strains that were proposed by Zhang and Regueiro (2015) for experimental data on two dense triaxial specimens of F35 Ottawa sand. First, the appropriate REV size was identified by trying different methods. Then, strains were calculated for the specimens at multiple compression stages and were compared to global measurements, the evolution of the void ratio, and particle kinematics.

Materials and Methods

Grain sizes between U.S. sieves #40 (0.420 mm) and #50 (0.297 mm) of F35 Ottawa sand were used in the experiments. F35 Ottawa sand is a sub-rounded to rounded natural silica (quartz) sand, with a specific gravity of 2.65, maximum void ratio of 0.763, minimum void ratio of 0.570, and mean particle size of 0.36 mm. Axisymmetric triaxial compression experiments were conducted on dry F35 Ottawa sand specimens. The triaxial cell is both light in weight and small in size in order to facilitate mounting it directly on the rotation stage where in-situ 3D Synchrotron Micro-Computed Tomography (SMT) images were acquired. It was specially fabricated in order to have the same capabilities as the conventional triaxial cell. The specimens are cylindrical and measure 20 mm in height and 10 mm in diameter to achieve a high image resolution. They were prepared by filling the sand in five layers while gently tamping each layer to achieve a uniform dense packing. The first specimen was tested at a constant confining pressure (σ_3) of 15 kPa (denoted as F35-D-15kPa) which is considered as the low confining pressure whereas the second specimen was tested at relatively high σ_3 of 400 kPa (denoted as F35-D-400kPa, Table 4).

The SMT scans were acquired at beamline 13D of the Advance Photon Source (APS), Argonne National Laboratory (ANL), Illinois, USA. The specimens were scanned using a monochromatic energy of 33 keV and were compressed axially at a constant displacement rate of 0.2 mm/min while maintaining the prescribed constant σ_3. Loading was paused at multiple axial strain (ε_1) stages of the experiments to acquire SMT scans. It took approximately 50 minutes to acquire a full scan. The voxel size for F35-D-15kPa and F35-D-400kPa specimens are 11.14 microns/voxel and 11.18 microns/voxel, respectively

(Table 4). Figure 27 shows the principal stress ratio (PSR=σ_1/σ_3) and the global volumetric strain (ε_v) versus global ε_1 for both experiments. ε_v were calculated from SMT images since air pressure was used to apply σ_3. Referring to Figure 27, F35-D-400kPa specimen exhibited a peak PSR of 4.1 at ε_1 = 5.6% followed by a small degree of softening while the PSR of F35-D-15kPa specimen gradually increased and approached a nearly constant value at a higher ε_1 = 14% when compared to F35-D-400kPa. A higher σ_3 causes failure at smaller ε_1 at a smaller PSR. F35-D-15kPa specimens showed a dilative ε_v from the beginning of the test while F35-D-400kPa shows negligible volume change at early stage of the test followed by dilation until $\varepsilon_1 = 11.81\%$ after which ε_v became nearly constant.

Image Processing and Particle Tracking

Processing of the SMT images was performed using Avizo Fire 8.0 software that uses Visilog algorithm for image processing and quantification. For each loading stage, four overlapping scan heights at a constant step size were acquired in order to capture the total volume of the specimen at the required resolution. The raw greyscale SMT scans were read by the software according to their step size and were stitched together using the merging module, forming a complete one scan volume (Figure 28a). Noise from the greyscale images was removed using an anisotropic diffusion filter which generates a diffusion coefficient in the form of an edge seeking function that preserves the edges between the particles and the voids while removing the noise (Figure 28b). The images were then segmented using a consistent threshold value to separate the solid particles from the surrounding air resulting in a binarized image. Contacting particles were separated using the Avizo *Separate Objects* algorithm, which removes the small area of contact

between particles in contact (Figure 28c). Then, particles were individually labeled with identification numbers (Figure 28d) followed by masking the labels within the binary image to restore the contact area (Figure 28e). A full description of the image processing procedure can be found in Druckrey et al. (2016).

Further quantitative analysis was conducted on the labeled images using a code described in Druckrey et al. (2016). It provides a variety of physical properties of the sheared granular material particles including the coordinates of the center of mass, volume, surface area, and longest, intermediate and shortest axes of particles. Although Avizo labels particles, it does not necessarily give the same label to a specific particle in different scans. Therefore, the code of Druckrey and Alshibli (2014) was used to track particles between two consecutive scans. It isolates a sub-volume around the centroid of each particle in the first image and uses the sub-volume in the second image to search for a matching particle. Individual particle properties within an error of 3% to 4% are compared to the properties obtained from the particle in the first image. If the algorithm does not find a matching particle, it will be eliminated from the analysis. If more than one matching particle are found, the particle with the closest morphological properties is selected.

Finite Strain Calculations

Zhang and Regueiro (2015) proposed granular strain measures using the rate of deformation tensor (d) that was originally proposed by Fu and Dafalias (2012) for 2D DEM simulations. In addition, Fu and Dafalias (2012) used triangular reference frames to calculate the micro element rate of the deformation tensor, where each vertex in the triangle corresponds to a particle centroid and therefore only the velocities of those particles will

be considered while ignoring the contributions of other particles within each triangle. Zhang and Regueiro (2015) extended their strain formulations to 3D by adopting the continuum approach and the Delaunay tessellation of Barber et al. (1996) to divide the granular assembly into many tetrahedrons where each vertex represents a centroid of a particle and the edges are the lines connecting two neighboring particle centroids (Figure 29). If the connected particles were actually in contact with each other, then the edge is denoted as a real contact and if they are not in contact then the edge is treated as a virtual contact (Bagi, 1996). The Delaunay tessellation was then used to represent a whole specimen by a series of continuous REVs in which the nodes of the tetrahedrons have similar kinematics as the particles' centroids. Zhang and Regueiro (2015) formulated the following finite strain measures:

Lagrangian strain: $\bar{E} = \frac{1}{2}\left[\left(\frac{\partial \bar{u}}{\partial X}\right) + \left(\frac{\partial \bar{u}}{\partial X}\right)^T + \left(\frac{\partial \bar{u}}{\partial X}\right)^T \left(\frac{\partial \bar{u}}{\partial X}\right)\right]$ (1)

Eulerian strain: $\bar{e} = \frac{1}{2}\left[\left(\frac{\partial \bar{u}}{\partial x}\right) + \left(\frac{\partial \bar{u}}{\partial x}\right)^T - \left(\frac{\partial \bar{u}}{\partial x}\right)^T \left(\frac{\partial \bar{u}}{\partial x}\right)\right]$ (2)

Henckey strain: $\bar{e}^H = \ln\sqrt{\bar{b}}, \bar{b} = \bar{F}\bar{F}^T$ (3)

Eulerian strain by rate-form: $\bar{e}^{rate}_{n+1} = \bar{e}_n + \left(\bar{d}_{n+1} - \bar{l}^T_{n+1}\bar{e}_n - \bar{e}_n\bar{l}_{n+1}\right)\Delta t$ (4)

Lagrangian strain by rate-form deformation gradient: $\bar{E}_{n+1} = \frac{1}{2}\left(\bar{F}^T_{n+1}\bar{F}_{n+1} - 1\right)$ (5)

Eulerian strain by rate-form deformation gradient: $\bar{E}_{n+1} = \frac{1}{2}\left(1 - \bar{b}^{-1}_{n+1}\right), \bar{b}^{-1}_{n+1} = \bar{F}_{n+1}\bar{F}^T_{n+1}$ (6)

Henckey strain by rate-form deformation gradient: $\bar{e}^{H}_{n+1} = \ln\sqrt{\bar{b}_{n+1}}$ (7)

Where $\frac{\overline{\partial u}}{\partial X}$ is the spatial derivative of the current particle centroid displacement with respect to the reference position. $\frac{\overline{\partial u}}{\partial x}$ is calculated with reference to the current position. $\overline{F}$ is the average deformation gradient tensor that can be calculated from the average Eulerian displacement gradient tensor: $\overline{F} = \left(1 - \frac{\overline{\partial u}}{\partial x}\right)^{-1}$. The granular spatial velocity gradient is denoted as $\bar{l} = \frac{\overline{\partial v}}{\partial x}$, $\overline{d}$ is the deformation rate tensor that represents the symmetric part of the velocity gradient: $\overline{d} = sym(\bar{l})$.

Furthermore, Zhang and Regueiro (2015) conducted two tests to check the validity of the strain formulations: comparison with the macro-wall-strain (i.e.: the strain calculated from the boundary displacements) and a large rotation test. The tests were conducted on a DEM simulation of a 5 mm × 5 mm × 4 mm assembly of F-75 Quartz Ottawa sand grains undergoing triaxial compression. In summary, Zhang and Regueiro (2015) reported that the rate-form strains (Equations 4-7) are the best strain measures, and the Eulerian strain by rate-form is the same as the Eulerian strain by rate-form deformation gradient. Furthermore, the Lagrangian and the Eulerian strain formulations gave the best results for calculating strains for DEM simulations of triaxial compression tests. For a more detailed description of the formulations of the strain measures and the aforementioned tests, the reader is referred to Zhang and Regueiro (2015). In this paper, the volume-averaging

domain was taken as the REV size and the computer code of Zhang and Regueiro (2015) was applied on the 3D experimental triaxial data for the centroids of the tracked particles at multiple global strain increments. Both Lagrangian and Eulerian strains were calculated for the data and they gave similar results. Therefore, only Eulerian octahedral shear, and volumetric strain results are reported in this paper.

Volumetric and Octahedral Shear Strains

To calculate the finite strains, a REV needs to be identified for the F35 sand specimens. Although the REV concept was initially developed for providing an average of properties of a homogenous medium where the classical continuum hypothesis holds, it was extended to the microstructural equivalent continuum approach to calculate the strain tensor of a granular assembly. The equivalent continuum approach requires a continuous domain that represents the granular assembly where the translation of the characteristic points in the domain is equal to the translation of particles' centroids. REV is defined as the smallest constituent or sub-volume to represent a physical property of a 3D SMT image (e.g., void ratio). In a qualitative assessment of the REV, Bear (1972) and Dullien (1992) suggested that the size of the REV should be large enough to smooth out granular fluctuations and at the same time, it should be relatively small such that macroscopic changes will not affect the results. Cubical sub volumes were extracted from 3D CT images and were used to calculate multiple properties such as porosity, saturation, and the interfacial area of glass beads (Al-Raoush and Willson, 2005; Culligan et al., 2004) and Ooid sand (Al-Raoush and Willson, 2005). Numerical simulations of particle assemblies

were also utilized to find adequate REV size for relevant properties (Ostoja-Starzewski, 2005; Stroeven et al., 2004).

REV size identification was conducted using two methods. The first method utilized Avizo 8.0 software. The final labeled image was loaded into the software, a cube with a known size was extracted from the middle of the specimen, and the *label analysis* module was used to calculate the volume for particles within the assigned cube. The void ratio (volume of voids divided by volume of solids) was then calculated for the cubic sub-volume. The cube size was increased in the following loading increments while maintaining its position within the specimen and the void ratio was calculated again. Figure 30 shows the calculated void ratio versus the side length of the cube for the two specimens. A REV size of 1500 micron was selected as the smallest cube size that yields a constant void ratio value.

The second REV size identification method used the code of Zhang and Regueiro (2015) to calculate Eulerian volumetric strain ($\bar{E}_v$) and octahedral shear strain ($\bar{\gamma}_{oct}$) for different cubical sub-volume sizes. $\bar{E}_v$ and $\bar{\gamma}_{oct}$ are defined as:

$$\overline{E}_v = \overline{E}_{11} + \overline{E}_{22} + \overline{E}_{33} \tag{8}$$

$$\overline{\gamma}_{oct}^2 = \frac{1}{9}\left[\left(\overline{E}_{11} - \overline{E}_{22}\right)^2 + \left(\overline{E}_{11} - \overline{E}_{33}\right)^2 + \left(\overline{E}_{22} - \overline{E}_{33}\right)^2\right] + \frac{2}{3}\left(\overline{E}_{12}^2 + \overline{E}_{13}^2 + \overline{E}_{23}^2\right) \tag{9}$$

$\bar{E}_{11}$, $\bar{E}_{22}$, and $\bar{E}_{33}$ are the normal Eulerian strains by rate-form deformation gradient in the x, y, and z directions, respectively. The z direction represents the direction of loading (major principal stress direction) for the triaxial specimens. Figure 31 through Figure 33

show the calculated $\bar{E}_v$ and $\bar{\gamma}_{oct}$ versus ε_1 for different REV sizes at three different locations within the F35-D-400kPa specimen. To eliminate the effect of the membrane on the finite strain calculations, all REVs were centered within the x-y plane while their position was changed in the z-direction. A negative $\bar{E}_v$ represents specimen dilation. Referring to Figure 31, the REVs are located in the middle of the specimen, where intensive shearing took place. All REV sizes for $\bar{E}_v$ exhibit a similar behavior until $\varepsilon_1 = 4.91\%$. The 1500 micron REV shows a different trend when compared to the other REV sizes where higher predictions of decreasing volumetric strains are observed during the last two ε_1 increments. In addition, $\bar{E}_v$ of the 1500 micron REV shows a trend change into contraction after $\varepsilon_1 = 4.91\%$ and exhibits unrealistic extreme values after $\varepsilon_1 = 8.85\%$. On the other hand, the 3000 micron REV begins to show a small deviation from the other REVs at $\varepsilon_1 = 4.91\%$ and evolves into a higher deviation at $\varepsilon_1 = 8.85\%$ where $\bar{E}_v$ decreases to a positive value at the last two increments with a final value of $\bar{E}_v$ = 10%. The remaining REVs agree well with each other with a small variation at the last increment, at which the $\bar{E}_v$ begins to decrease and fluctuate between -4.0% and 4.0%. All REV sizes for $\bar{\gamma}_{oct}$ exhibit similar trends until $\varepsilon_1 = 4.91\%$ (Figure 31) followed by high values. The 1500 micron REV has the highest value of approximately 35% and the 9000 micron REV has the lowest value of about 16%.

Figure 32 shows the $\bar{E}_v$ and $\bar{\gamma}_{oct}$ versus ε_1 relationships for different REV sizes at the top portion of the specimen. The top edge of each REV was chosen at a distance of 720 micron ($2d_{50}$) from the interface with the loading end plate. All REV sizes for $\bar{E}_v$ follow the same trend with almost equal values (within an error of ±1.2%) except for the 1500

micron REV which has a similar trend with significantly higher strain values. The 1500 and 3000 micron REVs exhibit slightly different behavior for $\bar{\gamma}_{oct}$ versus ε_1 in comparison with the remaining REVs. The 1500 and 3000 micron REVs also show a tendency to reach a plateau in $\bar{\gamma}_{oct}$ at the last two ε_1 increments whereas other REVs exhibit a continuous increase in $\bar{\gamma}_{oct}$. The REVs located near the bottom of the specimen, where the bottom edge of each REV was at a distance of 720 micron ($2d_{50}$) from the interface with the bottom plate (Figure 33), have similar $\bar{E}_v$ values and trends. The exception is the 1500 micron REV, which exhibits higher $\bar{E}_v$ values at the last two ε_1 increments. Furthermore, at the last ε_1 increment, the $\bar{E}_v$ for the 1500 micron REV keeps on increasing while it decreases for the rest of the REVs. All REV sizes for $\bar{\gamma}_{oct}$ versus ε_1 show the same trend with almost equal values except for the 3000 micron REV, which shows a completely different behavior. It is interesting to note that the 1500 micron REV has similar $\bar{\gamma}_{oct}$ values as the REVs within the size range of 4500 to 9000 micron, but then again the behavior changes for the 3000 micron REV.

In summary, a REV size of 1500 micron is not large enough to yield acceptable values of the finite strains within extensive shearing zones and a higher REV size is required. In other words, although the 1500 micron REV was enough to achieve constant void ratio values, a larger number of particles are needed to achieve logical values of finite strains. The strain values for the 1500 micron REV are not logical (overestimated or slightly underestimated in some cases). To further investigate this finding, color maps of the calculated $\bar{\gamma}_{oct}$ values for an axial section that was extracted from the middle of the 3D scans and divided into 1500 micron cubes were analyzed. These maps strongly predict the

failure modes for both the F35-D-400kPa and the F35-D-15kPa specimens. The F35-D-400kPa specimen failed through a single shear band as can be easily identified in the color maps of the $\bar{\gamma}_{oct}$ (Figure 34) which also compares well with the particle rotations (Figure 35) and displacement fields (Figure 36) for the same specimen. The F35-D-15kPa specimen did not fail through a single well-defined shear band but rather through bulging in the middle of the specimen with intensive shearing and $\bar{\gamma}_{oct}$ spatial distribution reflects such behavior (Figure 37 through Figure 39). The analysis of the color maps suggests that the code can be used as a tool to initially investigate and detect the failure modes of the tested specimen for smaller REV sizes with the tradeoff of not achieving accurate values of the calculated finite strains.

If we exclude the last ε_1 increment, REV sizes between 4500 micron and 9000 micron exhibit similar behavior and values of $\bar{E}_v$ and $\bar{\gamma}_{oct}$ near the top and bottom parts of the specimen as well as $\bar{E}_v$ for the REVs in the middle of the specimen. Although $\bar{\gamma}_{oct}$ for the REVs in the middle of the specimen show the same behavior, higher values and variations are observed in the last two ε_1 increments as the REV size increases from 4500 micron to 9000 micron. Referring to Figure 31, the difference between $\bar{\gamma}_{oct}$ values from REV sizes of 4500 micron to 9000 micron at $\varepsilon_1 = 8.85\%$ is almost 6.0% and it increases at the last step ($\varepsilon_1 = 11.79\%$) to 8%.

In some cases a decrease in $\bar{E}_v$ is noticed in the last two ε_1 increments especially in zones where intensive shearing and high strain localization occur (Figure 31), indicating that the particles in the tested REV began to undergo compression, which is not in agreement with the global behavior (ε_v) of the specimen. To further investigate such

unexpected behavior, several REVs of a size of 5000 micron were selected at different locations within both specimens. Two REVs (1B and 2B) were selected within the shear band, and REV 3 and REV 4 were chosen near the bottom and top of the F35-D-400kPa specimen, respectively (Figure 40). There are small overlaps between the REVs due to the small size of the specimen in comparison to the size of the REV required to achieve logical values of finite strains. Overall, such overlaps do not have a significant effect on the results. Figure 41 shows $\bar{E}_v$ versus ε_1 of the REVs superimposed on ε_v for the F35-D-400kPa specimen. REVs located within the shear band exhibit the highest $\bar{E}_v$, and their values are close to ε_v. However, $\bar{E}_v$ of REV 1B exhibits a sudden decrease at the last ε_1 increment. This is also obvious in $\bar{E}_v$ of REV 2B, where it begins to decrease slightly at $\varepsilon_1 = 8.85\%$ followed by a higher drop at the last ε_1 increment. On the other hand, the ε_v keeps increasing at ε_1 = 11.81% and finally reaches a plateau at ε_1 = 17.20%. REVs 3 and 4 show a dilative behavior and begin to approach a plateau at the last two ε_1 increments, which is in agreement with the global ε_v behavior of the specimen.

Figure 42 shows the location of the REVs that were analyzed for the F35-D-15kPa specimen where three 5000 micron REV were selected near the bottom, middle, and top of the specimen. The results of the analysis are depicted in Figure 43 where REV 2 exhibits $\bar{E}_v$ values slightly higher than the ε_v until ε_1 = 4.96% when $\bar{E}_v$ begins to decrease to 2.66% contraction. REV 2 is located in the middle of the specimen where extensive shearing took place. REVs 1 and 3 show dilative behavior throughout the different scans; however, their rate of increase is smaller than ε_v. With exception of the last ε_1 increment for REVs that are within zones of extensive shearing, the global ε_v can be perceived as an approximate

average of all local $\bar{E}_v$ values. While only 3 or 4 REVs per specimen were analyzed in the paper, the global ε_v is situated between the upper range REVs where high strain localization occurs (REV 1B and REV 2B in Figure 41 and REV 2 in Figure 43) and the lower range REVs that are located outside zones of intensive shearing (REV 3 and REV 4 in Figure 41 and REV 1 and REV 2 in Figure 43).

To check if the decrease in the volumetric strains is attributed to material response or error in computer code calculations, the evolution of the void ratio (e) was calculated for all REVs as well as the whole specimens (labeled as global e values) based on SMT images which are depicted in Figure 44 and Figure 45 for the F35-D-400kPa and F35-D-15kPa specimens, respectively. An image processing technique was used to calculate the void ratio for each individual REV by dividing the voxels of voids by the voxels of particles. The accuracy of e calculations is very high and can be used as a validation for volumetric strains calculations. The global e evolution versus ε_1 for the F35-D-400kPa specimen has an initial value of 0.586 that decreases to 0.577 in the second ε_1 increment followed by a linear increase to a value of 0.687 at ε_1 = 8.85% when e remains constant during the last ε_1 increment. The global e-value for the F35-D-15kPa specimen starts at an initial value of 0.603 and displays a continuous increase to 0.668 with a slower rate when compared to the F35-D-400kPa specimen (Figure 45). The general trend of e evolution for the REVs within both specimens is the same as the global e-values with a few exceptions. REVs 1B and 2B represent the zones of intensive shearing; therefore, they manifested the highest rate of e increase (Figure 44). The rate of e increase declines slightly during the last two ε_1 increments. REVs 3 and 4 in Figure 44 show smaller rates of increase and reach

nearly constant e values of 0.589 and 0.547, respectively. Referring to Figure 45, REV 2 shows the highest e-rate increase where e reaches a value of 0.717 at ε_1 = 11.81%, which is higher than the global e-value for the F35-D-15kPa specimen. REVs 1 and 3 show similar behavior as the global e-value; however they have smaller e-values and REV 1 (located near the bottom of the specimen) displays a slight decrease in e at the last ε_1 increment. The small difference between each REV and the global behavior is due to the particulate nature of sand, which causes the observed heterogeneous behavior. Furthermore, the location of the REV within the specimen is very critical. A REV within a shear localization zone and a REV outside a shear localization zone are expected to yield different values of the calculated e or finite strains. However, the observation can be extended to include REVs selected close to each other within the same zone, where one may include a cluster of particles that exhibit extreme dilative or contractive behavior which will have a major influence on the calculations while they are absent from the other REV. The confining pressure affects the evolution of e where high confining pressure inhibits dilation and none of the selected REVs had an e-value higher than the global e (Figure 44), whereas specimen will dilate and shear zones will have e-values higher than the global e-value when it is tested under low confining pressure (Figure 45).

One can observe that the e evolution and the volumetric strain trends fully agree with each other. This is also the case for the REVs located outside zones of intensive shearing. On the other hand, REVs located within zones of intensive shearing show an increase in e, meaning that said REVs are showing dilative behavior. However, $\bar{E}_v$ for those REVs show compressive behavior at the last ε_1 increment (REVs 1B and 2B in Figure 41) and

sometimes much earlier than that ε_1 level (REV 2 in Figure 43). The code does not yield accurate $\bar{E}_v$ for high strains because the SMT scans were acquired at larger strain increments in the last two SMT scans (see Table 4). REV positions were fixed in all strain stages whereas the sand grains within a particular REV will change. As the loading proceeds, some grains will move out of the REV and new sand grains will replace them. The Eulerian strain calculations are based on these changed sand grains and since high shear strains occurred between ε_1 = 8% to 12% scans, smaller strain increments are needed to yield accurate strain values. Nonetheless, the code produced accurate strain calculations when the SMT scans were acquired at 2% axial strain increments.

Conclusions

The experimental kinematic measurements of sand grains within two dense F35 sand specimens that were tested under axisymmetric triaxial loading at confining pressures of 15 kPa and 400 kPa were used to quantify the local Eulerian finite strains using the method proposed by Zhang and Regueiro (2015). The following conclusions are drawn from the results reported in this paper:

1. This paper presented for the first time experimental validation to calculate the local finite strains based on 3D particle translation.
2. A REV size of 1500 micron (4.17 d_{50}) is sufficient to yield an accurate average e and color maps of the calculated $\bar{\gamma}_{oct}$ that compared well with particle kinematics measurements. However, the values of the calculated $\bar{E}_v$ and $\bar{\gamma}_{oct}$ corresponding to this

REV size over-predicted and in rare instances under-predicted the values especially at the last two ε_1 increments.

3. A minimum REV size of 4500 micron (12.51 d_{50}) is required to give better predictions of $\bar{E}_v$ and $\bar{\gamma}_{oct}$. Nevertheless, even with larger REV sizes, REVs located within the zones of intensive shearing still gave illogical values at the last two ε_1 increments due to larger interval between the SMT scans.
4. Larger REV sizes as well as smaller strain increments between the scans are needed in order to improve the accuracy of the code in quantifying finite strains based on particle kinematic behavior.
5. The specimen tested under high confining pressure (F35-D-400kPa) failed through a single well-defined shear band. The $\bar{E}_v$ for the local REVs exhibit a small compression at the first ε_1 increment followed by a dilation that reaches a plateau at the final ε_1 increments.
6. The specimen tested under low confining pressure (F35-D-15kPa) failed through bulging where intensive shearing occurred in the middle part of the specimen. Unlike the F35-D-400kPa specimen, the $\bar{E}_v$ exhibit no compression but rather it dilates at a slower rate than that of the F35-D-400kPa and continues dilating throughout the test.
7. Void ratio evolution curves were constructed for 5000 micron REVs positioned at different locations within the two specimens and were compared with the $\overline{E}_v$. In general, the measurements compared well except for the last two ε_1 increments for REVs located within zones of intensive shearing. All REVs in the specimen show dilative behavior, especially in zones of intensive shearing (i.e, within the shear band

for the F35-D-400kPa specimen and within the middle of the F35-D-15kPa specimen that failed via a diffuse bulging failure).

8. The local e-value and its evolution for the F35-D-400kPa specimen never exceeded the global e evolution due to the high confining pressure. On the other hand, REVs located in the intensive shearing zone within the F35-D-15kPa specimen exhibited high e-values when compared with the global e.
9. The advancements in imaging techniques and processing will make it possible to apply the codes developed by Zhang and Regueiro (2015) on experimental data in order to calculate accurate 3D measurements strains at the local particle level that can potentially help in developing micromechanic constitutive models for granular materials.

References

Al-Raoush, R.I., Willson, C.S., (2005). "Extraction of physically realistic pore network properties from three-dimensional synchrotron X-ray microtomography images of unconsolidated porous media systems". *Journal of Hydrology*, 300, 44-64.

Alsaleh, M. I., G. Z. Voyiadjis and K. A. Alshibli (2006). "Modelling strain localization in granular materials using micropolar theory: mathematical formulations." *International Journal for Numerical and Analytical Methods in Geomechanics* 30(15): 1501-1524.

Andò, E., Hall, S.A., Viggiani, G., Desrues, J., Bésuelle, P. (2011). "Grain-scale experimental investigation of localised deformation in sand: a discrete particle tracking approach." *Acta Geotechnica*, 7, 1-13.

Bagi, K. (1996). "Stress and strain in granular assemblies." *Mechanics of Materials*, 22, 165-177.

Bagi, K. (2006). "Analysis of microstructural strain tensors for granular assemblies." *International Journal of Solids and Structures* 43, 3166-3184.

Barber, C.B., Dobkin, D.P., Huhdanpaa, H. (1996). "The quickhull algorithm for convex hulls." *ACM Trans. Math. Softw*. 22, 469-483.

Bardet, J.P., Vardoulakis, I. (2001). "The asymmetry of stress in granular media." *International Journal of Solids and Structures* 38, 353-367.

Bathurst, R.J., Rothenburg, L. (1988). "Micromechanical Aspects of Isotropic Granular Assemblies With Linear Contact Interactions." *Journal of Applied Mechanics* 55, 17-23.

Bauer, E. (1996). "Calibration of a comprehensive hypoplastic model for granular materials." *Soils and Foundations* 36(1): 13-26.

Bear, J. (1972). "Dynamics of Fluids in Porous Media." Dover.

Cambou, B., Chaze, M., Dedecker, F. (2000). "Change of scale in granular materials." *European Journal of Mechanics - A/Solids* 19, 999-1014.

Chang, C., Chang, Y., Kabir, M. (1992). "Micromechanics Modeling for Stress-Strain Behavior of Granular Soils. I: Theory." *Journal of Geotechnical Engineering* 118, 1959-1974.

Chang, C.S., Ma, L. (1991). "A micromechanical-based micropolar theory for deformation of granular solids." *International Journal of Solids and Structures* 28, 67-86.

Christoffersen, J., Mehrabadi, M.M., Nemat-Nasser, S. (1981). "A Micromechanical Description of Granular Material Behavior." *Journal of Applied Mechanics* 48, 339-344.

Chupin, O., Rechenmacher, A.L., Abedi, S. (2012). "Finite strain analysis of nonuniform deformation inside shear bands in sands." *International Journal for Numerical and Analytical Methods in Geomechanics* 36, 1651-1666.

Culligan, K.A., Wildenschild, D., Christensen, B.S.B., Gray, W.G., Rivers, M.L., Tompson, A.F.B. (2004). "Interfacial area measurements for unsaturated flow through a porous medium." *Water Resources Research* 40.

Cundall, P.A., Strack, O.D.L. (1979). "A discrete numerical model for granular assemblies." *Géotechnique* 29, 47-65.

Druckrey, A., Alshibli, K. (2014). "3D Behavior of Sand Particles Using X-Ray Synchrotron Micro-Tomography." *Geo-Congress 2014 Technical Papers*. American Society of Civil Engineers, pp. 2814-2821.

Druckrey, A.M., Alshibli, K.A., Al-Raoush, R.I. (2016). "3D characterization of sand particle-to-particle contact and morphology." *Computers and Geotechnics* 74, 26-35.

Dullien, F.A.L. (1992). "Porous Media: Fluid Transport and Pore Structure." Academic Press.

Fu, P., Dafalias, Y.F. (2012). "Quantification of large and localized deformation in granular materials." *International Journal of Solids and Structures* 49, 1741-1752.

Hasan, A., Alshibli, K.A. (2010). “Experimental assessment of 3D particle-to-particle interaction within sheared sand using synchrotron microtomography.” *Géotechnique* 60, 369-379.

Iwashita, K., Oda, M. (1999). “Mechanics of Granular Materials: An Introduction.” Taylor & Francis.

J., Techman and E. Bauer (1996). "Numerical Simulation of Shear Band Formation with a Polar Hypoplastic Constitutive Model." *Computers and Geotechnics* 19(3): 221-244.

Kruyt, N.P., Rothenburg, L. (1996). “Micromechanical Definition of the Strain Tensor for Granular Materials.” *Journal of Applied Mechanics* 63, 706-711.

Kuhn, M.R. (1999). “Structured deformation in granular materials.” *Mechanics of Materials* 31, 407-429.

Liao, C.-L., Chang, T.-P., Young, D.-H., Chang, C.S. (1997). “Stress-strain relationship for granular materials based on the hypothesis of best fit.” *International Journal of Solids and Structures* 34, 4087-4100.

Mühlhaus, H. B. (1986). "Shear band analysis in granular materials by Cosserat theory." *Ing. Arch.* 56: 389-399.

Ostoja-Starzewski (2005). “On the admissibility of an isotropic, smooth elastic continuum.” *Archives of Mechanics* 57, 345-355.

O'Sullivan, C., D. Bray, J., Li, S. (2003). “A new approach for calculating strain for particulate media.” *International Journal for Numerical and Analytical Methods in Geomechanics* 27, 859-877.

Pasternak, E. and H. B. Mühlhaus (2002). “Large deformation Cosserat continuum modeling of granular materials.” Applied Mechanics. Progress and application. In ACAM 2002 The Third Australasian Congress on Applied Sydney, Australia, World Scientific Publishing Co. Pte. Ltd. .

Rothenburg, L., Selvadurai, A.P.S. (1981). “A micromechanical definition of the Cauchy stress tensor for particulate media.” in: Selvadurai (Ed.), *Int. Symp. on the Mechanical Behavior of Structured Media*, Ottawa, pp. 469-486.

Satake, M. (2004). “Tensorial form definitions of discrete-mechanical quantities for granular assemblies.” *International Journal of Solids and Structures* 41, 5775-5791.

Steinmann, P. (1995). "Theory and numerics of ductile micropolar elastoplastic damage." *International Journal for Numerical Methods in Engineering* 38(4): 583-606.

Stroeven, M., Askes, H., Sluys, L.J. (2004). “Numerical determination of representative volumes for granular materials.” *Computer Methods in Applied Mechanics and Engineering* 193, 3221-3238.

Tordesillas, A., Peters, J.F., Gardiner, B.S. (2004). “Shear band evolution and accumulated microstructural development in Cosserat media.” *International Journal for Numerical and Analytical Methods in Geomechanics* 28, 981-1010.

Tordesillas, A., Walsh, S.D.C., Muthuswamy, M. (2010). “The effect of local kinematics on the local and global deformations of granular systems.” *Mathematics and Mechanics of Solids* 15, 3-41.

Zhang, B., Regueiro, R.A. (2015). “On large deformation granular strain measures for generating stress–strain relations based upon three-dimensional discrete element simulations.” *International Journal of Solids and Structures* 66, 151-170.

Appendix

Table 4. Properties of the tested F-35 Ottawa sand specimens

Exp.	Initial void ratio	σ_3 (kPa)	Relative density (%)	Specimen height (mm)	Initial specimen diameter (mm)	Scan acquired at axial compression, ε_1 (%)	Resolution, (μm/voxel)
F35-D-15kPa	0.603	15	83	20.16	10.77	0.0, 0.99, 1.98, 3.47, 4.96, 6.94, 8.93, 11.90	11.14
F35-D-400kPa	0.586	400	91	20.35	10.41	0.0, 0.98, 1.97, 3.44, 4.91, 6.88, 8.85, 11.79	11.18

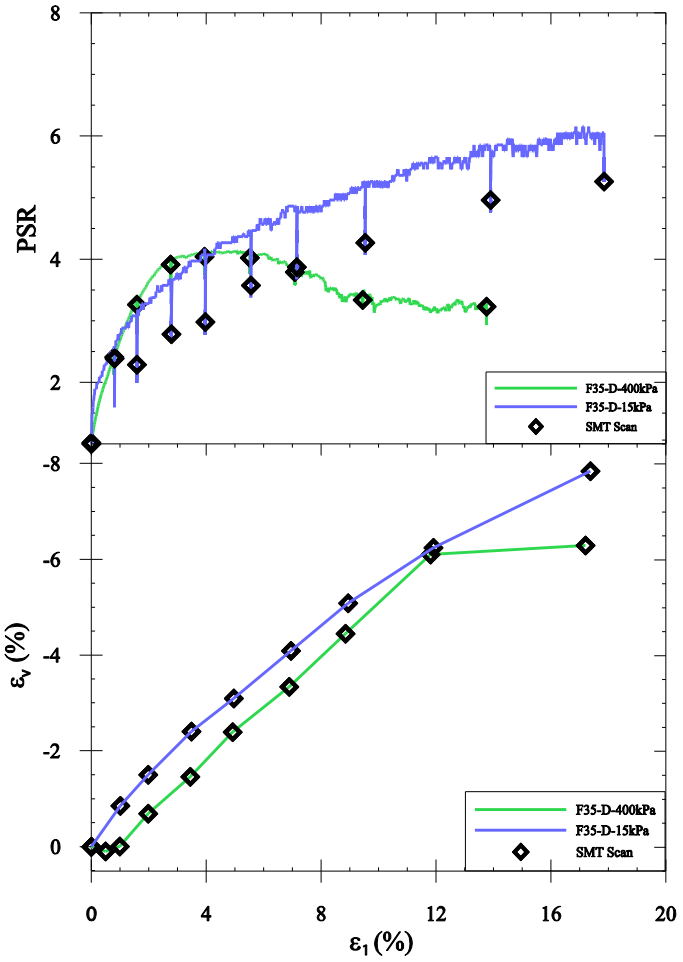

Figure 27. Principal stress ratio (PSR) and global volumetric strain versus nominal axial strain for the F35-D-400kPa and F35-D-15kPa specimen.

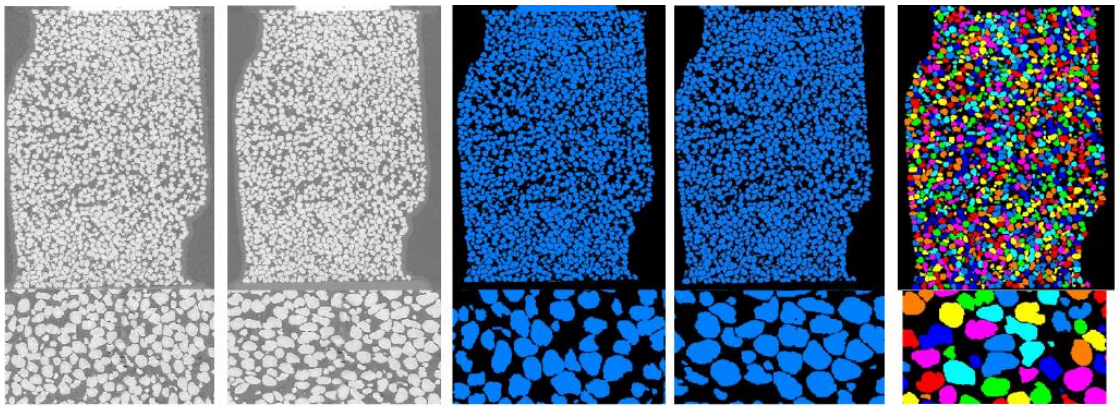

Figure 28. Image processing steps to produce labeled particles.

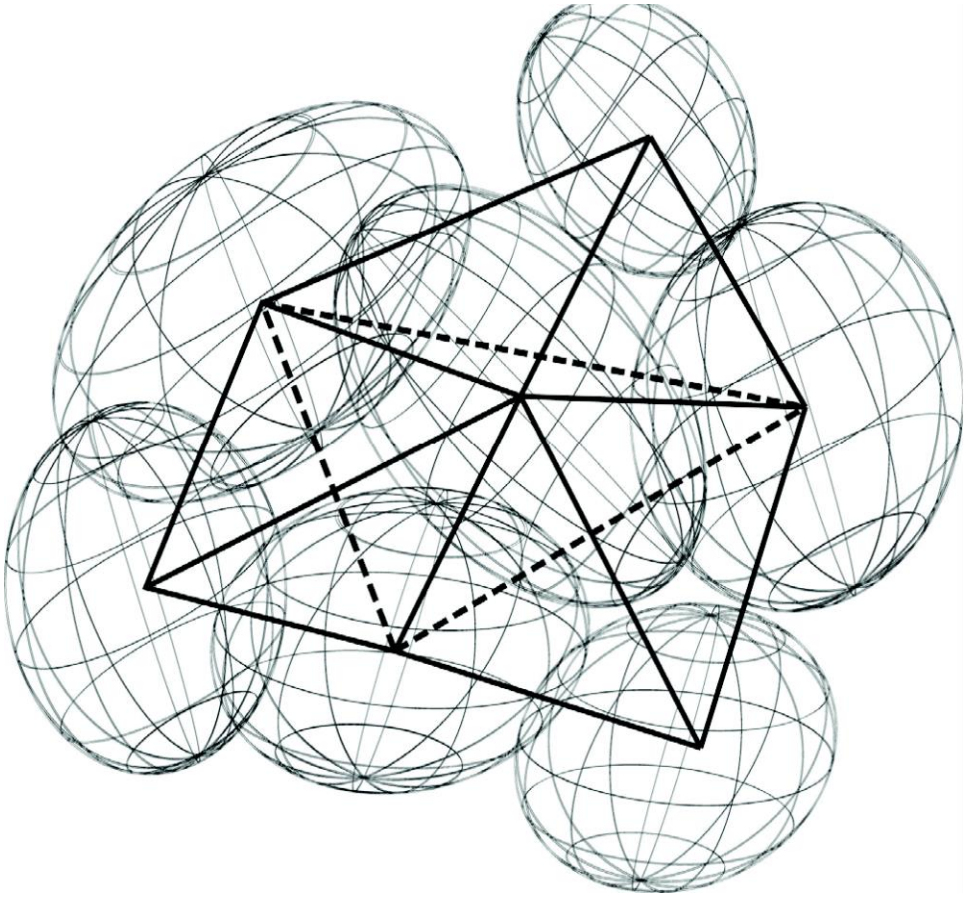

Figure 29. Illustration of Delaunay tessellation for seven ellipsoidal particles showing four tetrahedrons (Zhang and Regueiro; 2015).

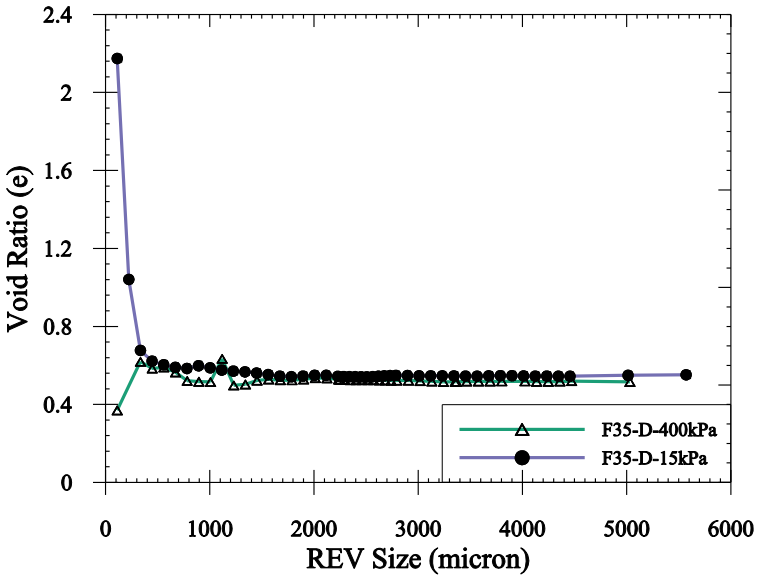

Figure 30. Void ratios versus REV size the F35-D-400kPa and the F35-D-15kPa specimens. Based on the analysis, a REV size of 1500 microns was chosen as the smallest size to yield a constant void ratio.

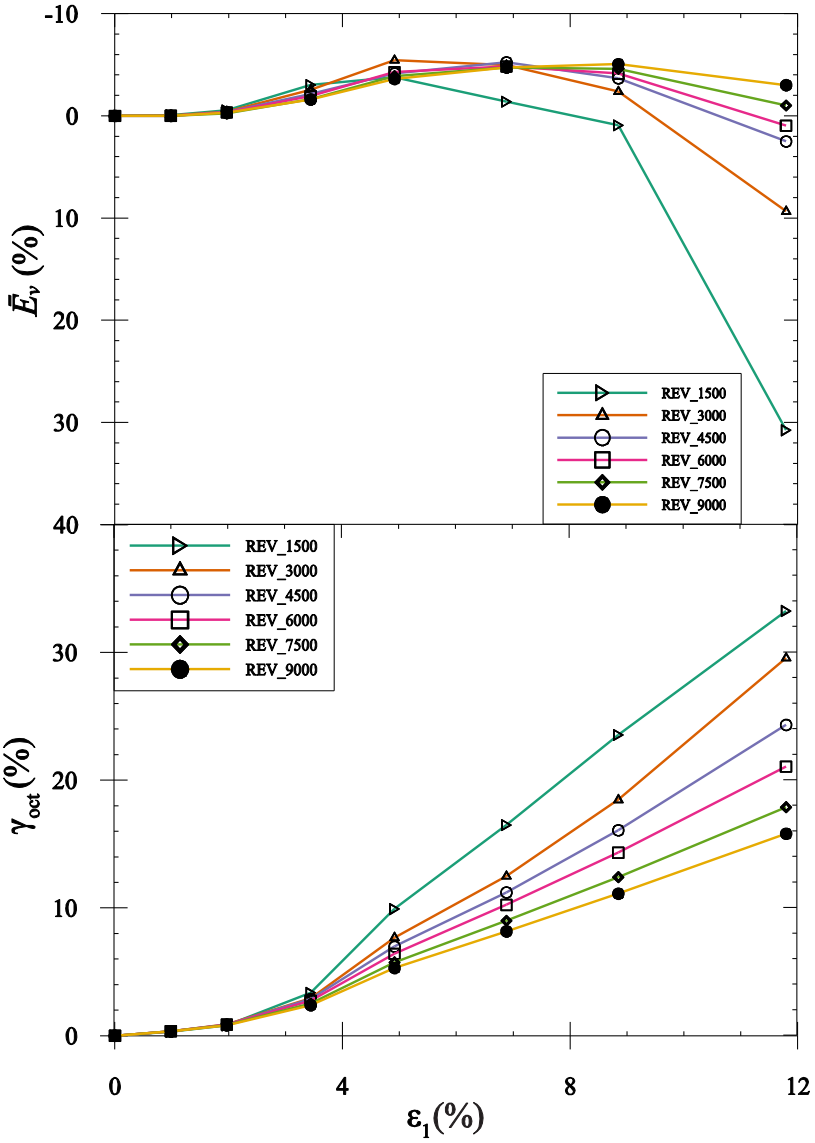

Figure 31. Eulerian volumetric and octahedral shear strains versus the global nominal axial strain for different REV sizes taken at the middle of the F35-D-400kPa specimen.

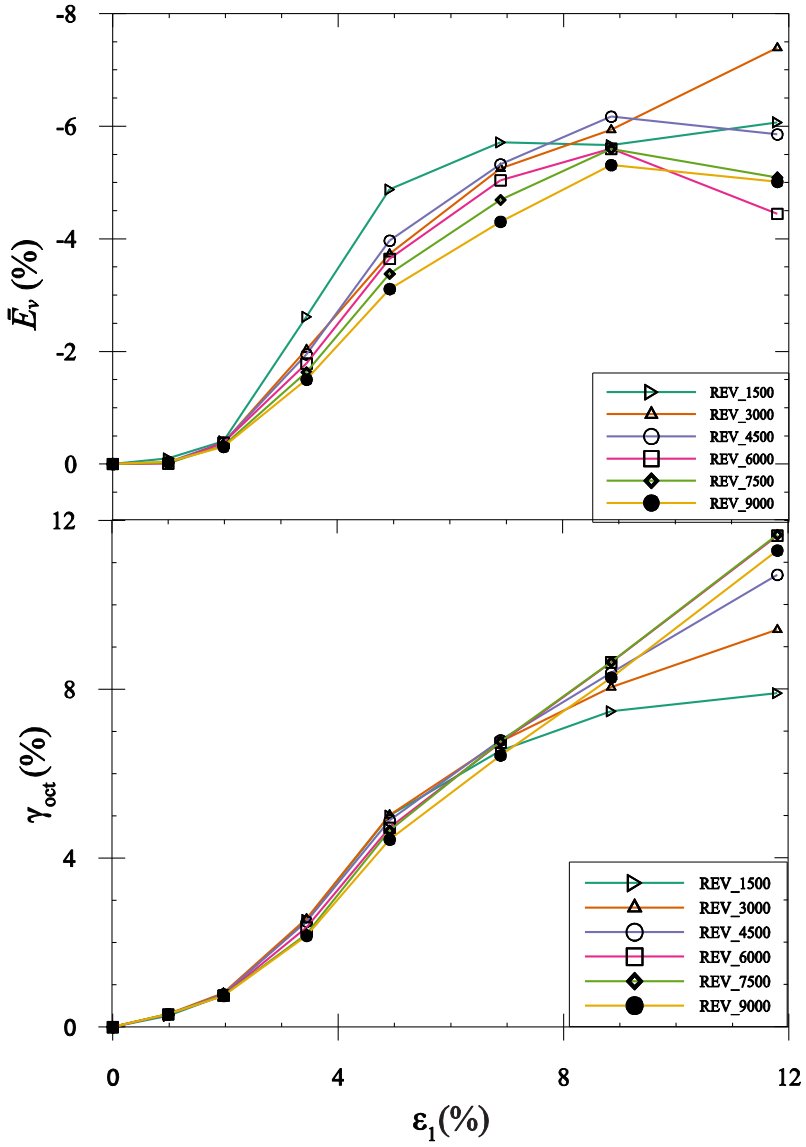

Figure 32. Eulerian volumetric and octahedral shear strains versus the global nominal axial strain for different REV sizes taken near the top of the F35-D-400kPa specimen.

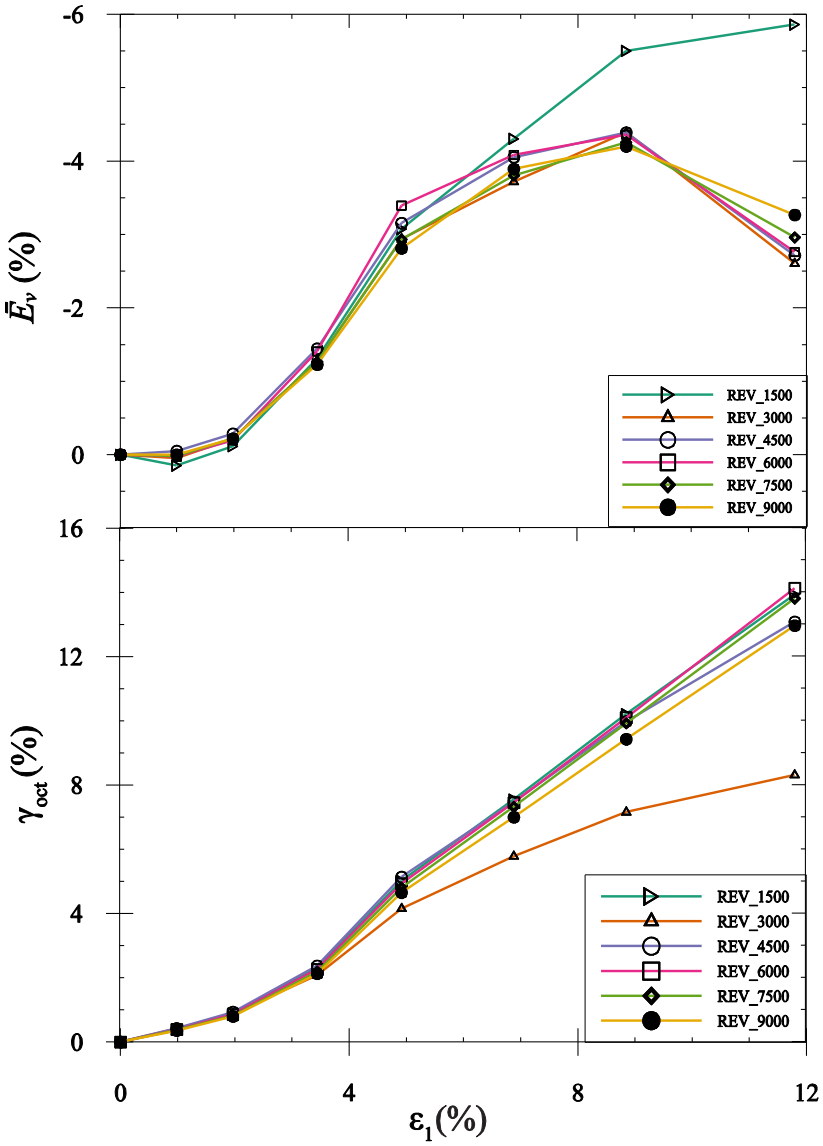

Figure 33. Eulerian volumetric and octahedral shear strains versus the global nominal axial strain for different REV sizes taken near the bottom of the F35-D-400kPa specimen.

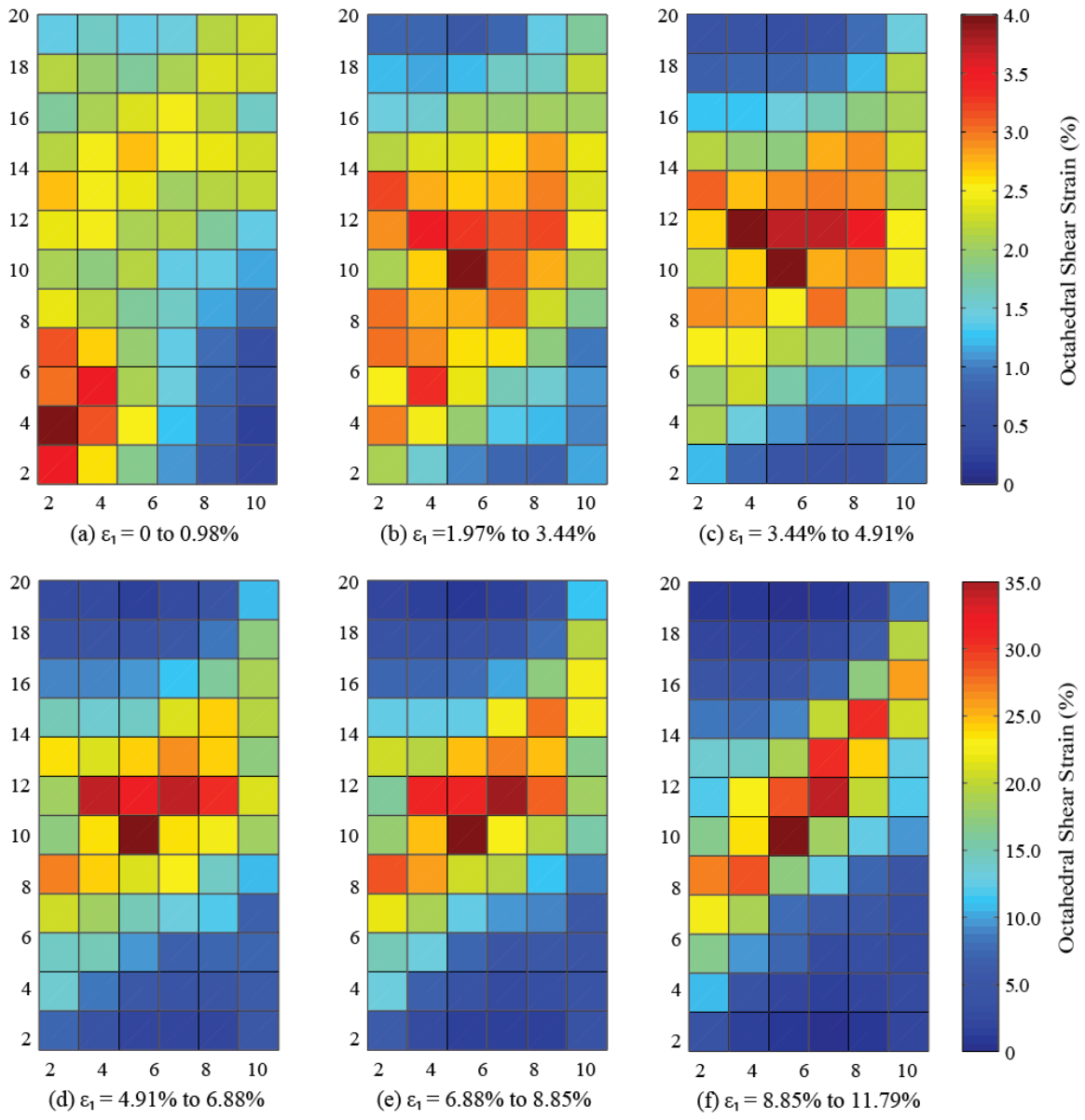

Figure 34. Color maps of the octahedral shear strains for 1500 micron REVs at a central axial section of the F35-D-400kPa specimen.

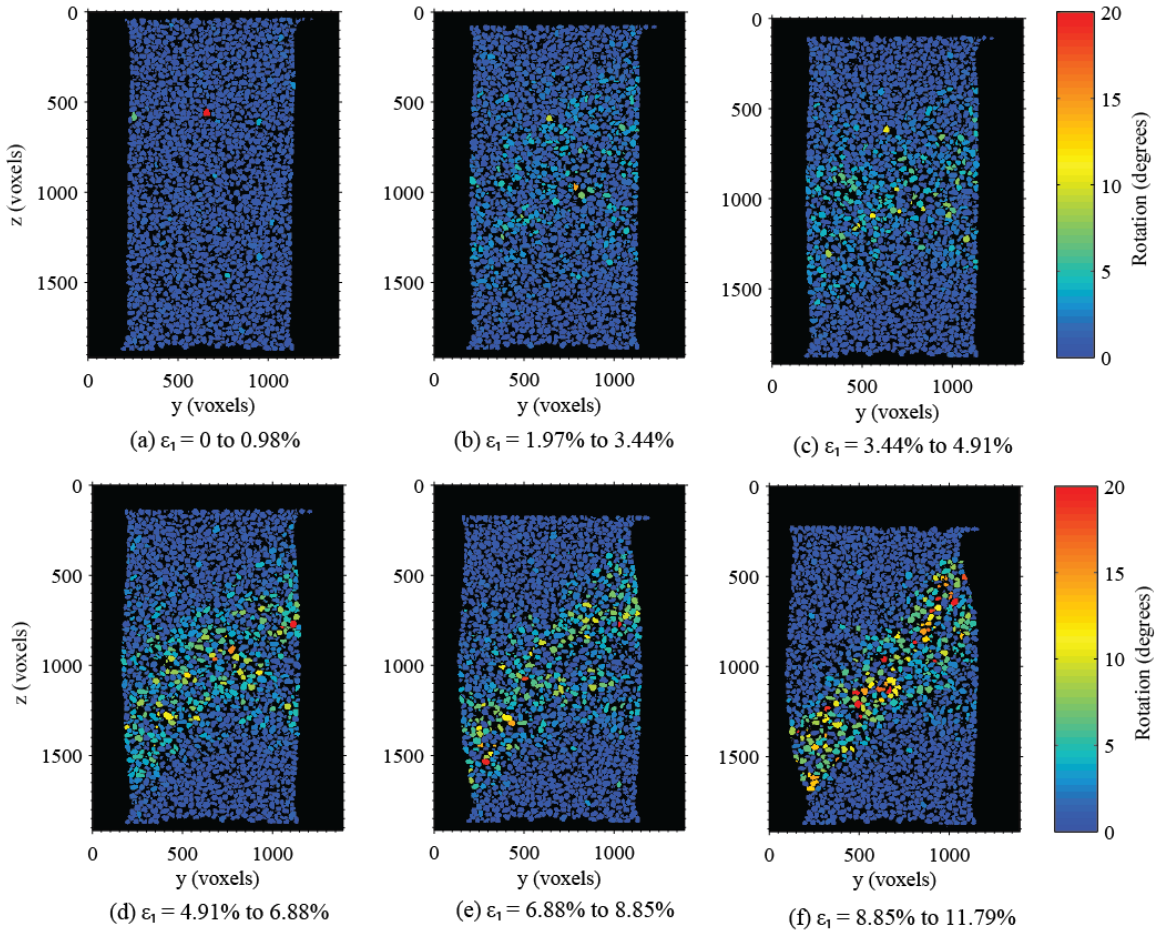

Figure 35. Rotation angle of particles for the F35-D-400kPa specimen.

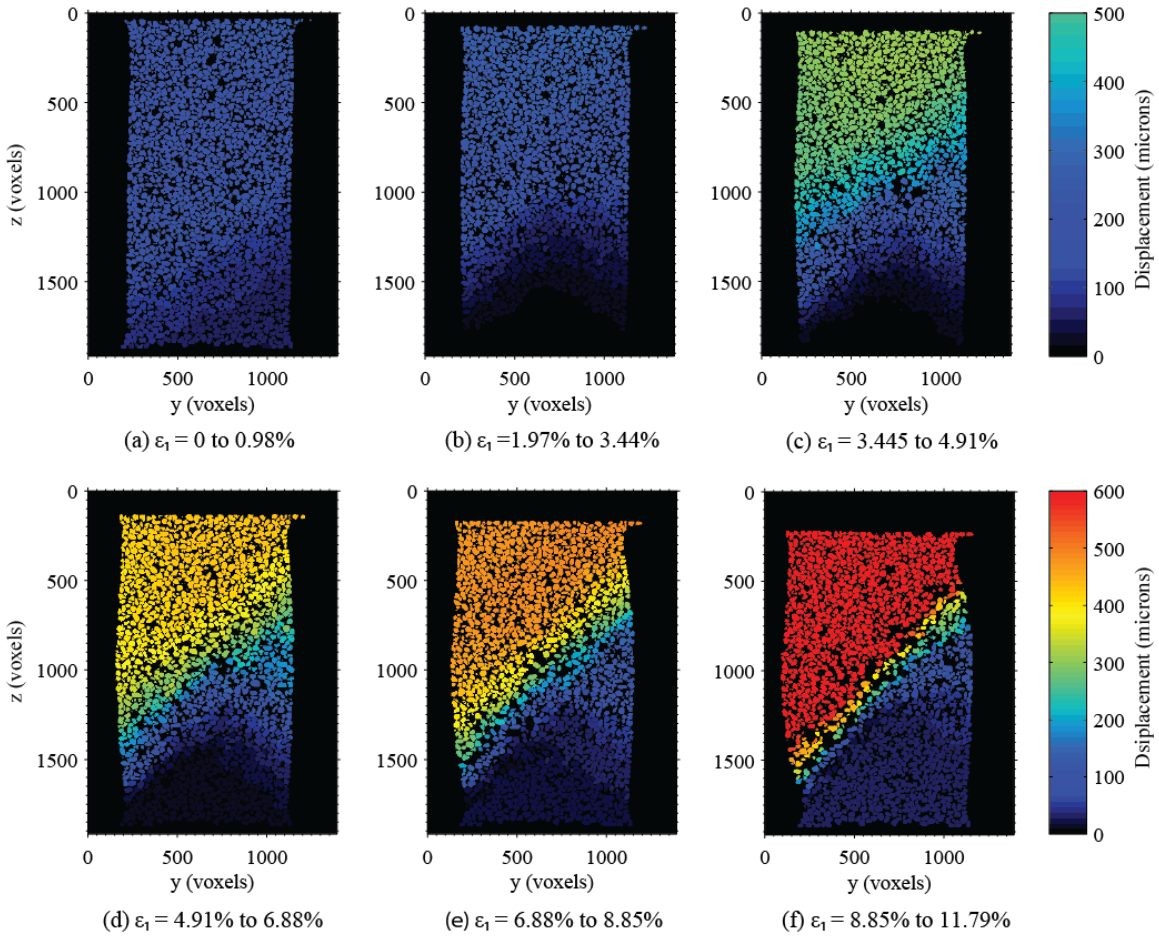

Figure 36. Particle translation for the F35-D-400kPa specimen.

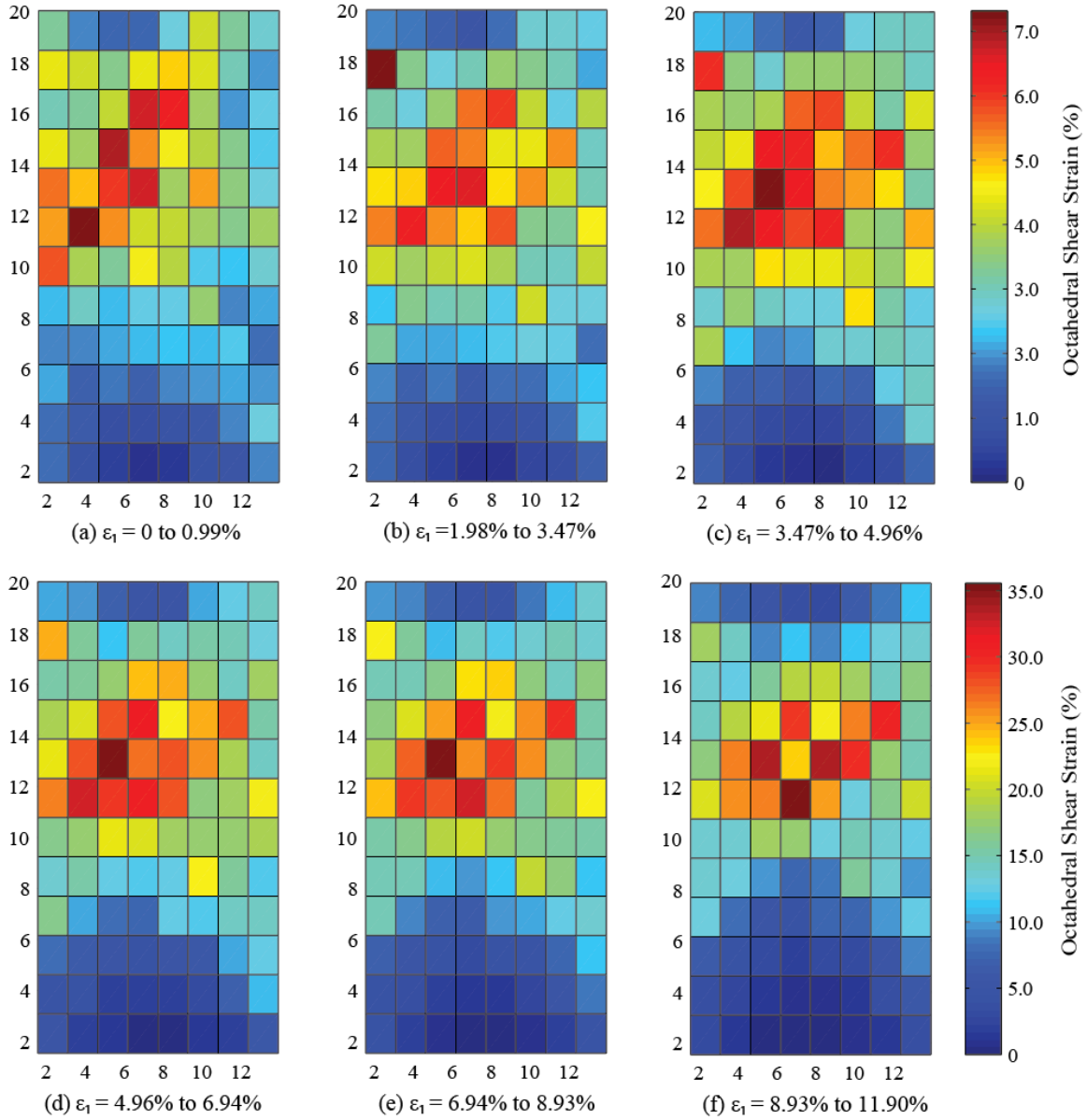

Figure 37. Color maps of the octahedral shear strains for 1500 micron REVs at a central axial section of the F35-D-15kPa specimen.

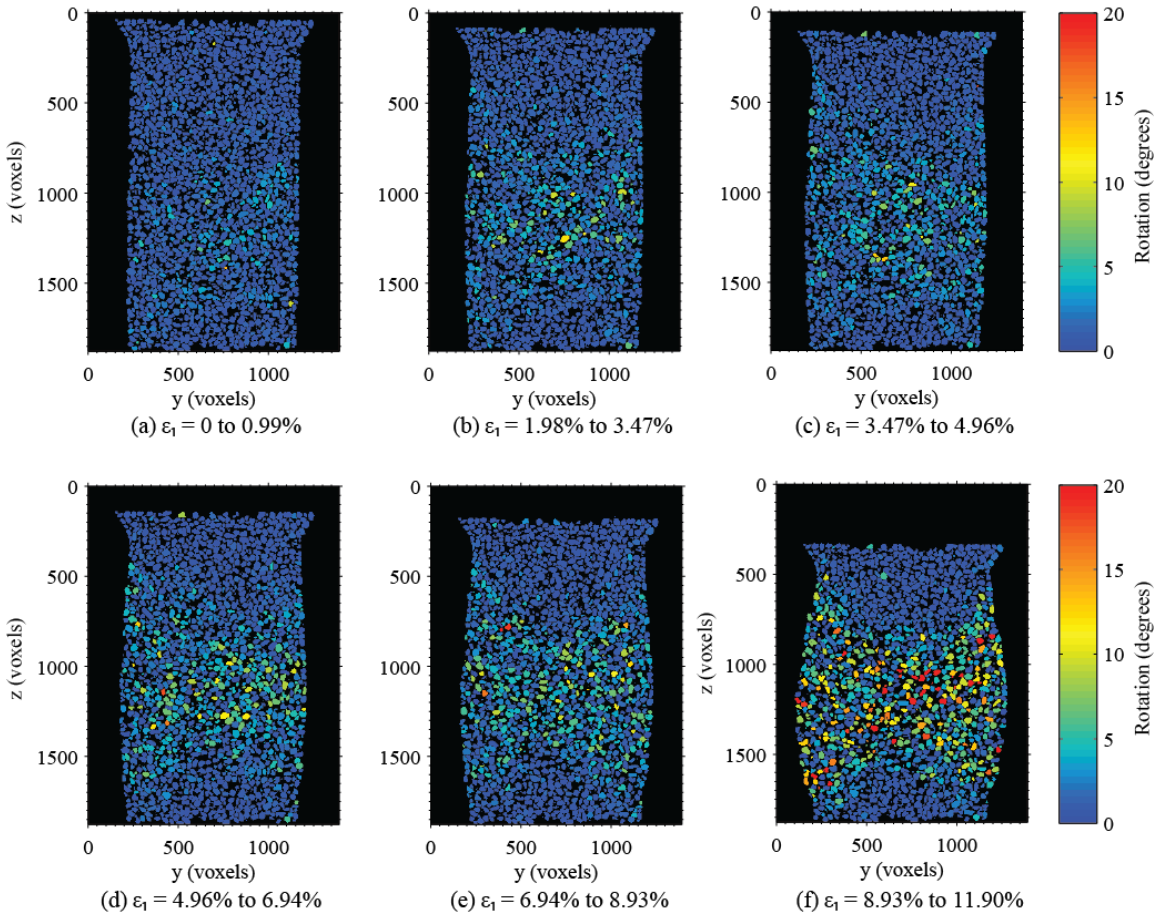

Figure 38. Rotation angle of particles for the F35-D-15kPa specimen

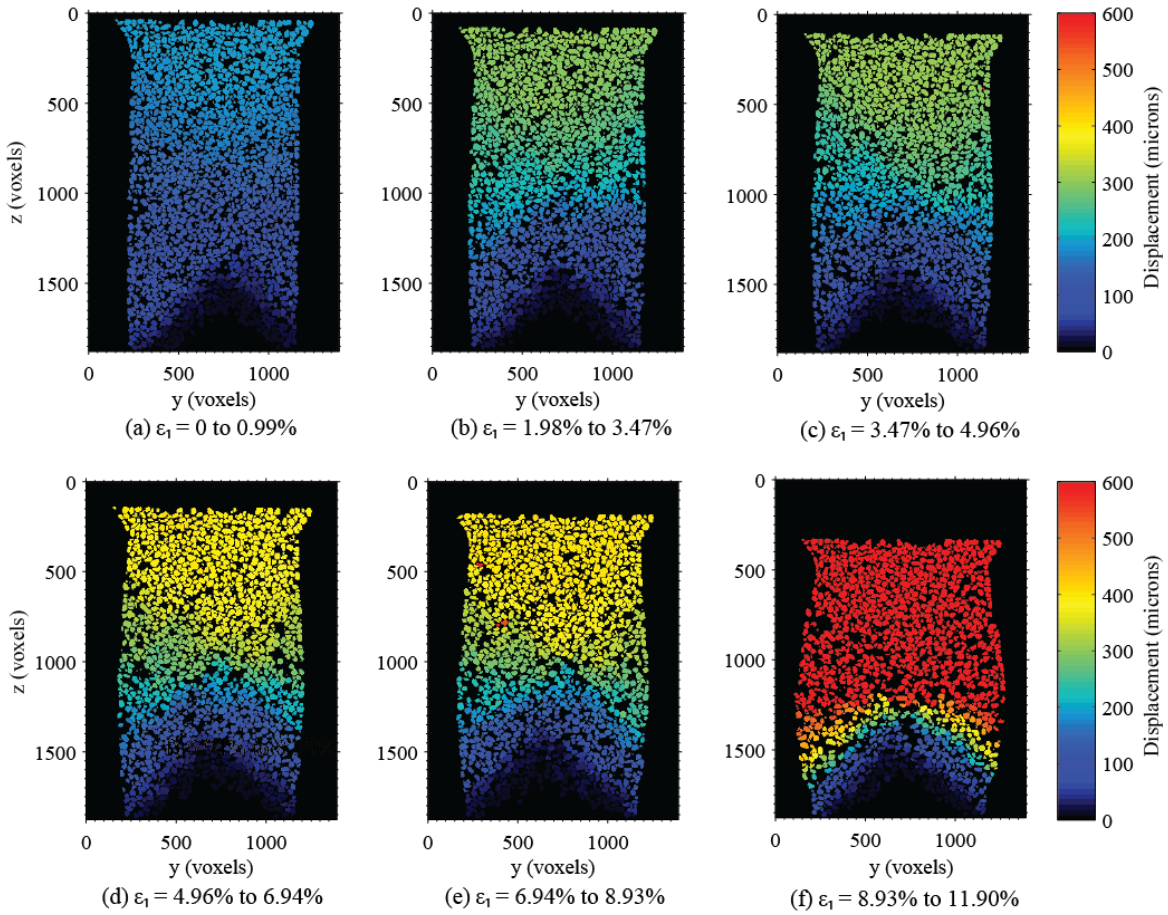

Figure 39. Particle translation for the F35-D-15kPa specimen.

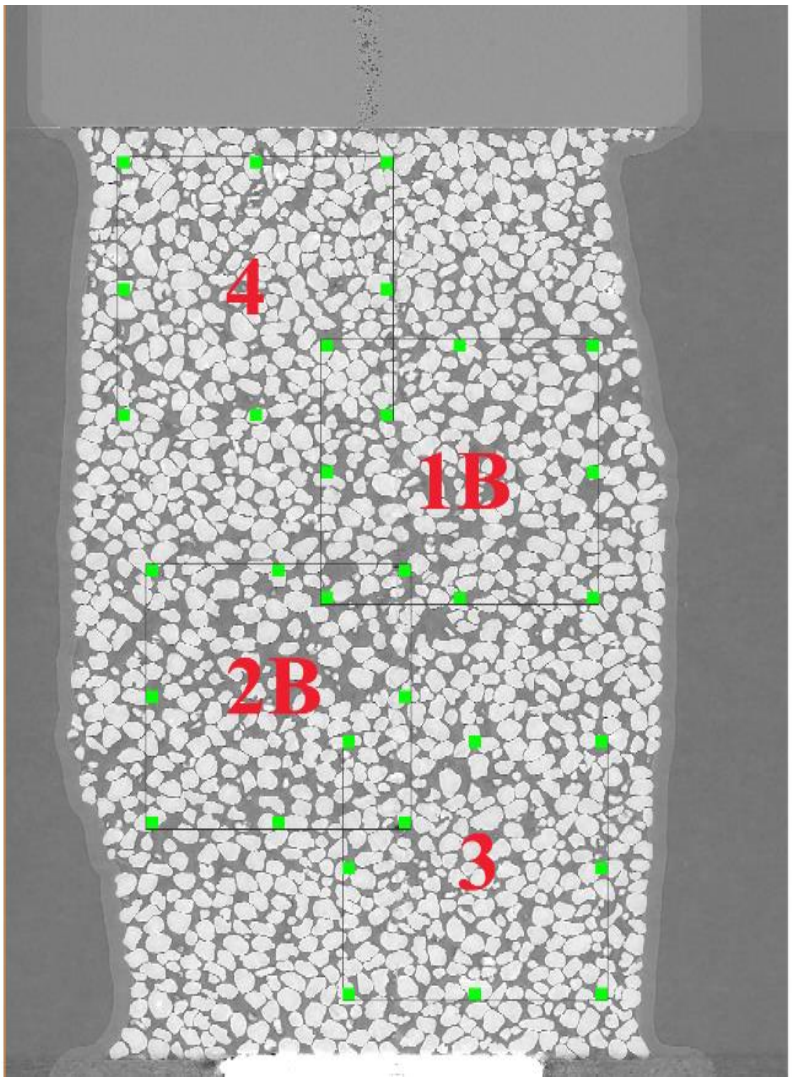

Figure 40. Locations of 5000 micron REVs at central axial section of F35-D-400kPa specimen.

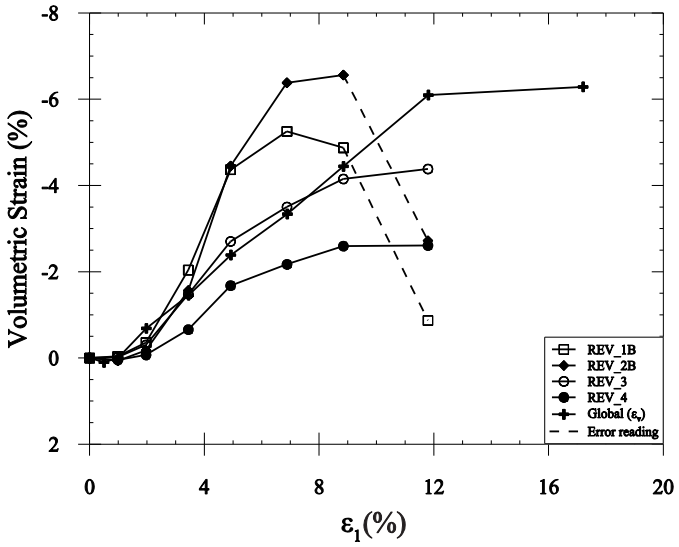

Figure 41. Volumetric strains ($\bar{E}_v$) versus global nominal axial strain (ε_1) for 5000 microns REVs along with the global volumetric strain (ε_v) versus ε_1 for F35-D-400kPa specimen.

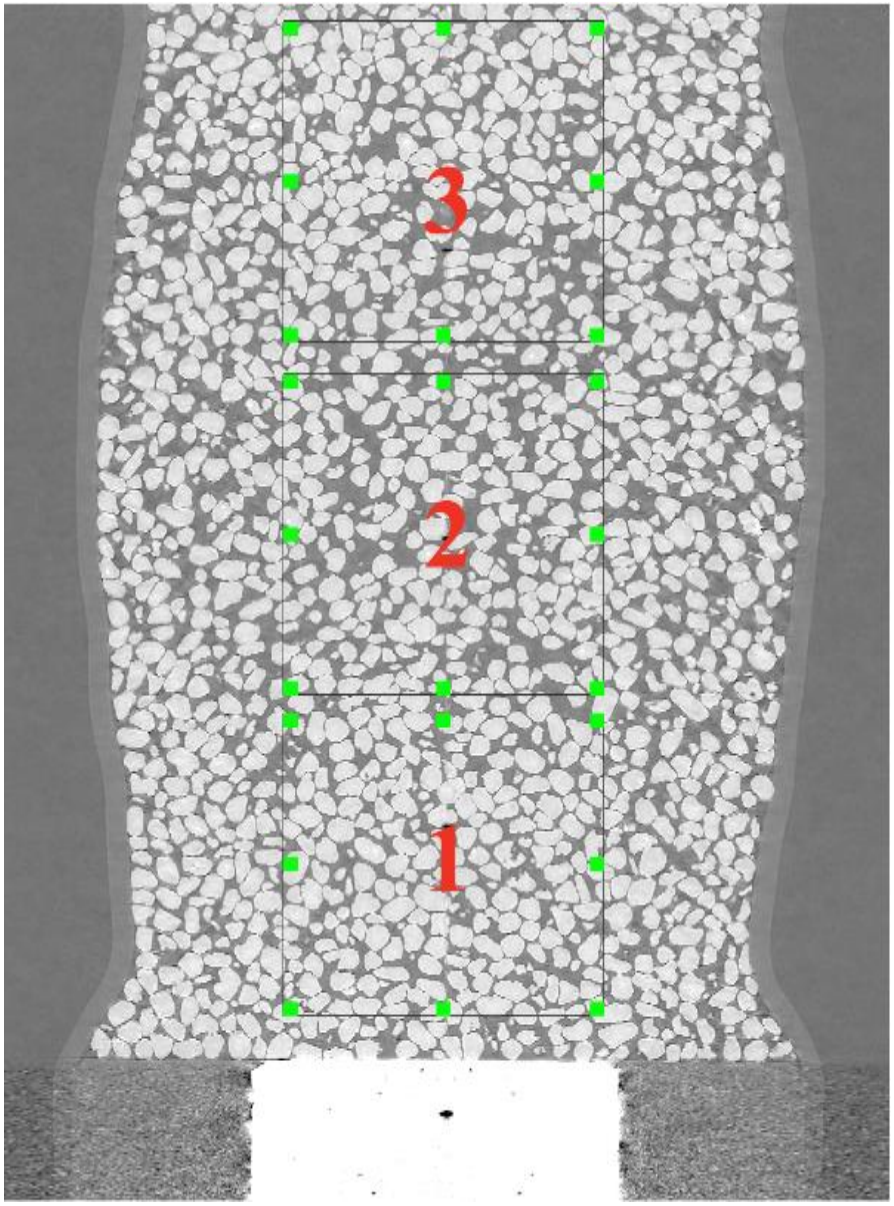

Figure 42. Locations of 5000 micron REVs at central axial section of the F35-D-15kPa specimen.

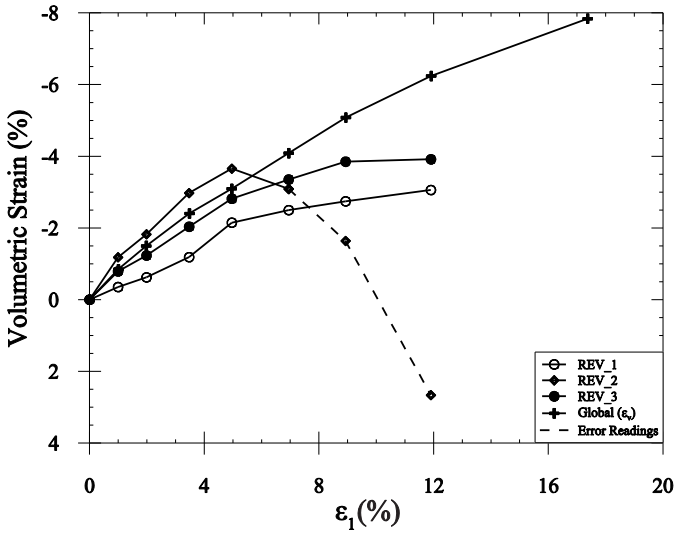

Figure 43. Volumetric strains ($\bar{E}_v$) versus global nominal axial strain (ε_1) for 5000 microns REVs along with the global volumetric strain (ε_v) versus ε_1 for F35-D-15kPa specimen.

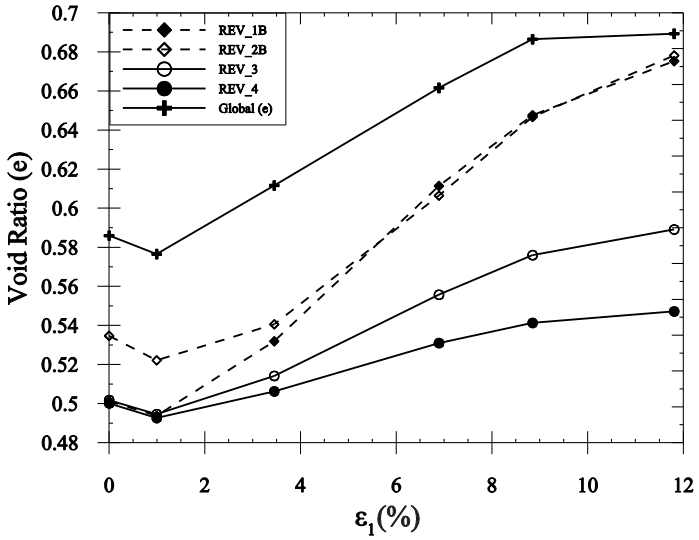

Figure 44. Evolution of void ratio for 5000 micron REVs for the F35-D-400kPa specimen along with global void ratio.

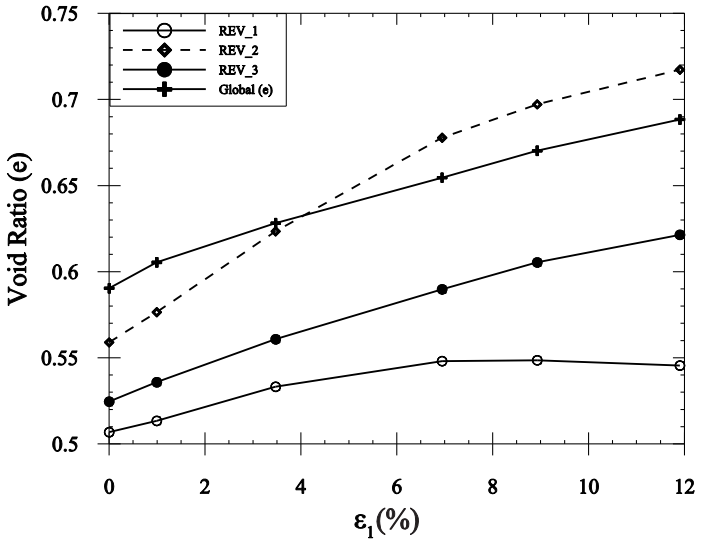

Figure 45. Evolution of void ratio for 5000 micron REVs for the F35-D-415kPa specimen along with global void ratio.

CONCLUSION

This work begins with presenting a 3D systematic experimental investigation of the effect of particle morphology, confining pressure, and specimen density on the failure modes of sand specimen tested under axisymmetric triaxial loading. The final findings of this research showed that specimen tested under low confining pressure, as well as loose specimen exhibited a preference to fail via bulging, which is an external manifestation of a complex internal shear pattern. Furthermore, particle roundness was found to be the major factor in the development of a single well-defined shear band or a bulging mode for dense specimens tested under high confining pressure.

The second part of this work, is a study that is leading in its field in successfully calculating the local finite strains in 3D on a sub-sample of the experimental data that was taken from the first part. It begins by applying different methods to find the appropriate REV size by testing different REV sizes. Local finite strain measurements were done using C++ codes based on the equivalent continuum mechanical approach. The major findings of this research showed that an REV size of 1500 microns (4.17 d50) was sufficient to give an average e. Color maps of the measured octahedral shear strains for REVs of the same size compared well with particle kinematics measurements that showed the locations of high shear strains. However, values of the measured $\bar{E}_v$ and $\bar{\gamma}_{oct}$ corresponding to this REV size were overestimated and in rare instances underestimated especially at the last two ε_1 increments. Therefore, a minimum REV size of 4500 (12.5 d50) micron is required to give better estimations of the $\bar{E}_v$ and $\bar{\gamma}_{oct}$. Then, the $\bar{E}_v$ was compared to the global volumetric measurements, which also can be considered as an averaging of all $\bar{E}_v$ .Finally, void ratio

evolution curves compared well with the volumetric strains at both the local and global level except in the last ε_1 increments for REVs located within zones of intensive shearing. This was due to acquiring SMT scans at strain increments that are higher than 2%.

Understanding and predicting the complex failure modes of granular material is very important in many Civil Engineering applications. One of which, is the mitigation process against soil mass failure. Soil mass failures, especially within highly populated areas, can be both dangerous and costly. An example of such occurrences are slope failures which can take place either naturally or due to excavation work in many construction projects. The "understanding" of the failure of a soil mass requires an experimental investigation of loaded specimen with different properties and boundary conditions, hence the first part of this thesis. After utilizing experiments to understand the behavior of sheared granular materials, models must be built in order to theoretically "predict" this behavior. Until now, there is no conclusive work on the formulation of constitutive laws that govern the behavior of granular material. Furthermore, there was no experimental validation of computer models that calculate strain tensors for such material. The second part of this thesis proved that this is possible, and will benefit modelers in implementing those findings into their constitutive models in predicting the behavior of soil.

VITA

Maha Fawaz Jarrar was born in Kuwait. In the shadow of the Gulf War her family moved to Jordan where she got her citizenship. When she was 10 years of age, her family decided to relocate and settled in the West Bank. There, she finished her undergraduate degree in Civil and Environmental Engineering at Birzeit University, Ramallah. Due to her academic excellence she was selected to work as a teacher assistant in the same program, where she worked for a year. In 2014, she moved to the U.S. to continue her graduate studies in Geotechnical Engineering at the University of Tennessee, Knoxville.